Studies of states in ^{19}Ne about the ^{18}F + p threshold and the ^{18}Ne(α,p) HCNO breakout reaction

Alexis Noel Josephides

School of Physics

The University of Edinburgh

Thesis submitted for the degree of
Doctor of Philosophy in the subject of *Physics*

2009

For

Family and Friends

Abstract

The rate of destruction of ^{18}F via the ^{18}F + p reactions is of importance in both novae and X-ray burster explosive scenarios. The rate of the competing destructive reactions, ^{18}F(p,γ)^{19}Ne and ^{18}F(p,α)^{15}O, depend upon the level structure of the compound nucleus ^{19}Ne.

The first experiment in this thesis examines the level structure of ^{19}Ne about the ^{18}F + p threshold via elastic ^{15}O(α,α)^{15}O scattering. The experiment was performed at the CRC Louvain-la-Neuve. A radioactive ^{15}O beam bombarded a thick ^{4}He gaseous target with elastically scattered alpha particles detected using segmented silicon detectors.

An R-matrix approach was used to analyse the data and extract the resonance parameters E_r and Γ_α. Particular emphasis was placed on extracting information regarding the possible $\frac{3}{2}^+$ doublet, the parameters of which, to date, have been inferred from the mirror nucleus ^{19}F. The nominal values for the doublet taken from the mirror are E_r = 8 and 38 keV, with Γ_α = 0.27 and 1.3 keV respectively. Following this new analysis it has been found that the doublet straddles the threshold at E_r = -22 and 3 keV, with Γ_α = 0.15 and 3.3 keV respectively. S-factor calculations and interference effects were also examined.

The ^{18}Ne(α,p)^{21}Na reactions is believed to be a key process in X-ray bursters. It is thought to be a possible HCNO-breakout reaction; the mechanism responsible for producing energy to drive the X-ray burster.

To date the reaction has been studied both directly and indirectly. The results from each previous experiment show sufficient discrepancies to warrant a re-examination of the reaction rate. As such, the

second experiment presented in this thesis revolves around a new direct measurement of ^{18}Ne(α,p). The experiment was undertaken at the CRC Louvain-la-Neuve, where, a radioactive ^{18}Ne beam impinged upon a thin gaseous ^{4}He target. The beam energy was chosen to provide data points in common with previous experiments at E_r = 1.7 and 2.5 MeV. Reaction protons were detected via a segmented silicon detector telescope system.

The total cross section calculated at E_r = 2.5 MeV is 1.22±0.151 mb. An upper limit for the cross-section of 0.0208 mb was evaluated at E_r = 1.7 MeV.

Acknowledgements

Despite what is written in the declaration I cannot take full credit for this body of work. It would not have been possible without the help and support of those around me.

I'd like to begin by thanking my supervisor Tom Davinson for his guidance over the three years. Thanks also to Marialuisa Alliota, Alex Murphy and Phil Woods for the useful discussions, support and sage words of wisdom.

My thanks to the scientific and technical staff at the CRC Louvain-la-Neuve, notably Guy and Marc for the expert beam tuning and Nic and Angel for their good humour and company on many a night shift.

I wish to especially thank Carmen Angulo and Pierre Descouvement for their help with both the experimental and theoretical work, their incredible patience and faith throughout.

A huge thank you to the Michael Bay obsessed Edinburgh nuclear physics group: The Rev. Dr. Cham 'God Loves You' Ghag, Gavin 'Don't Stop Believing' Lotay, Dan 'F*ck the Proton' Watts, Derek 'White wine spritzer' Glazier, Daria 'Howling Mad' Sokhan, Tom 'Charlie' Jude, Emma 'John Connor' Barnes, Mark 'Cultural Attache' Sikora, Steve 'Chillaxing' Plank, Pauline Scovell and Philip 'Salty Balls' Salter, without whom a tea break would have been 5 minutes not 45.

A colossal thank you to Claire Tarbert, without who, I can honestly say, hand on my heart, this magnum opus would not have been completed without. Her calming nature and stunning banter, not to mention her computer skills, were invaluable throughout.

Thank you to all the poor soles that put up living with me over the three years, Banksey, Ricky B, Jones, Josh, Captain O, Asher and Cammo.

Thank you to the Wally Dug and the Cambridge Arms (cheers Cookie) and of course Garibaldi's for allowing me to let off some steam.

I would also like to thank Milo, Smudger, Duncan and Leesa for their long distance support, it meant more than I think they realised. Finally I would like to thank my family for their support.

Acknowledgements to the Engineering and Physical Sciences Research Council (EPSRC) for funding of this project.

Declaration

The two experiments described in this thesis were performed by myself, fellow members of the Edinburgh University Nuclear Physics Group, and our collaborators at various international institutions. The data analysis and interpretation of results are entirely my own work, and this thesis has been written entirely by me. No portion of the work referred to in this thesis has been submitted in support of an application for another degree or qualification at this university or any other institute of learning.

A. Josephides

Contents

List of Figures

List of Tables

Chapter 1

Introduction and Astrophysical Background

1.1 Introduction

Nuclear astrophysics bridges the microscopic world of atoms and the evolution of the macroscopic universe. It is the field of physics responsible for the explanation of energy production in stars, and the cosmic synthesis of nuclei more complex than hydrogen. By reproducing the nuclear reactions present in stars within the laboratory, one can gain a wealth of insight into the stellar environment that is simply not possible by astronomical observation alone.

This thesis presents the results from two new experiments probing reactions of particular importance to nuclear astrophysics. The first is a study of states in ^{19}Ne about the ^{18}F + p threshold via elastic ^{15}O(α, α) scattering. Improved knowledge of the ^{19}Ne level structure is essential in order to better understand the rate of the competing destructive reactions ^{18}F(p, γ)^{19}Ne and ^{18}F(p, α)^{15}O. The rate of destruction of ^{18}F via the ^{18}F + p reactions in turn plays a vital role in both novae and X-ray burster scenarios.

The second reaction under investigation is the ^{18}Ne(α, p)^{21}Na reaction. It is thought to be a key process in X-ray bursters and a possible hot CNO breakout reaction.

Given the importance of the reactions under investigation to various aspects of stellar evolution, it is appropriate to begin this thesis with a brief review of stellar evolution, such that the results might be properly placed in context.

1.2 Quiescent Burning Stages of Stellar Evolution

Immediately following the Big Bang the entire universe was composed of a hot dense fireball of elementary particles. This fireball quickly cooled and between 3-20 mins after the initial explosion it had largely condensed into the simplest elements: hydrogen and helium. At that time as much as 75% of the universe's mass was in the form of ^{1}H with 25% ^{4}He and a trace of other elements [2]. These, the most simple elements, came together under the force of gravity and formed the first Giant Molecular Clouds (GMC).

A stellar life cycle begins with the gravitational collapse of a GMC. The gravitational collapse of the clouds creating the earliest of the stars (Population III[1]), was triggered by the collision of two GMCs. The collapse forming Population II and I stars may be triggered by the GMC passing through a dense region of a spiral galaxy, or, by the resultant shock waves of a supernova.

As these primary gas clouds of hydrogen and helium collapse the net temperature of the cloud increases. At a certain point the density becomes such, that the cloud becomes opaque to radiation, the method by which most of the heat is released, and thus a rapid temperature increase occurs. At temperatures T_6 $\sim$10[2], hydrogen burning commences in the form of the p-p chain (Section 1.2.1.1), and the collapse is halted by the thermal pressure exerted from the core, thus stabilising the star in a state of hydrostatic equilibrium of quiescent burning of nuclear fuel.

During quiescent stages of stellar evolution, the reactions that occur take place over large timescales (for $M < 2.0M_{\odot}$ t$\sim 10^{10}$ years) and, as a result, mainly involve stable or long-lived nuclei. For example, protons in the Sun (internal temperature is T_7 $\sim$1.5 and density of ρ $\sim$150 g/cm^3) have a typical energy of 1 keV. The cross-section for proton-proton fusion is σ $\sim 10^{-23}$ b[3]

[1] The category of Population a star falls into is dependent on its metallicity, i.e the total content of elements heavier that He. Population I are the youngest stars, for example the Sun. Population II are metal poor stars and the oldest stars yet observed in the universe. Population III stars, although not discovered, are included in theoretical models and contain no metals.

[2] This shorthand notation for temperature will be used throughout this thesis.T_x = y $\Rightarrow$ T = y$\times 10^x$ K.

[3] Cross-section (σ) in nuclear physics is analogous to the probability of a reaction occurring. Its unit is the barn, a unit of area, where, 1 barn = 10^{-24}cm^2.

therefore giving an average proton survival time of about 10^{10} years.

Stars remain static structures for a lifetime that is dependent on the rate at which they consume their available hydrogen fuel. A star in this period of its evolution is known as a Main Sequence star[1]

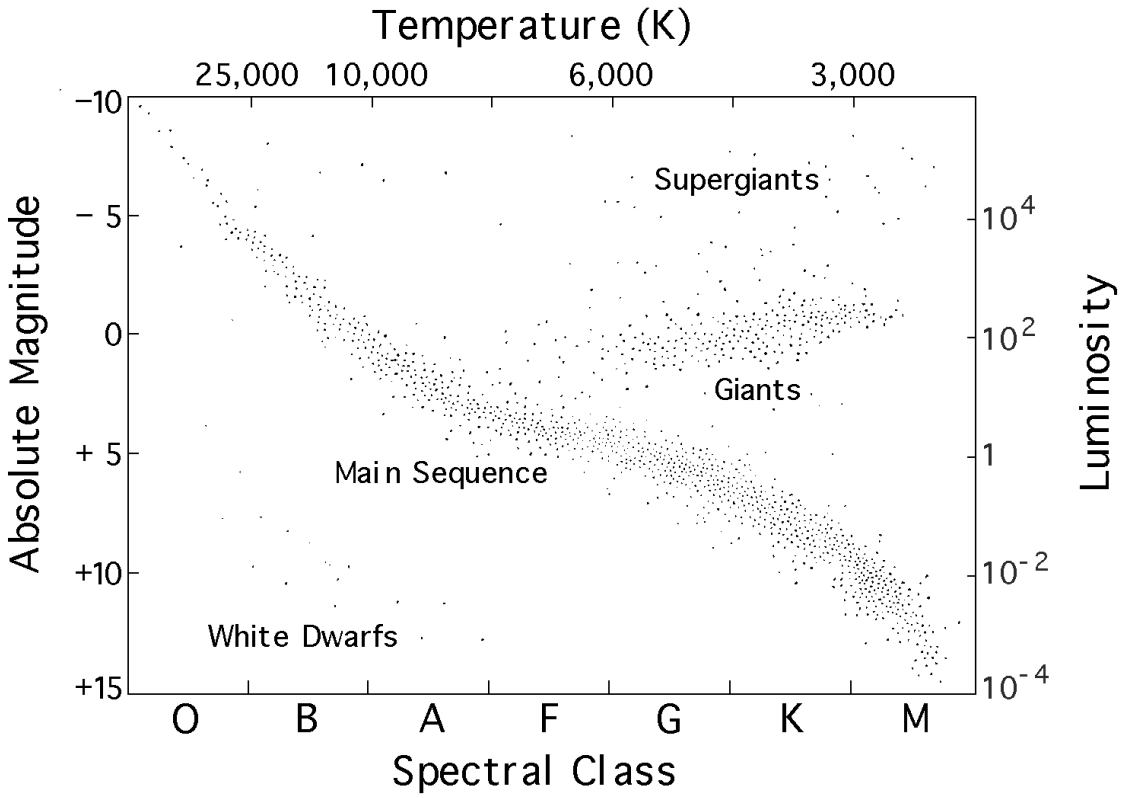

Figure 1.1: *The Hertzsprung-Russell Diagram [3]*

1.2.1 Hydrogen Burning Cycles

The hydrogen burning cycles are of great importance in main sequence stars as they are the main energy source. They also play a crucial role in the astrophysical scenarios studied later in this work and for that reason are outlined in the following sections.

[1]Refers to the area occupied in the Hertzsprung-Russell Figure 1.1, a plot of luminosity versus temperature. A main sequence star falls in the band running from the upper left-hand section to the lower right-hand part.

1.2.1.1 The pp-chain

The pp-chain comprises three sequences of reactions shown schematically in Figure 1.2. The net energy generated by each chain is identical since the overall process remains the fusion of four protons to form a ^{4}He nucleus.

The first two reactions in each chain are the same, generating ^{3}He. At this stage the chain splits and the progression of the sequence is determined by the relative abundance of ^{4}He. In helium-poor stars the first chain will dominate. However, if there is a significant abundance of ^{4}He, chains II and III will play an important role.

1.2.1.2 The Cold CNO Cycle

Like the pp-chain the Carbon-Nitrogen-Oxygen (CNO) cycles involve a number of processes in which the net result is hydrogen fusing to form helium nuclei. In this case however, carbon, nitrogen and oxygen are present and behave as catalysts. The cycles are one of the main energy generating processes in the quiescent burning stages of stars and are shown schematically in Figure 1.3. The necessary initial conditions for the cold CNO-cycle are a hydrogen-rich medium with sufficient abundances of carbon, nitrogen and oxygen as catalysts.

These cycles become the main source of energy generation within ($M > 1.5 M_\odot$) Population II and Population I stars once the temperature conditions are such that the proton capture reactions on the abundant carbon, nitrogen and oxygen occur at a greater rate than those of the pp-chain ($T_7 \sim 2$).

The complete CNO-cycle is made up of 4 sequences of reactions, each one feeding material to the next [4]. The first cycle was independently discovered in 1937-38 by Bethe and von Weizsäcker [5; 6; 7] and is commonly referred to as the CN-Cycle.

Cycle I (Q[1] = 26.73 MeV):

$$^{12}\mathrm{C(p,}\gamma)^{13}\mathrm{N}(\beta^+\nu)^{13}\mathrm{C(p,}\gamma)^{14}\mathrm{N(p,}\gamma)^{15}\mathrm{O}(\beta^+\nu)^{15}\mathrm{N(p,}\alpha)^{12}\mathrm{C}$$

The CN-cycle can branch at ^{15}N giving rise to the CNO bi-cycle. The ^{15}N(p,γ) reaction results in Cycle II, again with four hydrogen nuclei fusing to form helium.

Cycle II (Q = 12.126 MeV):

[1]Energy released/absorbed during a reaction. Arises from mass difference between parent and daughter nuclei.

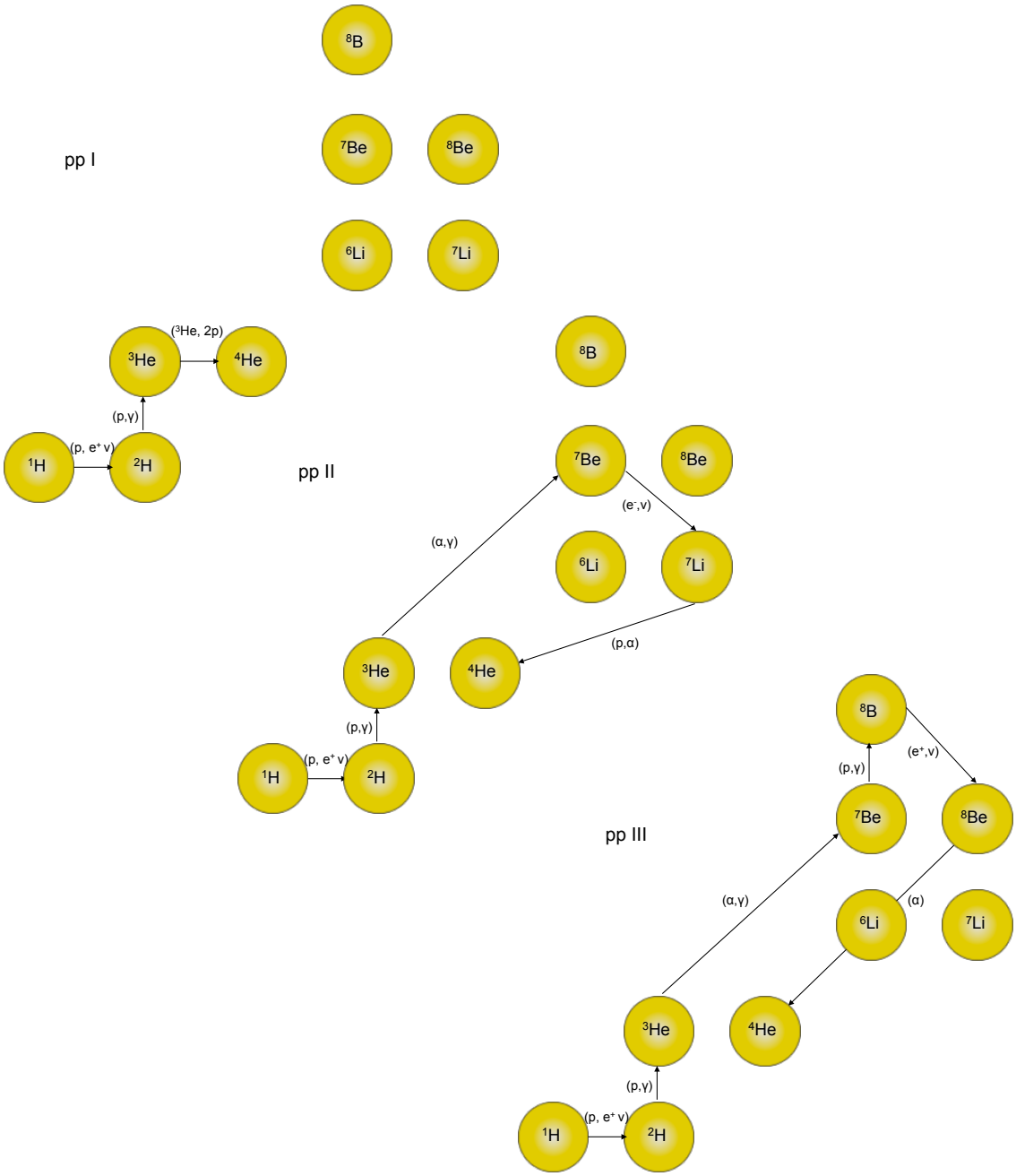

Figure 1.2: *The 3 pp-chains*

$$^{15}\mathrm{N(p,}\gamma)^{16}\mathrm{O(p,}\gamma)^{17}\mathrm{F}(\beta^{+}\nu)^{17}\mathrm{O(p,}\alpha)^{14}\mathrm{N}$$

Cycle I is the main contributor to energy generation as it proceeds 1000 times more often than Cycle II [8]. The remaining two cycles, their contribution to isotope production and their interplay with Cycles I and II are detailed in Figure 1.3.

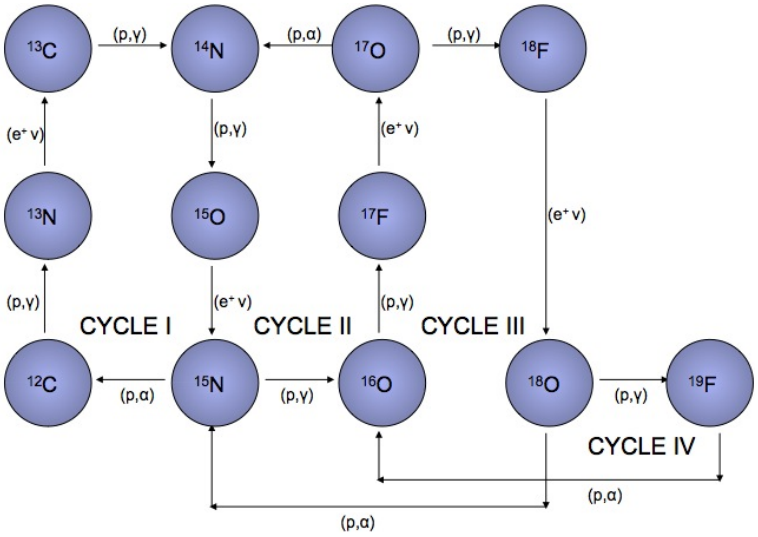

Figure 1.3: *The 4 CNO cycles*

1.2.2 Stellar Evolution

1.2.2.1 $M < 2.0M_{\odot}$

Once the hydrogen fuel has been exhausted in the core, i.e. once it has been completely converted to helium, the star is no longer in hydrostatic equilibrium and begins to collapse. The collapse of stellar matter causes the core's temperature to increase. When the temperature in the area surrounding the core reaches a value of T_6 ~10, hydrogen burning commences in this region. Not all of the energy from this shell radiates out from the star's surface; some heats the intermediate layers giving rise to expansion. At this stage the star is classified as a *red sub-giant*[1]. As the outer layers continue to expand, the core contracts

[1]Lies on towards the the upper right-hand section of the H-R diagram

further until the conditions, T_9 ~0.23, ρ ~7x10^2 gcm^{-3}, allow for helium burning to take place via the triple alpha reaction[1] At this point the expansion is halted and the star is now a *red giant*[2].

For stars of initial mass M <0.7 $M_\odot$ the necessary core temperature required for helium burning is never reached. Instead, following their initial expansion, they contract until the gravitational collapse is balanced by electron degeneracy[3] within the core. These stars are known as *white dwarfs*[4]. Stars with masses between $0.7M_\odot$ and $1.5M_\odot$ (once the helium has been exhausted) also become white dwarfs.

1.2.2.2 M >2.0$M_\odot$

Massive stars (M >2.0$M_\odot$) evolve in the same manner as smaller stars, with the exception that their initial mass is great enough to allow further burning stages of elements heavier than hydrogen and helium. Following the triple alpha stage, the core once again contracts and the temperatures and densities reached allow for carbon burning. Following this both oxygen and silicon are burned. It is believed that only stars with masses greater than $8M_\odot$ will achieve conditions necessary for the nucleosynthesis of elements up to iron. The timescales of these heavy element burning stages are considerably quicker than the hydrogen and helium quiescent burning stages.

With the synthesis of an iron core, the star no longer has a viable fuel source to continue energy production and therefore cannot counteract the effects of gravitational collapse. When the core's size exceeds that of the Chandrasekhar Limit[5] the inward gravitational force can no longer be balanced by the outward electron degeneracy pressure and the core collapses. As this happens, the iron decomposes to helium and neutrons (via photodissociation). Neutrons and neutrinos are further produced from protons and electrons coming together. The

[1] Sequential two step process. First step is the reaction ^{4}He+^{4}He$\rightleftarrows^8$Be. The unstable ^{8}Be reacts in the second step ^{8}Be(^{4}He,γ)^{12}C.

[2] Found centre right of the HR diagram 1.1

[3] Degenerate matter refers to matter whose density is so high that the factor governing its pressure are quantum effects arising from the Pauli principle. The matter has been compressed to a stage where all particles are in their lowest energy configurations and thus no further compression can take place

[4] Found bottom left-hand corner in the HR diagram 1.1

[5] Limit on the mass of bodies consisting of electron degenerate matter. Taken to be M ~1.44$M_\odot$

neutrinos escape from the core radiating energy and further accelerating the core collapse. With almost pure neutron matter remaining the core collapse is eventually halted by a neutron degeneracy pressure. The rebounding shock wave blows off the outer layers of the star. This is a Type II Supernova explosion.

The remnant of this forms a neutron star and it retains stability through the balance between gravity and the neutron degeneracy pressure. The neutron core can further collapse to become a Black Hole if its radius is less than or equal to the Schwarzschild radius[1].

1.3 Explosive Stellar Scenarios

Explosive stellar burning processes occur under extreme stellar temperature and density and involve reactions that take place on a timescale of the order of seconds. Due to the short timescales on which the nuclear interactions take place, short-lived, unstable nuclei play an active role in these scenarios thus opening new reaction sequences and cycles.

There are two types of explosive scenario; catastrophic which entirely disrupt the whole star on which the event takes place, e.g Supernovae, and cataclysmic, which only partially disrupts the stars surface, such as Novae and X-Ray Bursters. It is reactions that occur within cataclysmic explosive scenarios that will make up this body of work.

1.3.1 Novae

Novae are recurring (every 10^3-10^5yr [10]) explosive events that are believed to occur on the surface of white dwarfs. They are characterised by an intense increase in luminosity reaching a maximum of $\sim 10^{37}$-10^{38} ergs s^{-1}[2], typically a factor of $\sim 10^4$ greater than before the explosion. It is believed that in our galaxy alone there are $\sim 30 \pm 10$ yr^{-1} [11].

A typical optical light curve for a classical nova event is shown in figure 1.4. The fast rise time, over a couple of days, is followed by a much slower decay time. The decay time[3] varies greatly from, less than 10 days for a very fast nova

[1] Characteristic radius associated with every mass.$r_s = 2Gm/c^2$

[2] 1 erg = 1 g $cm^2 s^{-2}$, with 1 eV = 1.60×10^{-12} ergs

[3] The time taken for maximum luminosity to decrease by 2-3 orders of magnitude

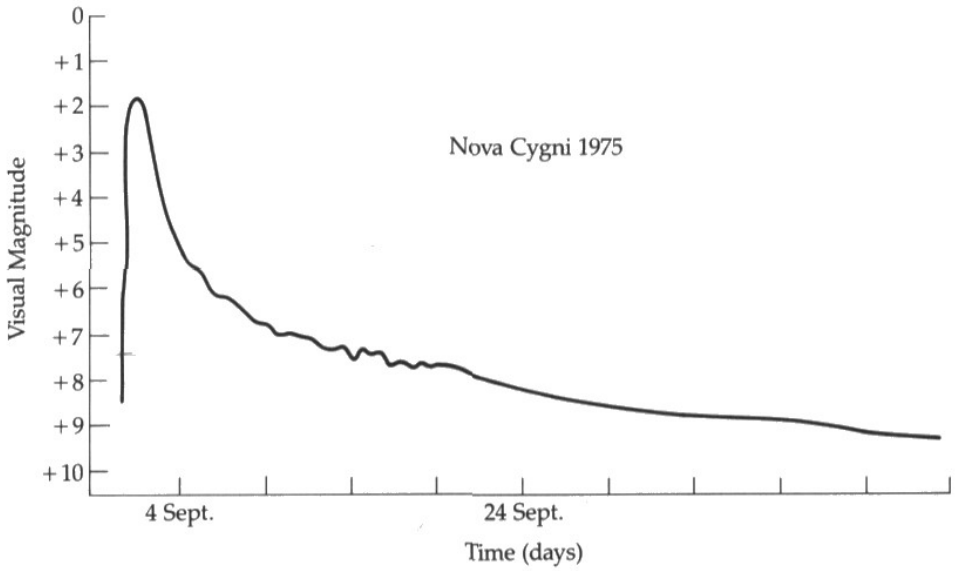

Figure 1.4: *The Nova Cygni light curve. First detected on the 29th August 1975 with a visual magnitude of 3.0. The peak magnitude of 2.0 was reached the next day, which then faded rapidly by 3 magnitudes in the next three days. Over a 45 day period the visual magnitude descended a total of 7 magnitudes [9].*

and between 150-250 days for a slow nova. As a general rule, the brighter the nova the faster the decay time.

Observations at different wavelengths also present certain characteristics specific to nova events. For instance, UV observations show that the total integrated flux of a nova event decreases at a much slower rate than that of purely optical observed flux.

Spectroscopic observations in the UV and IR range of the ejected material (M $\sim$10^{-5}-10$^{-4}M_{\odot}$) show over-abundances of some elements compared to typical solar system abundances. This spectroscopy points to the composition of the white dwarf. For example if a substantially higher abundance of neon is observed this indicates that the white dwarf was an *Oxygen-Neon* (O-Ne) dwarf.

The composition of the ejecta and their characteristic γ-ray lines, e.g. from ^{18}F, allow for important information about the star to be inferred, e.g. distance.

The peak temperatures reached in explosive scenarios are typically between T_9 $\sim$0.1-0.2 for C-O white dwarfs and T_9 $\sim$0.4-0.5 for O-Ne-Mg white dwarfs [10; 12; 13].

1.3.2 X-Ray Bursts

X-ray bursters are recurring explosive stellar events occurring on the surface of a neutron star. They are characterised by intense X-ray activity of 10^{39}-10^{40} ergs (10^{46}-10^{47} MeV).

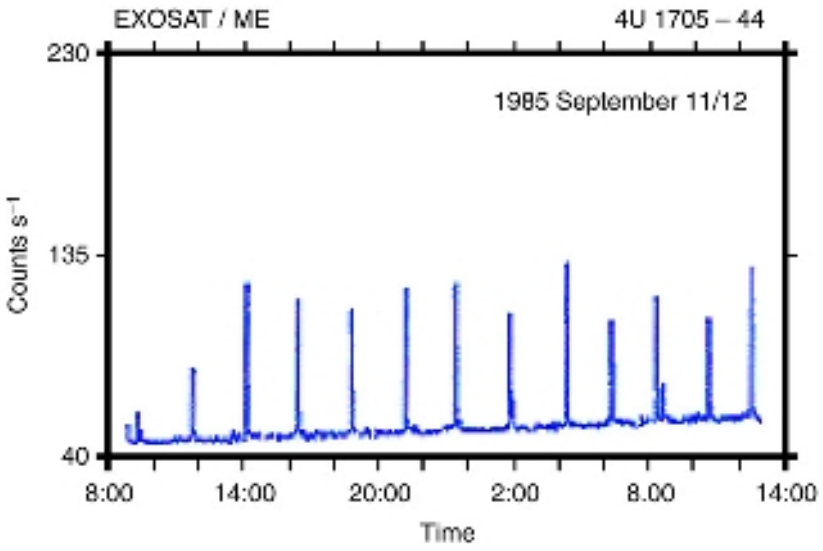

Figure 1.5: *X-ray burster light curve[14]. The figure illustrates a sequence of type I X-ray bursts plotted as a function of time for EXOSAT observations. The typical frequency varies between 0.2-0.5 bursts/h.*

There are two types of X-ray burster, Type I and Type II. Type I are the most common, with the signature of a sharp rise time of 1-10 s in luminosity (typically one order of magnitude increase), followed by a decay time 5-100 secs. The bursts typically last for a minute and repeat after several hours-days. Figure 1.5 shows a typical light curve for such an event.

Type II bursters are characterised by quick pulses recurring within minutes of each other.

1.4 Binary Systems

A binary system consists of two stars orbiting about their common point, the centre of mass (CoM). Associated with every star is its Roche lobe, a hypothetical area around a star marking its gravitational boundary. Within a binary system, the Roche lobe of each star may overlap, thus forming a figure of

eight-like equipotential surface around the inner Lagrangian point (where the gravitational effects of each star cancel) (Figure 1.6) [15].

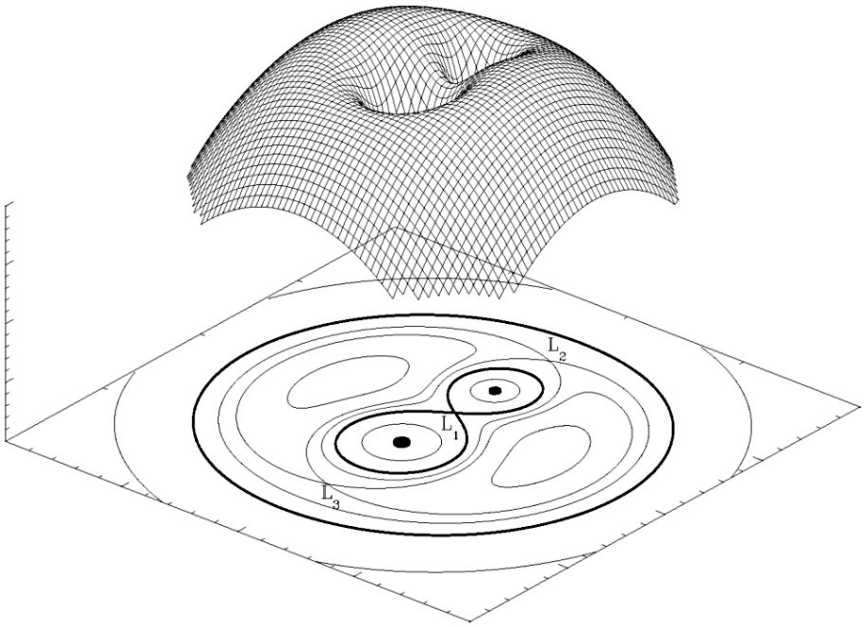

Figure 1.6: *A three-dimensional representation of the Roche potential in a binary system with stellar mass ratios of 2 to 1, in the co-rotating frame. The droplet-shaped figures in the equipotential plot at the bottom of the figure are called the Roche lobes of each star. L1, L2 and L3 are the Lagrangian points where forces cancel out. Mass can flow through the saddle point L1 from one star to its companion, if the star fills its Roche lobe[15]*

During the lifetime of the binary system, the stars will evolve independently over different timescales, depending on their initial mass. If, during this evolution, one of the stars were to undergo an expansion, e.g. migrate from main sequence to the red giant phase, and fill its Roche lobe, matter will fall from it onto its companion.

1.4.1 Novae

In the case of novae, the binary system will consist of a white dwarf and another less evolved star, typically a main sequence star that has begun to develop into a red giant. The white dwarf will either be primarily composed of carbon and oxygen (C-O white dwarf mass $\sim 1\ M_{\odot}$) or, if more evolved, oxygen, neon and

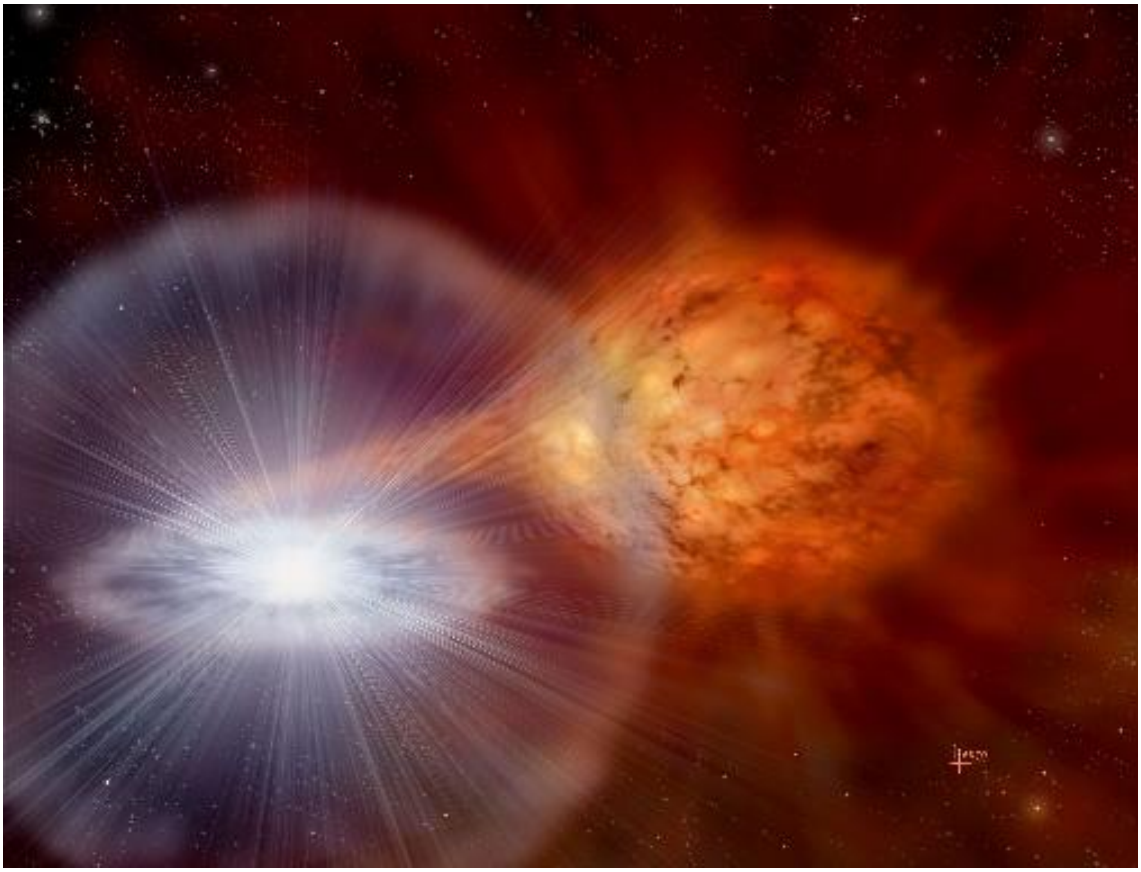

Figure 1.7: *An artist's impression of a typical explosive event occurring in a binary system[16]. The picture shows material falling from the red giant and spiralling around the white dwarf/neutron star forming and accretion disk, which, in turn falls onto the surface of the white dwarf/neutron star.*

magnesium (O-Ne-Mg mass$\sim$ 1.2-1.4 $M_{\odot}$) [10]. Hydrogen-rich matter from the expanding main sequence star falls onto its white dwarf companion. This material forms an accretion disk[1] around the white dwarf, which subsequently falls onto the degenerate surface. This material is enriched with 'dredged-up' matter, ^{4}He, ^{12}C, ^{16}O if a C-O white dwarf, or, ^{16}O, ^{20}Ne, ^{24}Mg if O-Ne-Mg white dwarf. The typical mass transfer rates ($\sim 10^{-9} M_{\odot}$/yr) from the main sequence/red giant allow this envelope to cool and become degenerate until a critical density is reached, $\rho \sim 10^{3}$g/cm^{3}[10].

At this point, the matter in the envelope will 'ignite' and, due to its degenerate nature, the temperature will increase without the envelope expanding and cooling. The initial burning stage within the envelope is thought to be the pp-chain.

The rapid increase in temperature at constant pressure and density, coupled with the 'dredged-up' catalysts of ^{12}C, ^{16}O open up further reaction channels, namely the cold CNO cycles which, eventually, under the correct conditions, will become the hot-CNO cycle. It is the hot-CNO cycle that will occur on a short timescale and generate the energy needed to power the subsequent explosion.

The temperature at the surface continues to rise until the Fermi temperature[2], [17], is reached. At this point, the degeneracy is lifted, resulting in a rapid expansion with matter being ejected into space, see Figure 1.7 [16].

1.4.2 X-Ray Bursts

These stellar phenomena also occur within cataclysmic binary systems in which a star fills its Roche lobe and matter is accreted onto its companion. There are, however, marked differences between X-ray bursters and Novae. Firstly, the star onto which matter accretes is not a white dwarf but a neutron star, secondly, the time frame on which these events re-occur is much shorter (hours-days) and, thirdly, no matter is expelled during an explosion and thus it has no effect on interstellar abundances [18].

Hydrogen-rich material falls from the near main sequence companion in a similar manner to that of novae, typically with an accretion rate of 4.4×10^{-10}

[1] An accretion disk is the name given to the rotating disk of matter that may form around a star. The matter, as well as rotating, will spiral into the central body.

[2] The temperature associated with the Fermi energy, the energy of the highest filled quantum state of a fermion at 0 K.

$M_{\odot}$/yr [18]. An accretion disk around the neutron star is formed before the matter falls further onto the degenerate surface of the neutron star. Due to the greater gravitational potential of a neutron star in comparison to that of a white dwarf, the critical density at which thermonuclear ignition occurs is higher, 10^6-10^8 g/cm^3 [10].

Under these conditions, hydrogen burning takes place via the CNO-cycles, the catalytic matter arising from the ashes of previous X-ray bursts and as a result of the triple alpha burning process. The marked difference is that, due to the greatly increased density the temperatures reached within these stellar environments are higher than those in novae. These more extreme conditions allow for further reactions to become possible, involving heavier and more unstable nuclei. The conditions are such that a break-out from the hot CNO-cycle becomes possible. This break-out process of (α,p) burning is highly energetic and is the mechanism believed to power these explosive scenarios [17; 19], it also produces seed nuclei which will eventually lead to the *rp*-process. Once this thermonuclear runaway takes place and the Fermi temperature is reached, the degeneracy is suddenly lifted and the explosive X-ray burst takes place.

No matter is believed to be expelled during an X-ray burster, as the matter does not reach the necessary escape velocity. The gravitational binding energy of ∼200 MeV far exceeds the nuclear energy release of 6 MeV per nucleon [18]. The peak temperatures reached in such scenarios are typically $T_9 \sim 2$.

1.5 Explosive Hydrogen Burning

1.5.1 Hot CNO-Cycle

At the temperatures and densities (T ∼10^8-10^9 K, ρ ∼10^4 g/cm^3) associated with novae and X-ray bursters further hydrogen burning reaction channels are opened. The rate at which the four hydrogen nuclei are fused to form a helium nucleus in the hydrostatic cold CNO-cycle, is limited by the temperature independent beta decays within the chain known as *waiting point* isotopes. The cold CNO-cycle becomes the explosive hot CNO-cycle (HCNO) once the reaction rate of ^{13}N(p,γ)^{14}O exceeds that of ^{13}N(β^+ ν)^{13}C.

Thus the first stage of the hot CNO-cycle is:

$$^{12}\mathrm{C}(\mathrm{p},\gamma)^{13}\mathrm{N}(\mathrm{p},\gamma)^{14}\mathrm{O}(\beta^+\ \nu)^{14}\mathrm{N}(\mathrm{p},\gamma)^{15}\mathrm{O}(\beta^+\ \nu)^{15}\mathrm{N}(\mathrm{p},\alpha)^{12}\mathrm{C}$$

and dominates the reaction flow until $T_9 \sim 0.2$ [10].

Cycle II occurs at temperatures approaching $T_9 \sim 0.4$ and involves the bypass of the waiting point isotopes in the second cold CNO-cycle, namely, ^{14}O ($t_{1/2}$ = 70.59 s) and ^{15}O ($t_{1/2}$ = 122 s). The energy rate per cycle is thus β-limited and remains constant at ∼133 keV/s [14]. Once the reaction rate of ^{17}F(p,γ)^{18}Ne exceeds that of ^{17}F(β^+ ν)^{17}O, Cycle II occurs alongside the initial hot CNO-cycle transferring material to and from it:

$$^{15}\mathrm{N(p,\gamma)^{16}O(p,\gamma)^{17}F(p,\gamma)^{18}Ne}(\beta^+\ \nu)^{18}\mathrm{F(p,\alpha)^{15}O}$$

The full hot CNO cycles illustrating the interplay between the two cycles is indicated in Figure 1.8.

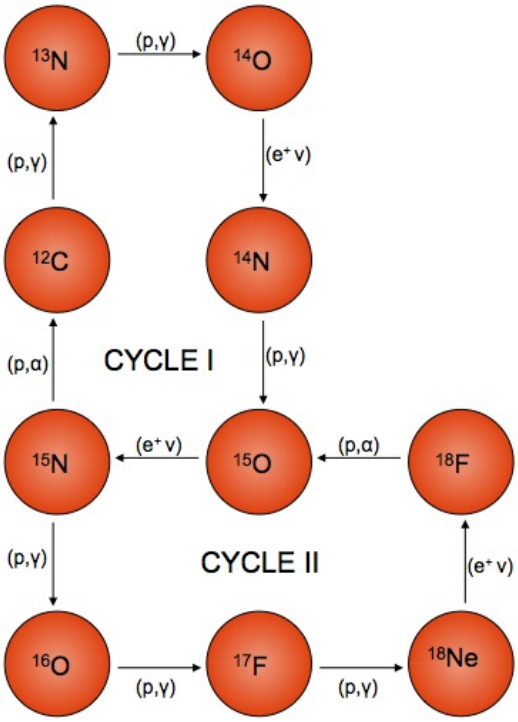

Figure 1.8: *The 2 hot-CNO cycles*

1.5.2 HCNO Break-Out

At temperatures exceeding $T_9 = 0.5$ such as those found in the environment associated with X-ray bursters it is possible to bypass the waiting point isotopes

of ^{15}O($t_{1/2}$ = 122 s) and ^{18}Ne ($t_{1/2}$ = 1.67 s)[20] . The α capture reactions on these two nuclei are known as the hot CNO break-out reactions[1]. They are:

$$^{15}\mathrm{O}(\alpha,\gamma)^{19}\mathrm{Ne}$$
$$^{18}\mathrm{Ne}(\alpha,\mathrm{p})^{21}\mathrm{Na}$$

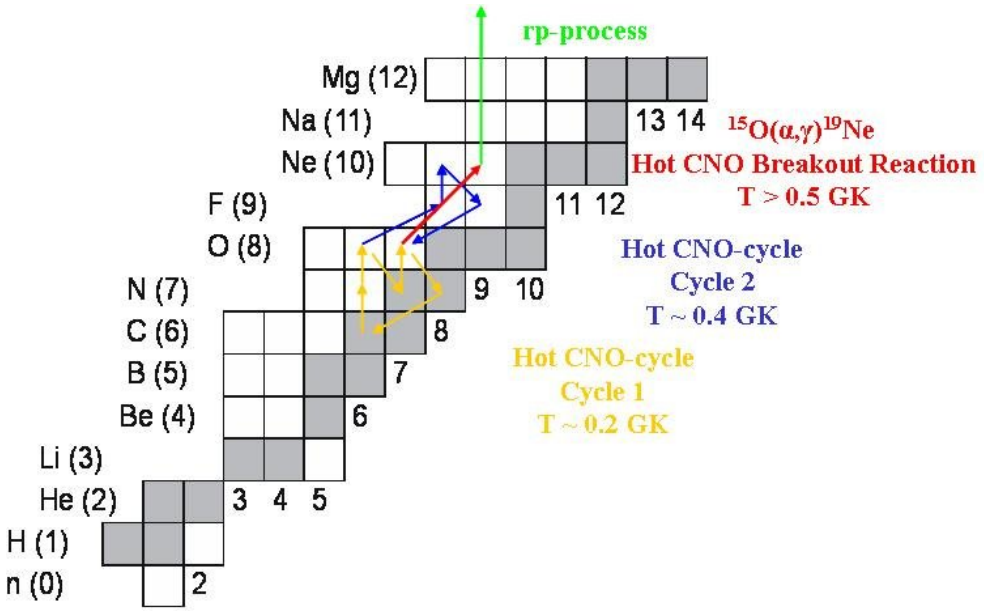

Figure 1.9: *HCNO break-out reaction path for the $^{15}O(\alpha,\gamma)^{19}Ne$ reaction, shown in red.*

These two reactions are believed to be the trigger for the rp-process[2] providing the initial seeds, as well as the energy required to drive the explosion associated with an X-ray burster.

1.6 Astrophysical Importance of ^{18}F and the ^{18}Ne(α,p) Reaction

1.6.1 ^{18}F

^{18}F is a positron emitter with a half-life $t_{1/2}$ = 110 mins. A general property of positron emitters is the β^+ annihilation with environmental β^- to produce two

[1]There is a third α capture reaction on ^{14}O($t_{1/2}$ = 70.59 s), ^{14}O(α,p)^{17}F, but this is not involved in the break-out and merely transfers material between the hot CNO-cycles.

[2]A series of rapid proton captures and β-decays resulting in the nucleosynthesis of heavier elements.

back-to-back gamma rays each of 511 keV. ^{18}F is believed to be the main source of 511 keV radiation observed after novae events.

Two types of novae can be distinguished through observation, *Standard* novae (CO) and *Oxygen-Neon* novae (O-Ne) [21]. The former is identified via the γ decay of ^{7}Be (478 keV, observable for 2 months following the nova), and the latter from the resultant γ decay of ^{22}Na (1275 keV, observable for several years). The 511 keV emission characteristic of ^{18}F[1] is believed to occur in both types of novae.

The 511 keV line has yet to be observed and can only be observed through very early detection, generally before the visual maximum of the event. It is predicted to be the most intense emission from a nova and thus allows for detection at greater distances $\sim$10 kpc [21]. The initial 511 keV peak from the decay of ^{13}N ($t_{1/2}$ = 9.96 mins) is of shorter duration than the more ideally suited (for observation) peak associated with ^{18}F. Its longer half-life is on a similar timescale to the point at which the expanding ejecta resulting from the nova becomes transparent to γ-radiation. The gamma flux at 511 keV is directly proportional to the amount of synthesised ^{18}F and therefore the rates at which it is produced and destroyed are very important. ^{18}F is produced via the Hot-CNO cycle:

$$^{16}\mathrm{O(p,}\gamma)^{17}\mathrm{F(p,}\gamma)^{18}\mathrm{Ne}(\beta^{+}\nu)^{18}\mathrm{F}$$

Due to the high ^{16}O abundance on the surface of a white dwarf,^{18}F may also be synthesised via the sequence:

$$^{16}\mathrm{O(p,}\gamma)^{17}\mathrm{F}(\beta^{+}\nu)^{17}\mathrm{O(p,}\gamma)^{18}\mathrm{F}$$

It is destroyed either via:

$$^{18}\mathrm{F(p,}\gamma)^{19}\mathrm{Ne}$$

or via

$$^{18}\mathrm{F(p,}\alpha)^{15}\mathrm{O}$$

[1] ^{13}N ($t_{1/2}$ = 10 mins), a β^{+} emitter, is also ejected in novae.

The latter is the dominant reaction having the higher cross-section of the two due to the low value of the coupling constant of the electromagnetic decay (p,γ) compared to the (p,α) decay mediated by the strong force.

The calculation of the rates of the two destructive reactions of ^{18}F require a detailed spectroscopic knowledge of the states of ^{19}Ne about the ^{18}F + p threshold.

The competing ^{18}F + p reactions, as well as being important in the manner described above, also play an important part within the hot CNO cycle and its possible break-out. The competing rates of ^{18}F(p,γ)^{19}Ne *vs* ^{18}F(p,α)^{15}O determine whether there is a significant flow towards heavy element production through the break out reaction or whether there is a return to the HCNO cycle 1.10.

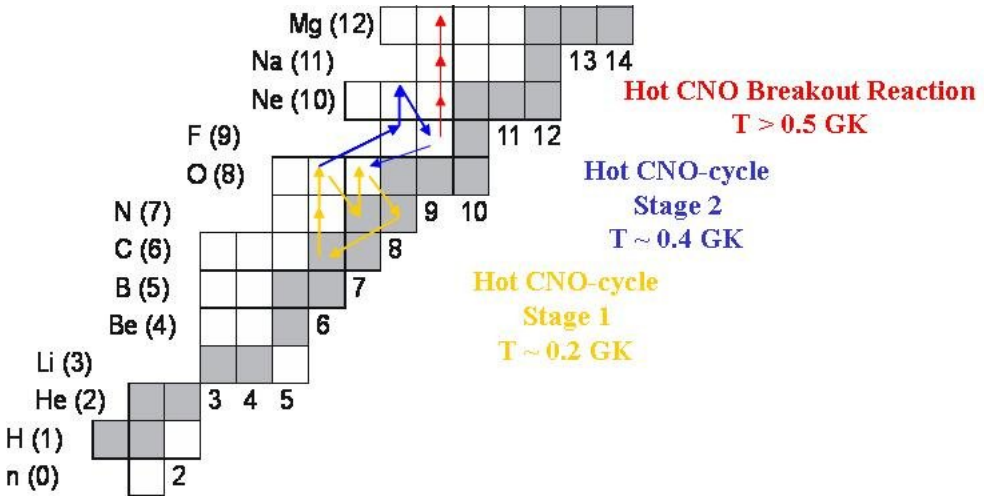

Figure 1.10: *Diagram illustrating the paths of the two possible ^{18}F + p reactions. The blue arrows shows the return/continuation of the HCNO cycle as a result of the the $^{18}F(p,\alpha)^{15}O$ reaction. The red arrow shows the $^{18}F(p,\gamma)^{19}Ne$ reaction path which, eventually may lead to the onset of rp-process.*

1.6.2 ^{18}Ne(α,p)^{21}Na

The ^{18}Ne(α,p)^{21}Na reaction is believed to provide a possible breakout route from the hot CNO cycle to the NeNa cycle, which, in turn, will eventually lead to the *rp*-process (Figure 1.11).

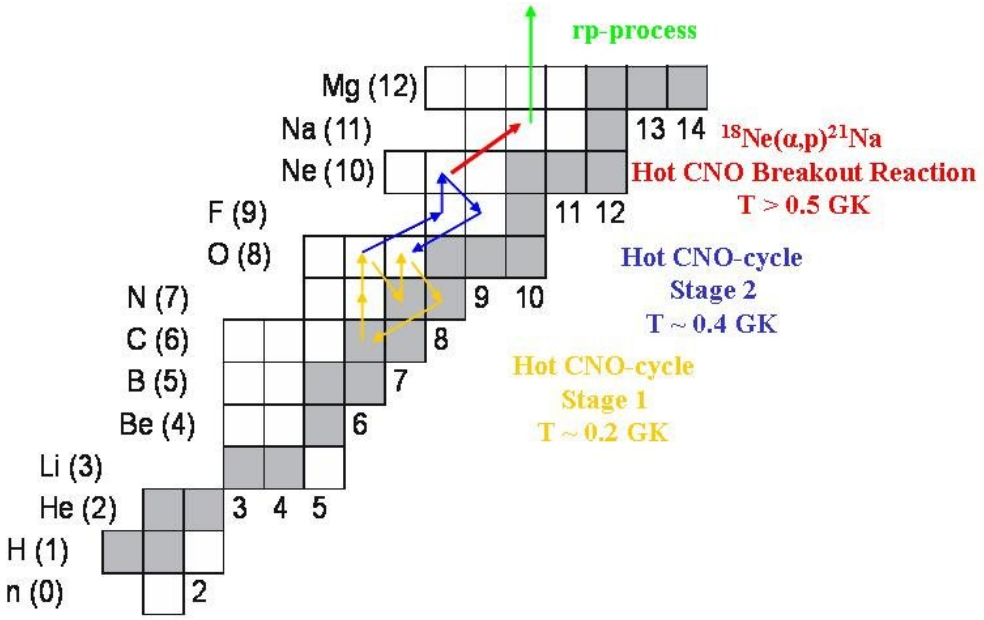

Figure 1.11: *HCNO break-out reaction path for the ^{18}Ne(α,p) reaction.*

The mean survival time of ^{18}Ne in a stellar environment depends on the physical conditions of density, temperature and pressure. The two competing destructive reactions for ^{18}Ne are ^{18}Ne(α,p) and its beta-decay, ^{18}Ne(β^+ ν) are best illustrated by Figure 1.12. The thick locus indicates the stellar conditions in which the mean lifetime of the isotope is equal for the two destructive processes. It is important to note that the data used to calculate the reaction rates for the ^{18}Ne(α,p) are based on resonances measured experimentally above $E_{\mathrm{CM}} =$ 2.5 MeV, corresponding to a stellar temperature of $T_9 \sim 2.9$ (higher than the expected stellar conditions), and as such does not include transitions from below this energy. Transitions resulting from below this energy will result in the locus shifting towards lower densities and temperatures.

There is some debate as to whether a hot-CNO break-out occurs within novae. If the reaction does indeed occur at nova sites then it plays a part in the nucleosynthesis of heavier elements and their astrophysical abundances. The reaction is of particular importance within X-ray bursters as the thermonuclear runaway which it leads to, provides the energy for driving the explosion.

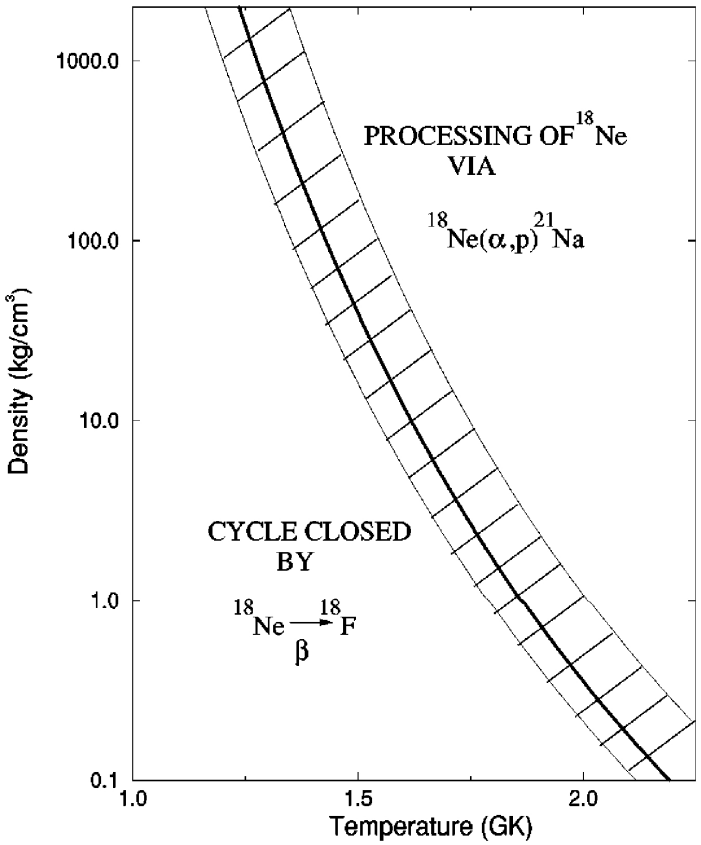

Figure 1.12: *Plot illustrating the effects of temperature and density on the determination of which reaction,^{18}Ne(α,p) or ^{18}Ne(β^+,ν), will dominate the destruction of ^{18}Ne [22]*

1.7 Thesis Outline

The remainder of this thesis will have the general outline detailed below.

Chapter 2 continues with an outline of the theory used to calculate stellar reaction rates and a brief description of R-matrix theory.

The scientific motivation and previous experiments relevant to the two reactions studied will be discussed in Chapter 3.

The experimental details of the two reactions studied will be presented in Chapter 4. Although the objectives and methodology were quite different, many of the experimental setups were very similar and so both will be discussed in the same chapter.

Chapters 5 and 6 are given over to the data analysis and results of the ^{15}O(α,α) experiment with Chapters 7 and 8 doing the same for the ^{18}Ne(α,p) reaction.

Finally, the conclusions of the work undertaken are presented in Chapter 9 and some suggestions for possible future experimental work as a consequence of the results obtained are made.

Chapter 2

Theoretical Model of Stellar Reaction Rates

The first part of this chapter is given over to the discussion of the basic theoretical model necessary to calculate the rate of a given stellar reaction. This is followed by a brief description of the R-matrix formalism which was used to fit the resonant elastic scattering experimental data.

2.1 Stellar Reaction Rates

2.1.1 The Maxwell - Boltzmann Velocity Distribution

The reactions studied in this thesis occur in non-degenerate stellar environments. The fully ionised plasma occurring in these environments is made up of a range of isotopes and free electrons and, because it is not degenerate, it is in thermodynamic equilibrium. The velocity distribution of the constituent particles, therefore, can be described by the Maxwell - Boltzmann distribution.

$$\phi(v) \;=\; 4\pi v^2 \left(\frac{m}{2\pi kT}\right)^{\frac{3}{2}} \exp\left(-\frac{mv^2}{2kT}\right) \tag{2.1}$$

where m is the mass of the nucleus of interest, T is the temperature (K) of the gas and $\frac{1}{2}mv^2$ is the kinetic energy of the nucleus.

In terms of energy this can be written:

$$\phi(E) \propto E \exp\left(-\frac{E}{kT}\right) \tag{2.2}$$

with the most probable value of kinetic energy being equal to kT, Figure 2.1.

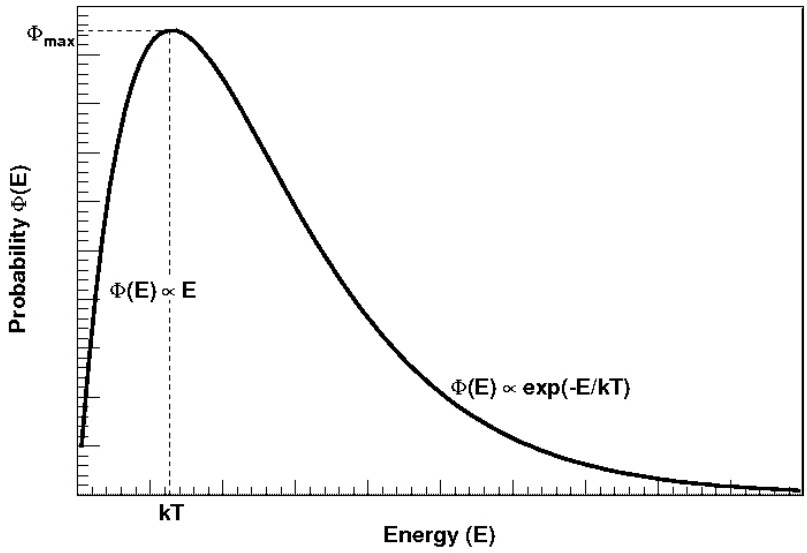

Figure 2.1: *Diagram illustrating the Maxwell-Boltzmann distribution. The most likely energy occurs at $E = kT$.*

2.1.2 Penetrating the Barrier

Within the high temperature stellar environment for the following general reaction to take place

$$a \ + \ A \ \longrightarrow \ b \ + \ B \tag{2.3}$$

the two positively charged nuclei, a and A, must overcome the repulsive Coulomb force. The Coulomb force is proportional to the product of the respective nuclear charges and results in a potential barrier. This Coulomb barrier must be penetrated for the fusion to take place and takes the form

$$V_C(r) \ = \ \frac{Z_a Z_A e^2}{4\pi\epsilon_0 r} \tag{2.4}$$

where $V_C(r)$ is the Coulomb potential, Z_a and Z_A represent the integral charges of the interacting nuclei and r the distance between them.

If examined classically, the typical energies needed for the fusion of light nuclei are of the order of a few hundred keV, which corresponds to a stellar temperature $T \sim 10^9$ K (from E=kT). For example, the Coulomb barrier for the $p + p$ reaction is ∼550 keV, which can only be achieved at a stellar temperature

of $T_9 = 6.4$. The typical temperature of the stellar core (in the case of the Sun) is $T_9 = 0.0136$. It can be seen from the example that the typical energies of nuclei in the stellar environment are a great deal smaller than that of the Coulomb barrier.

George Gamow [23], however, showed that if treated quantum mechanically there is a small but finite probability that a particle with $E < E_C$ can penetrate the potential barrier via the quantum-tunnelling effect (Figure 2.2). The probability that the nucleus will tunnel through the barrier is given by:

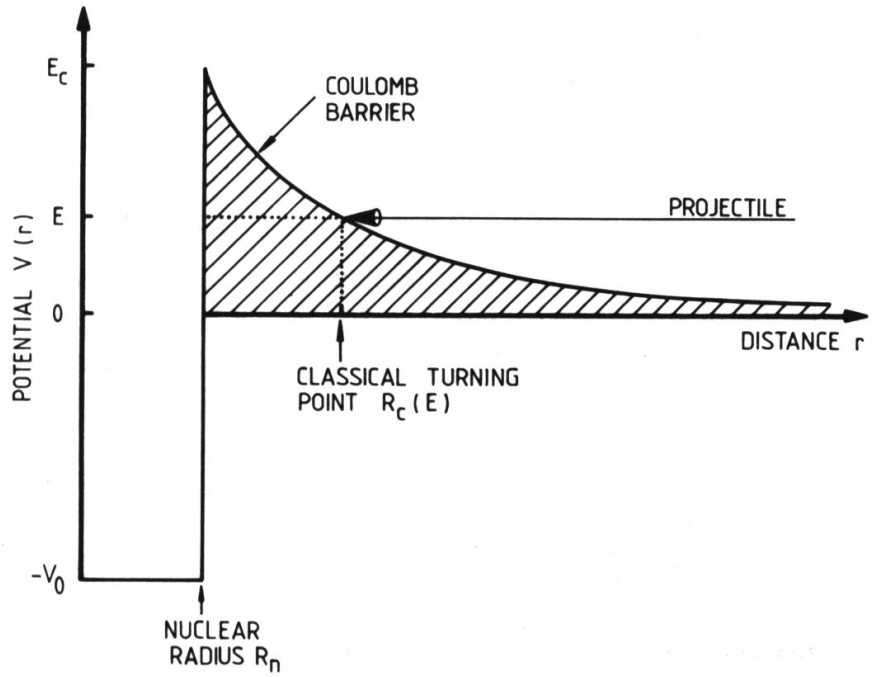

Figure 2.2: Schematic representation of the combined nuclear and Coulomb potential. Classically a projectile with $E < E_C$ would reach the turning point R_C. However, treated quantum mechanically a projectile can reach the nuclear domain. Image taken from *[8]*.

$$P = \frac{|\psi(R_n)|^2}{|\psi(R_c)|^2} \tag{2.5}$$

where$|\psi(R_n)|^2$ is the wave function at the nuclear radius R_n and $|\psi(R_c)|^2$ the wave function at the classical turning point R_c.

Solving the Schrödinger equation for the Coulomb potential and approximating at low energies, where $E \lll E_C$ and the classical turning point R_c is much larger than the nuclear radius R_n, equation 2.5 can be approximated to:

$$P = exp(-2\pi\eta) \tag{2.6}$$

where η, the Sommerfeld parameter is given by:

$$\eta = \frac{Z_a Z_A e^2}{4\pi\epsilon_0 \hbar v} \tag{2.7}$$

For each nucleus, one may associate a geometrical area, which is directly related to the probability of a projectile interacting with that nucleus. This area is known as the cross-section ($\sigma(E)$). The cross-section drops rapidly for energies below the Coulomb barrier due to the exponential nature of Equation 2.6 as well as being inversely proportional to energy ($\pi(\frac{\lambda}{2\pi})^2 \propto \frac{1}{E}$) accounting for the de Broglie wavelength of the particle. From the two relations stated, the cross section can be expressed as:

$$\sigma(E) = \frac{1}{E}\exp(-2\pi\eta)S(E) \tag{2.8}$$

where *S(E)* is the astrophysical S-factor, which contains all the nuclear effects. It is used to extrapolate measured cross-sections down to astrophysical energies as, for non-resonant reactions, it is a smoothly varying function of energy.

2.2 Reaction Rates

For the interaction expressed in Equation 2.3, the reaction rate can be generalised as:

$$r_{aA} = N_a N_A \int_0^\infty vP(v)\sigma(v)dv \equiv N_a N_A \langle\sigma v\rangle_{aA} \tag{2.9}$$

where $\langle\sigma v\rangle_{aA}$ is the reaction rate per particle per pair and $N_a N_A$ the total number density of pairs of non-identical nuclei a and A.

As shown in Figure 2.1 the velocity distribution has a maximum at $E = kT$ and is equal to $v_T = \sqrt{2kT/m_{aA}}$. The reaction rate per particle pair can be written in terms of energy as:

$$\langle\sigma v\rangle_{aA} = \left(\frac{8}{\pi\mu}\right)^{1/2} \frac{1}{(kT)^{3/2}} \int_0^\infty E\sigma(E)\exp\left(-\frac{E}{kT}\right)dE \tag{2.10}$$

where μ is the reduced mass of the particle pair.

2.2.1 Non-resonant reaction rates and the Gamow Peak

Combining equations 2.8 and 2.10 gives the reaction rate for non-resonant reactions. If examined at a specific temperature, and as a result assuming *S(E)* is constant, the reaction rate has the form:

$$\langle \sigma v \rangle_{aA} = \left(\frac{8}{\pi\mu}\right)^{1/2} \frac{1}{(kT)^{3/2}} S(E_0) \int_0^\infty \exp\left(-\frac{E}{kT} - \frac{b}{E^{1/2}}\right) dE \tag{2.11}$$

where b[1], due to the barrier penetrability term, is:

$$b = (2\mu)^{1/2} \pi e^2 Z_a Z_A / \hbar \tag{2.12}$$

The product of the Maxwell-Boltzmann and the Coulomb factors results in a peak of the integral near energy E_0[2] (see Figure 2.3). This peak is known as the Gamow Peak and is detailed in Figure 2.3.

2.2.2 Resonant Reaction Rates

The equation for the reaction rate given above is for non-resonant reactions only, as it relies on an (assumed) constant S-factor over a given energy. This same assumption cannot be made with regards to a resonant reaction. A resonant reaction is one in which there is a rapid increase/decrease in cross-section over a small energy range. A resonant reaction proceeds via a *Compound nucleus*(C)[3]:

$$a \ + \ A \ \longrightarrow \ C \ \longrightarrow \ b \ + \ B \tag{2.13}$$

The reaction will only occur if the energy of the entrance channel, the fusion of a and A, matches to an excited state in the compound nucleus C. This subsequently decays to the reaction products b and B. An isolated resonance is described by the Breit-Wigner formula:

$$\sigma_{BW}(E) = \frac{\lambda^2}{4\pi} \frac{2J+1}{(2J_a+1)(2J_A+1)} (1+\delta_{aA}) \frac{\Gamma_a \Gamma_A}{(E_r - E)^2 + \Gamma^2/4} \tag{2.14}$$

where $J_a$and J_A are the spins of the projectile and the target,J and E_r are the spin and energy of the resonance, Γ_a and Γ_A the partial widths of the resonances

[1] b^2 is known as the Gamow energy E_G

[2] Effective mean energy for thermonuclear fusion reactions at a given temperature T

[3] A compound nucleus is formed when the two interacting nuclei form a single excited nucleus. It is relatively long lived and has no 'memory' of how it was formed (Independence Theorem)

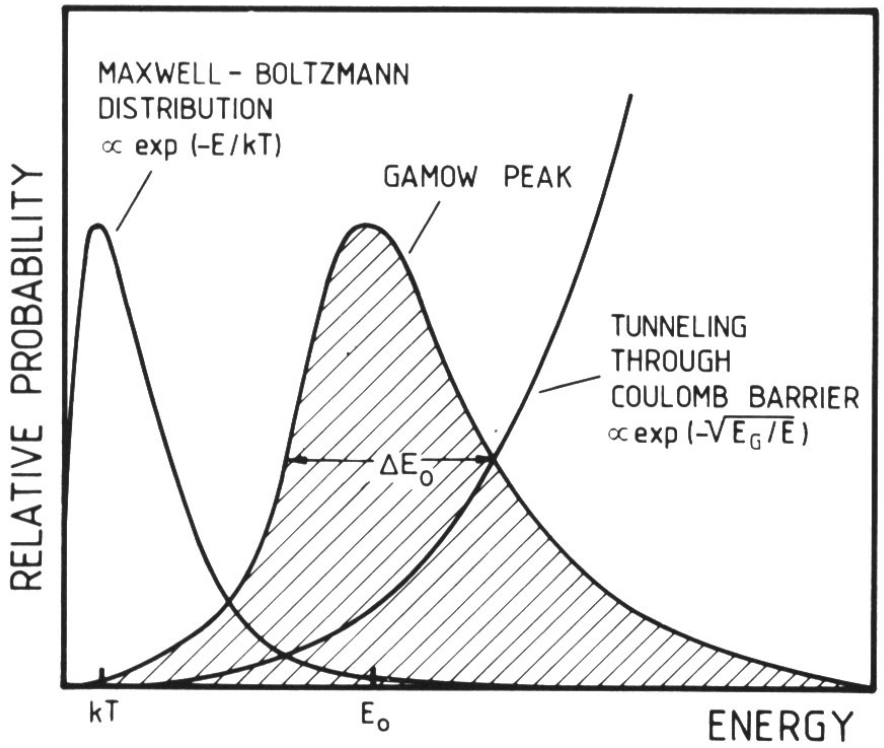

Figure 2.3: *Diagram showing both the Maxwell-Boltzmann distribution and the Coulomb function. Also shown is the product of the two, the Gamow Peak, which peaks near the energy E_0. Taken from [8].*

and Γ the total resonance width. The $(1 + \delta_{aA})$ term is included as the cross-section will increase by a factor of 2 for identical particles.

A resonance is defined to be narrow if its width, Γ, is a great deal smaller than its energy, E_{r}. A qualitative description of this is given by [8]:

$$\frac{\Gamma}{E_r} \ll 10\,\% \tag{2.15}$$

To calculate the reaction rate for narrow resonances the combination of equations 2.10 and 2.14 result in:

$$\langle \sigma v \rangle_{aA} = \frac{\sqrt{2\pi}\,\hbar^2}{(\mu kT)^{3/2}}\,\omega \int_0^\infty \frac{\Gamma_a \Gamma_A}{(E_r - E)^2 + \Gamma^2/4}\,\exp(-\frac{E}{kT})\,dE \tag{2.16}$$

where ω, the spin statistical factor, is:

$$\omega = \frac{(2J+1)}{(2J_a+1)(2J_A+1)}(1 + \delta_{aA}) \tag{2.17}$$

For resonances which satisfy this condition, it can be assumed that the partial widths and the Maxwell-Boltzmann factor are constant over the total resonance width. Thus, the reaction rate can be calculated analytically:

$$\langle \sigma v \rangle_{aA} = \left(\frac{2\pi}{\mu kT}\right)^{3/2} \hbar^2 \exp(-\frac{E_r}{kT})\omega\gamma \tag{2.18}$$

where $\omega\gamma$ is known as the resonance strength and is given by:

$$\omega\gamma = \omega\frac{\Gamma_a \Gamma_A}{\Gamma} \tag{2.19}$$

If the reaction rate depends on several narrow resonances, their contributions are summed to give a total reaction rate:

$$\langle \sigma v \rangle_{aA} = \left(\frac{2\pi}{\mu kT}\right)^{3/2} \hbar^2 \sum_i \exp(-\frac{E_i}{kT})(\omega\gamma)_i \tag{2.20}$$

2.3 *R*-Matrix Theory of Compound Nuclear Reactions

In the previous section the derivation of the Breit-Wigner formula was shown. In principle, one can parametrise the Breit-Wigner formula and fit it to an experimental cross section in order to gain information about a resonance's energy

and width. However, this formalism is limited as it only allows for the study of an isolated resonance being populated and decaying in the same manner. This is shown schematically in Figure 2.4.

The R-matrix formalism, however, allows for the simultaneous study of multiple states (channels) in the compound nucleus, thus incorporating multiple methods of population and decay. Figure 2.5 illustrates this for pure elastic reactions. It is important to note that the R-matrix formalism will simplify to the Breit-Wigner formula for a single channel case.

As well as elastic reactions there are inelastic and reaction channels open. Figure 2.7 illustrates examples of inelastic channels open in the ^{15}O(α,α) reaction.

The possible reaction channel amplitudes are then compiled into a matrix, the R-matrix. The R-matrix is a function of energy and is given by [24]:

$$R_{cc'} = \sum_{\lambda} \frac{\gamma_{\lambda c}\gamma_{\lambda c'}}{E_\lambda - E'} \tag{2.21}$$

where cc' label the incoming and outgoing channel (for elastic scattering c=c'), E_λ the pole energies, $\gamma_{\lambda c}$ the reduced width[1] amplitudes, λ is the level label.

The principal application of the R-matrix formalism in nuclear astrophysics is to parametrise some experimentally known quantities with a small number of parameters. These parameters can then be used to calculate σ and extrapolate σ to low energies. The parameters are known as *poles* and correspond to resonances, and are related to experimental parameters but not equal to them.

The R-matrix approach allows for exploration of interference effects arising from states of the same spin and parity in the compound nucleus when considering the inelastic reaction channels. In purely elastic reactions the interference arises from Coulomb scattering with the effect of a state interfering with itself. They can either interact constructively (their amplitudes sum), or destructively (amplitudes subtract). For elastic scattering from multiple states the amplitudes are simply summed.

The main application of the R-matrix formalism is as a means of extracting the angular momentum and parity of nuclear states. The R-matrix can be parametrised and fitted to experimental data. The fitted parameters then

[1]The reduced width has the advantage of removing the energy dependence from the partial width. This is very useful for comparison of width between a nucleus and its mirror as the reduced widths for analogous states should be similar.

provide information on the underlying reaction channels and can be used to calculate the properties of the resonances.

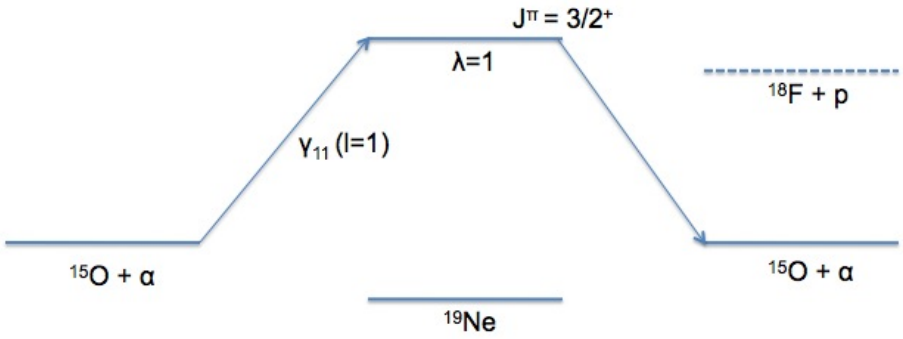

Figure 2.4: *Schematic of single resonance in compound nucleus for an elastic reaction.*

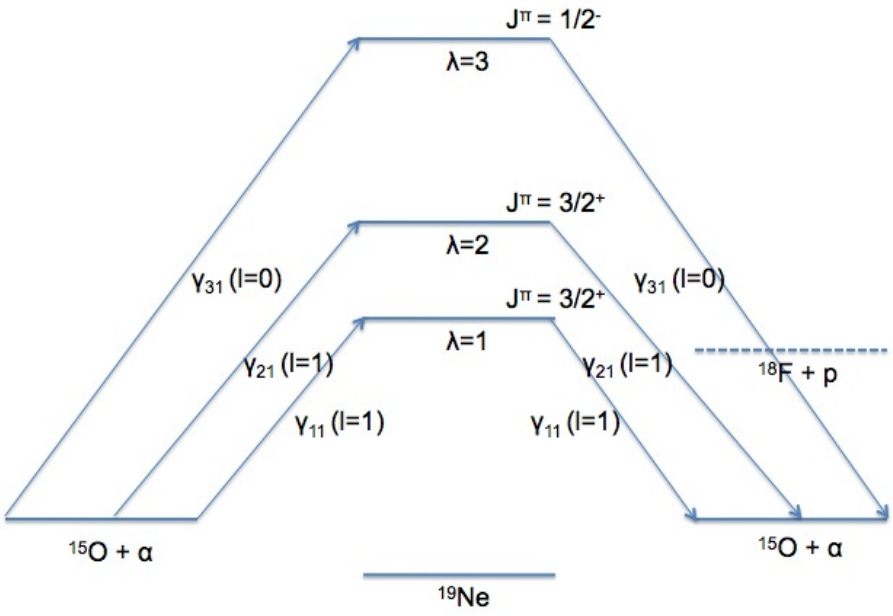

Figure 2.5: *Schematic of multiple resonances being populated in compound nucleus for an elastic reaction.*

The main idea is to divide the nuclear area into two regions, Figure 2.8:

1. The Internal Region: $r \leq a$: Nuclear and Coulomb Interactions
2. The External Region: $r \geq a$: Coulomb Interaction Only

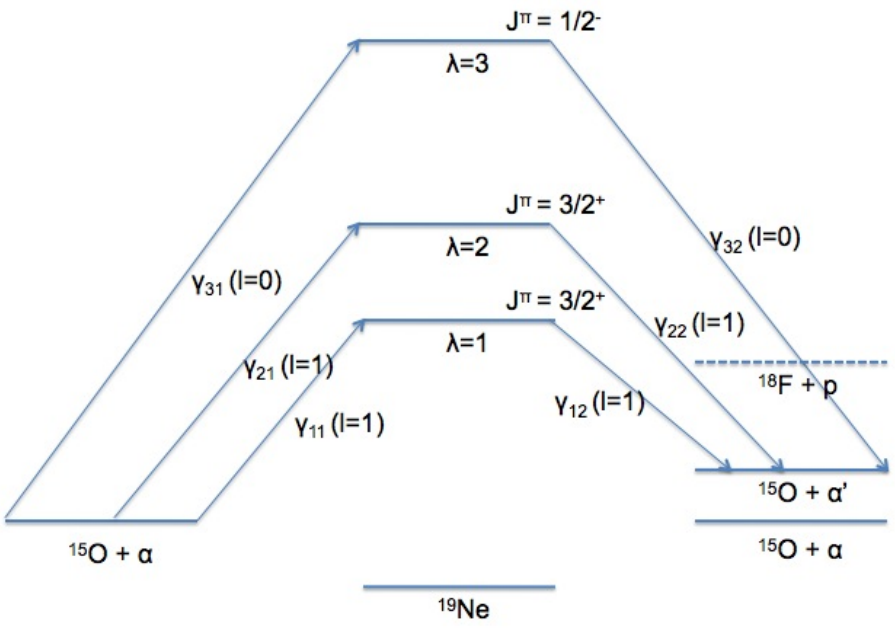

Figure 2.6: *Schematic of multiple resonances being populated in compound nucleus for an inelastic reaction.*

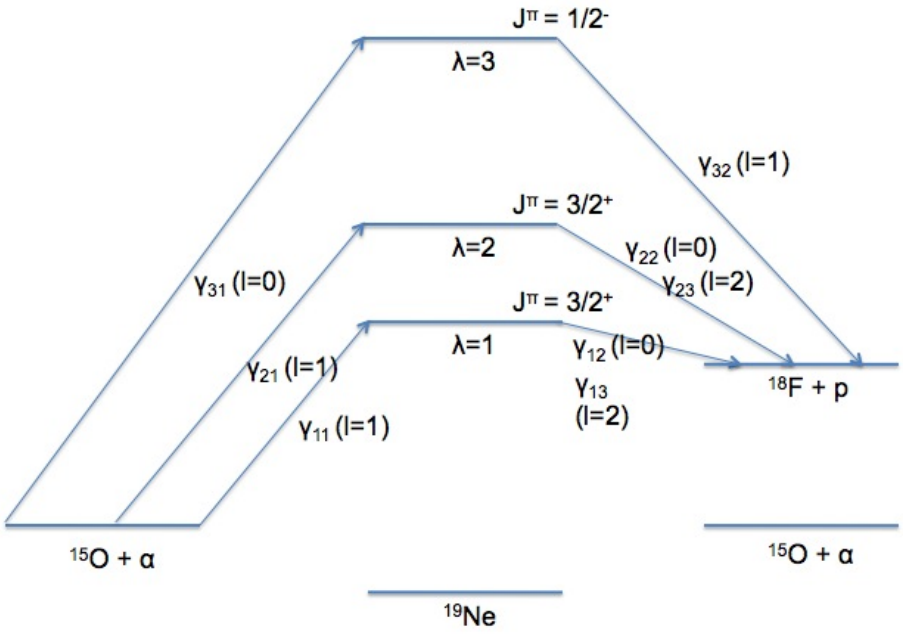

Figure 2.7: *Schematic of multiple resonances being populated in compound nucleus for a direct reaction.*

where a is the boundary radius and known as the *channel radius*. It is generally the smallest separation distance of the nuclear pair for which the nuclear potential is negligible. Generally:

$$a = r_0(A_t^{1/3} + A_p^{1/3}) \tag{2.22}$$

with radius parameter r_0 between 1.0 - 1.5 fm.

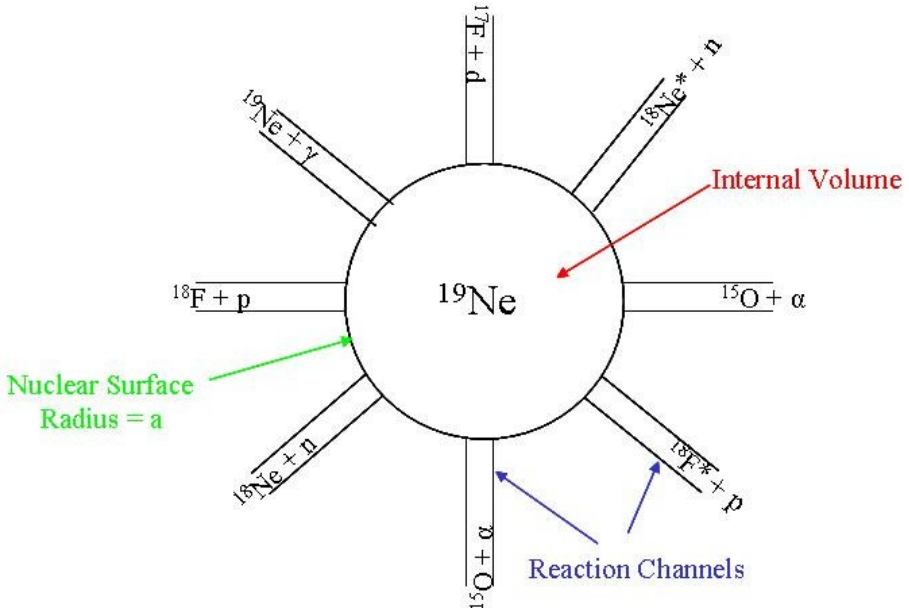

Figure 2.8: *Two dimensional schematic of configuration space for the R-matrix formalism. Only a handful of possible channels are shown.*

In practice the R-matrix formalism is limited to low energy data where the level density is low, as the J^π of each state must be considered individually. It is thus well suited to nuclear astrophysical scenarios.

In a physical scenario an 'observed' resonance will have an energy (E_r) and, a partial width (Γ_b) associated with it. The partial width may also be expressed as a *reduced* width, γ^2:

$$\Gamma_b = 2\gamma^2 P(E_r) \tag{2.23}$$

where $P(E_r)$is known as the *Penetration Factor*.

The R-Matrix equivalent parameters (*poles*), are $\bar{\mathrm{E}}_r$ and γ_b^2 and are both dependent on the channel radius.

2.4 Hauser-Feshbach Statistical Model

In the previous sections the methods of calculating reaction rates and cross-sections has examined the case of isolated narrow resonances. These methods are sufficient when dealing with low energy regions of excited nuclei, however, as the excitation energy increases the level density of the states increase as do their widths.

As the density increases the effect of individual resonances on the cross-section dissipate until the cross-section varies smoothly as a function of energy. To describe this *continuum* effect a statistical approach is necessary, one such technique is Hauser-Feshbach theory [25].

Chapter 3

Scientific Motivation and Previous Experiments

3.1 $^{15}O(\alpha,\alpha)^{15}O$

The abundance of ^{18}F following a nova event depends upon the rate of its synthesis and destruction. The rates of the destructive ^{18}F + p reactions depend on the spectroscopic properties of states in the compound nucleus ^{19}Ne. Investigations of the level structure of ^{19}Ne can therefore provide valuable insight into the abundance of ^{18}F following a nova.

There are various experimental methods which can be employed to determine the reactions rates of ^{18}F(p,α) and ^{18}F(p,γ). For instance, one could measure the cross sections directly via inverse kinematics, such as in [26; 27; 28; 29]. Other methods employed involved studying the reaction indirectly, through the population and subsequent decay of the compound nucleus ^{19}Ne [30; 31], through transfer reactions [32], via the elastic scattering reaction ^{18}F(p,p)^{18}F [33; 34] and examination of the compound mirror [1] nucleus ^{19}F [1; 35].

The ^{15}O(α,α)^{15}O elastic scattering experiment probes the level structure of ^{19}Ne above the alpha threshold (^{19}Ne E_x = 3.5291 MeV). The ^{15}O(α,α)^{15}O reaction is particularly suited to studying states near the ^{18}F + p threshold, for example, the possible $\frac{3}{2}^+$ state at E_r at 8 keV, which are difficult to access by the ^{18}F + p reaction. This will allow for the study of the energies and α widths of the states at and above the ^{18}F+p threshold (^{19}Ne E_x = 6.411 MeV).

[1] Mirror nuclei are those with the same mass number but with the respective number of protons and neutrons inverted. Such nuclei share similar spectroscopic properties.

3.1.1 ^{19}Ne

Figure 3.1 shows the level structure of the compound nucleus ^{19}Ne and its mirror ^{19}F at and above the proton threshold of ^{19}Ne, the region covered by this work.

The data illustrated in the level scheme have been taken from [36], a compilation of results, giving the most recent spectroscopic values for ^{19}Ne.

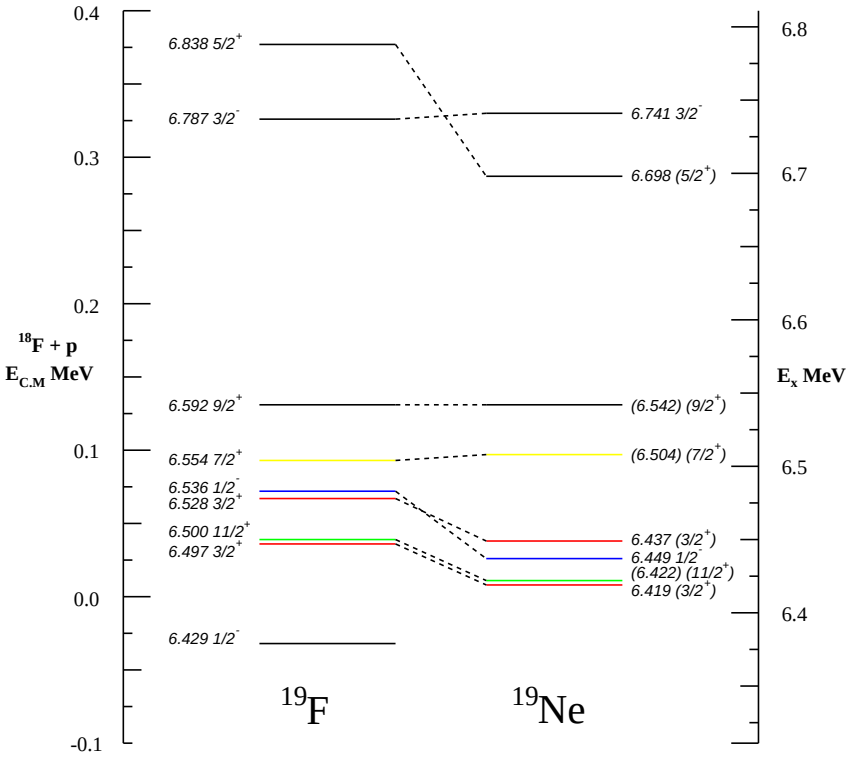

Figure 3.1: *Level scheme of ^{19}Ne and ^{19}F at and above ^{18}F+p threshold, E_x = 6.411 MeV. All values are taken from [36] bar the $\frac{1}{2}^-$ below the ^{18}F + p threshold, which, is taken from [37]*

Despite the ^{18}F+p threshold being ∼3 MeV higher than the α separation energy, the level density is sparse enough for individual resonances to have importance [10].

In nuclear astrophysical scenarios reaction rates will be dominated by *s*-wave transitions due to their low energy nature. The low momentum transfer

transitions in the ^{18}F + p reactions are believed to populate those states with low spins in ^{19}Ne, namely $J = \frac{3}{2}$ and below.

In view of this the experiment carried out aimed to study the region up to $E_x = 6.6991$ MeV corresponding to $E_r = 0.2881$ MeV, with the principal aim to study the possible $\frac{3}{2}^+$ doublet at $E_r = 8$ and 38 keV.

3.1.2 Current limitations and uncertainties

1. There are no experimental measurements of alpha widths for these two states. To date the alpha widths have been inferred from the mirror nucleus ^{19}F. It has been shown that alpha widths in ^{19}Ne theoretically inferred from states in its mirror ^{19}F, have differed by as much as an order of magnitude from experimentally measured alpha widths in ^{19}Ne [38].

2. With the small energy difference between the states (30 keV), coupled with their errors (∼6 keV [36]), one cannot make any direct conclusions regarding the two $(3/2)^+$ states at 8 and 38 keV. Could they be inverted with respect to the ^{19}F mirror states? Are they both above the ^{18}F + p threshold considering the errors associated with each state?

3. In (p,α) reactions states with the same parity may interfere, however, it is not known *a priori* if this interference is constructive or destructive. The ^{15}O(α,α) reaction will not give any indication of the shape of the interference but the resonance parameters extracted will allow for investigation of their influence on interference effects.

3.1.2.1 Interference Effects

Interference effects arise between states of the same parity and can be either constructive or destructive. An interference between two states is labelled constructive if the contributions in the collision matrix sum, destructive if they subtract. A more formal description is given in section 2.3.

Interference effects between the $\frac{3}{2}^+$ states at 8, 38 and 665 keV are shown in Figure 3.2. As three states are being examined there are eight distinct interference combinations, of which four are shown. For each scenario the R-matrix

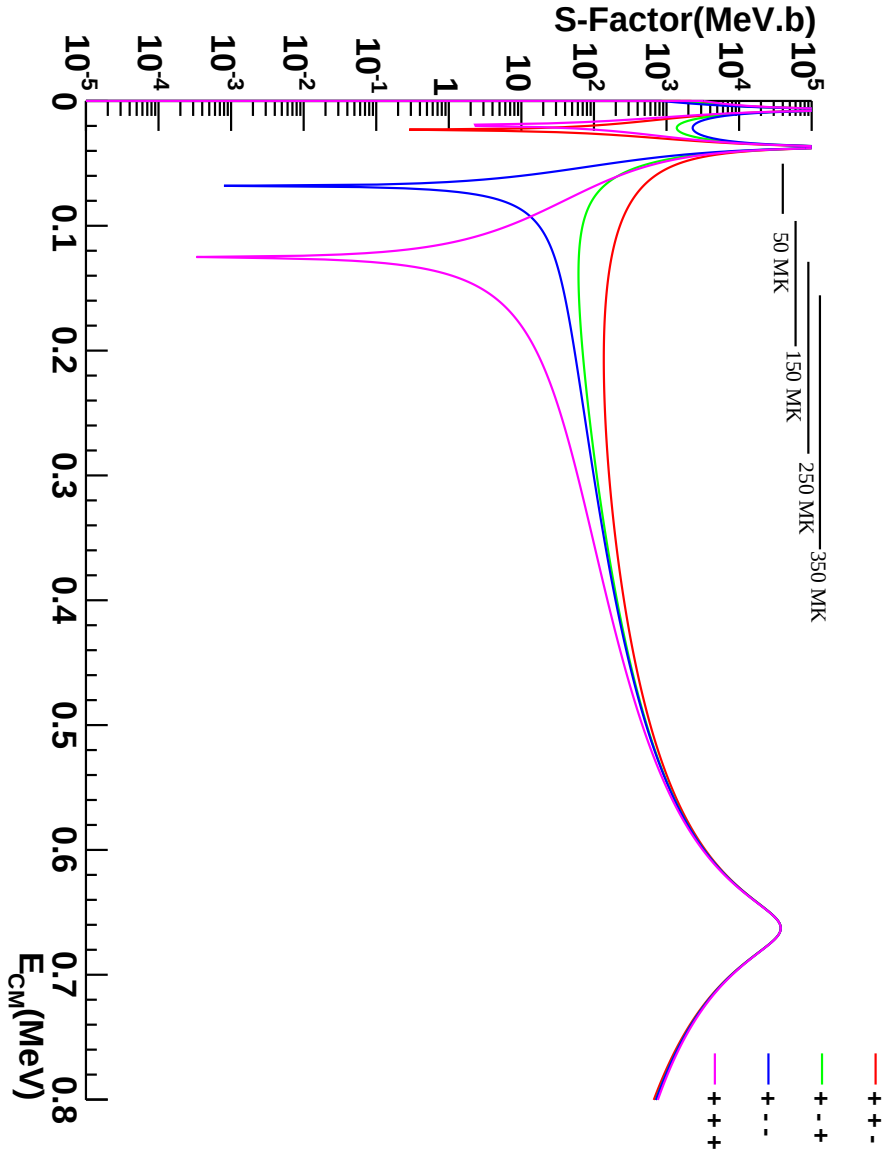

Figure 3.2: *Interference effects on the S-factor for the $^{18}F(p,\alpha)$ reaction. For each case the only factor that has been altered is the interference effect. The nuclear radius has been kept constant at 5.5 fm with nominal values for Γ_p and Γ_α taken from [36]. The temperature scales (top left) illustrate the Gamow energy window for the quoted temperatures. The area of interest for this reaction is therefore below E_{CM}=0.4 MeV as this corresponds to the astrophysical temperature range of interest.*

nuclear radius is set at 5.5 fm, with the resonance energies and widths, Γ_p and Γ_α, taken from [36]. The only parameter that is altered is the interference sign.

As can be seen the S-factor and, therefore the cross-section for the reaction plummets for the two cases (+++) and (+--). Astrophysically this would correspond to a scenario where the ^{18}F is not destroyed at such a high rate which therefore increases the probability of observation via the current generation gamma ray observatories such as INTEGRAL.

Figures 3.3 and 3.4 show the effect of an order of magnitude change in Γ_α widths on the S-factor for +-+ and +++ interference respectively.

3.2 ^{18}Ne(α,p)^{21}Na

As discussed in Section 1.6.2 the determination of the rate of this reaction is key to a better understanding of the HCNO breakout and is the primary motivation for studying this reaction. Previous attempts to measure the reaction have produced ambiguous results and it is the goal of this new experiment to attempt to resolve these discrepancies.

The first direct measurement of the ^{18}Ne(α,p) reaction used a helium-filled chamber [39] and covered an energy range between E_{CM} = 2.04 - 3.01 MeV. These measurements were extended to E_{CM} = 1.7 - 2.9 MeV [40][1]. Both experiments were performed using the same experimental technique. A ΔE-E detector telescope housed within a helium-filled chamber was used to detect the reaction protons of interest. The data were corrected for energy losses and converted to centre of mass energies, with E_{CM} of the interaction determined by tracking the proton back to its point of origin in the target. The data were fitted with Lorentzian functions, identifying excited states in ^{21}Na, with resonance energies, alpha widths, spins and parities identified in the compound nucleus ^{22}Mg. These results are shown in Table 3.1 with calculated spectroscopic factors.

The most recent study of ^{18}Ne(α,p) was investigated using the time-reverse reaction ^{21}Na(p,α)^{18}Ne [41; 42]. A ^{21}Na beam bombarded a 370 μg/cm^2 (CH_2) target. The ^{18}Ne and ^{21}Na ions were detected with an ionisation chamber with the α particles and protons detected in coincidence with silicon detectors.

[1] The energy range covered is a result of the experimental limitation of low beam intensity and corresponds to temperatures above those of astrophysical interest.

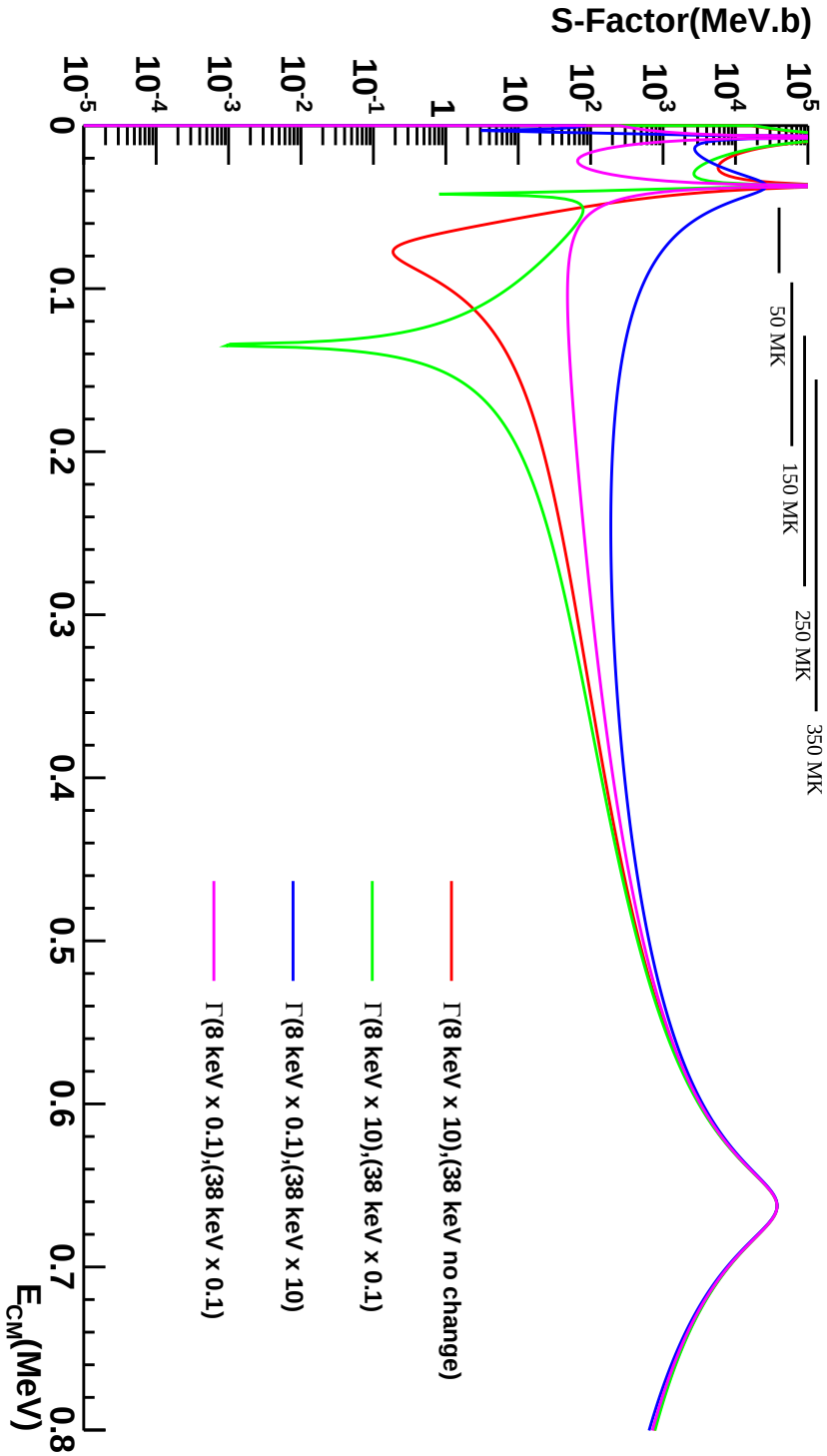

Figure 3.3: *Effect on S-factor for the $^{18}F(p,\alpha)$ reaction when increasing/decreasing nominal widths of 8 and 38 keV resonances by factors of 10 for +-+ interference. S-factor calculated from nominal widths is shown as green line in Figure 3.2*

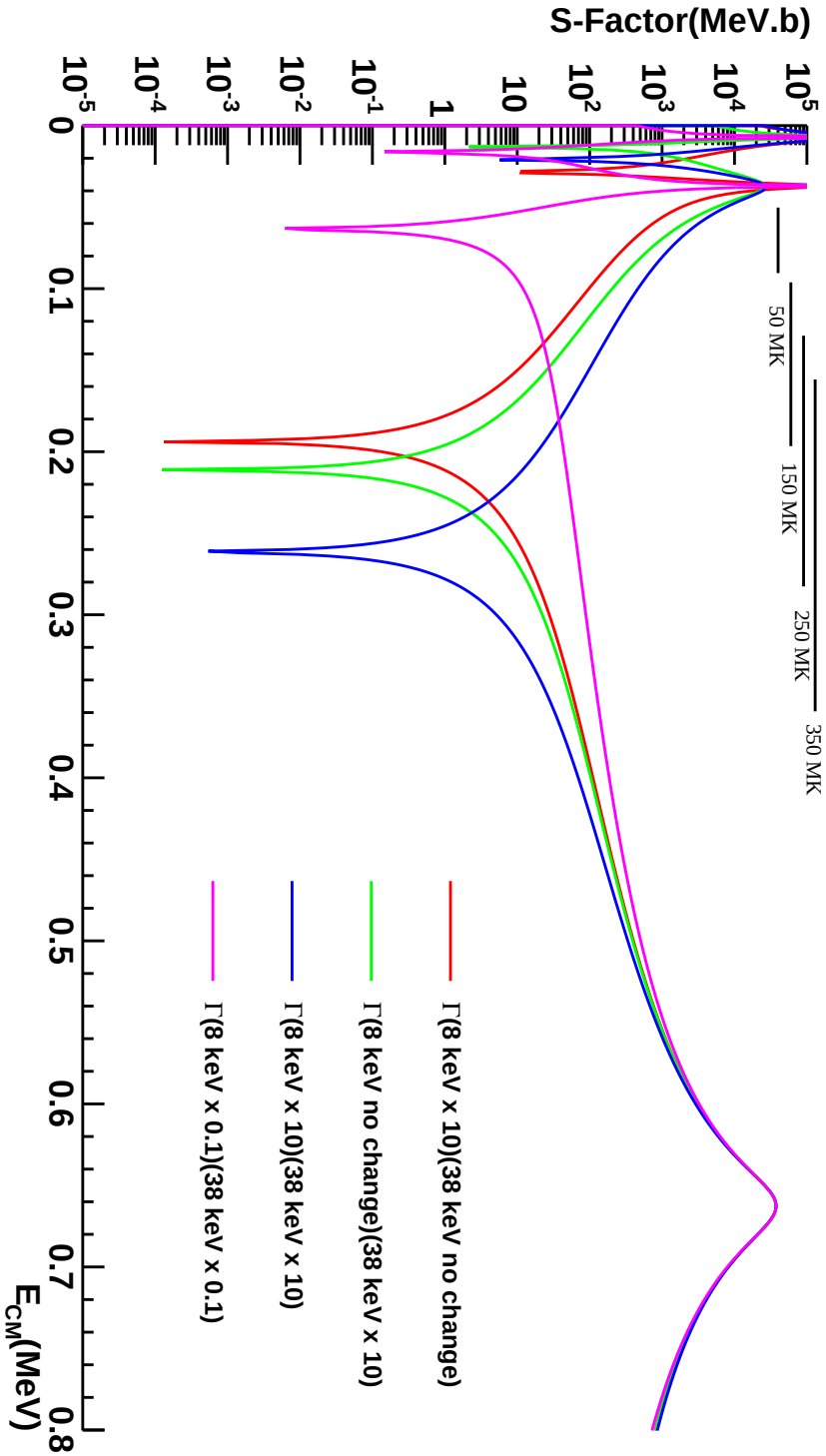

Figure 3.4: *Effect on S-factor for the $^{18}F(p,\alpha)$ reaction when increasing/decreasing nominal widths of 8 and 38 keV resonances by factors of 10 for +++ interference. S-factor calculated from nominal widths is shown as pink line in Figure 3.2*

Table 3.1: Results and reduced single particle widths for [40]. The reduced single particle widths shown were calculated with [43] and did not appear in the original Groombridge *et al* ([40]) publication

E_x(MeV)	E_r(MeV)	Γ_α(MeV)	J^π	θ^2(%)
10.12	1.98	0.1	2^+ (3^-, 5^-)	2.16×10^3
10.31	2.17	0.13	2^+ (3^-, 5^-)	1.07×10^3
10.42	2.28	0.21	2^+ (1^-, 3^-)	1.06×10^3
10.55	2.41	0.16	2^+ (3^-, 5^-)	4.81×10^2
10.66	2.52	0.1	2^+ (1^-, 3^-)	2.02×10^2
10.86	2.72	0.21	0^+ (1^-)	2.24×10^2
10.92	2.78	0.12	2^+ (1^-, 3^-)	1.07×10^2
11.01	2.87	0.1	2^+ (1^-, 3^-)	7.04×10^1

Figure 3.5 shows the excitation function of the ^{18}Ne(α,p) reaction plotted as a function of excitation energy in the centre of mass energy system of ^{18}Ne + α for each of the previous experiments.

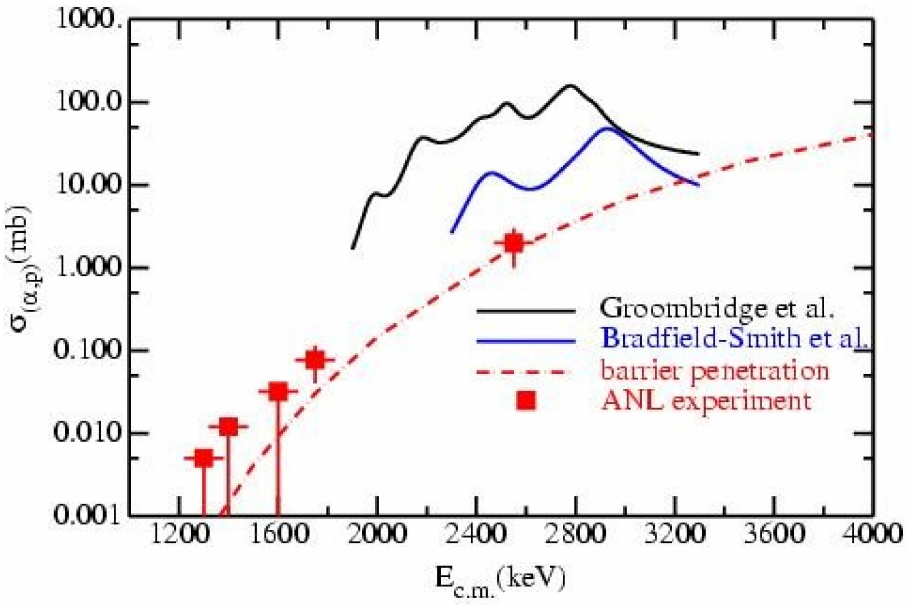

Figure 3.5: *Excitation function of the ^{18}Ne(α,p) reaction. The solid lines detail the experiments of [40] and [39]. The dashed curve is the calculated barrier penetration normalised to the highest energy point of [42]. This figure has been taken from [42]*

3.2.1 Limitations

From Figure 3.5 it can be seen that at $E_{\mathrm{CM}} = 2.5$ MeV the cross-section obtained by Sinha *et al* (ANL experiment) was a factor of $\sim 50\times$ smaller than had been reported by Groombridge et al [40]. Although a smaller cross-section would be expected for the time-reverse reaction, as inelastic channels will not contribute, a factor of ~ 50 is larger than anticipated.

It can also be seen from table 3.1 that the calculated reduced single particle width for each state reported by Groombridge *et al.* is unphysical. These were calculated with [43].

The discrepancy between the two reactions and the unphysical nature of the results from previous direct experimental approaches motivate and warrant a new, simple measurement. The energy points at $E_{\mathrm{CM}} = 1.7$ and 2.5 MeV were chosen for investigation to allow for direct comparison with previous measurements.

3.2.2 ^{22}Mg

The compound system ^{22}Mg was most recently studied via the ^{24}Mg(p,t)^{22}Mg reaction [44]. The experiment made use of the Grand Raiden spectrometer at RCNP Osaka [45]. A 100 MeV proton beam bombarded a 0.82 mg cm^{-2} enriched ^{24}Mg target with reaction tritons detected using two Multi-Wire Drift Chambers (MWDC)[1]. The resultant level scheme from this study is shown in Figure 3.6. The results show a high level density in ^{22}Mg, however no unique spin or parity state assignments could be made, nor their respective widths (Γ_p and Γ_α) determined. The resonance parameters shown in Figure 3.6 have been inferred from the well-known mirror ^{22}Ne.

Figure 3.6 shows the level structure of the compound nucleus ^{22}Mg. As can be seen clearly from 3.6 there is a great deal of uncertainty regarding the properties of the states in ^{22}Mg especially in the high density region covered by the experiment E_x $\sim$10 MeV. The ^{18}Ne+α will only populate states in ^{22}Mg with natural parity. As the states populated will be of natural parity coupled with the high level density, interference effects are a likely phenomenon.

As a rule of thumb, if level densities exceed $\gg 10$ per MeV then a statistical-model treatment of calculating the cross section, such as a Hauser-Feshbach

[1] Directional gas ionisation detector.

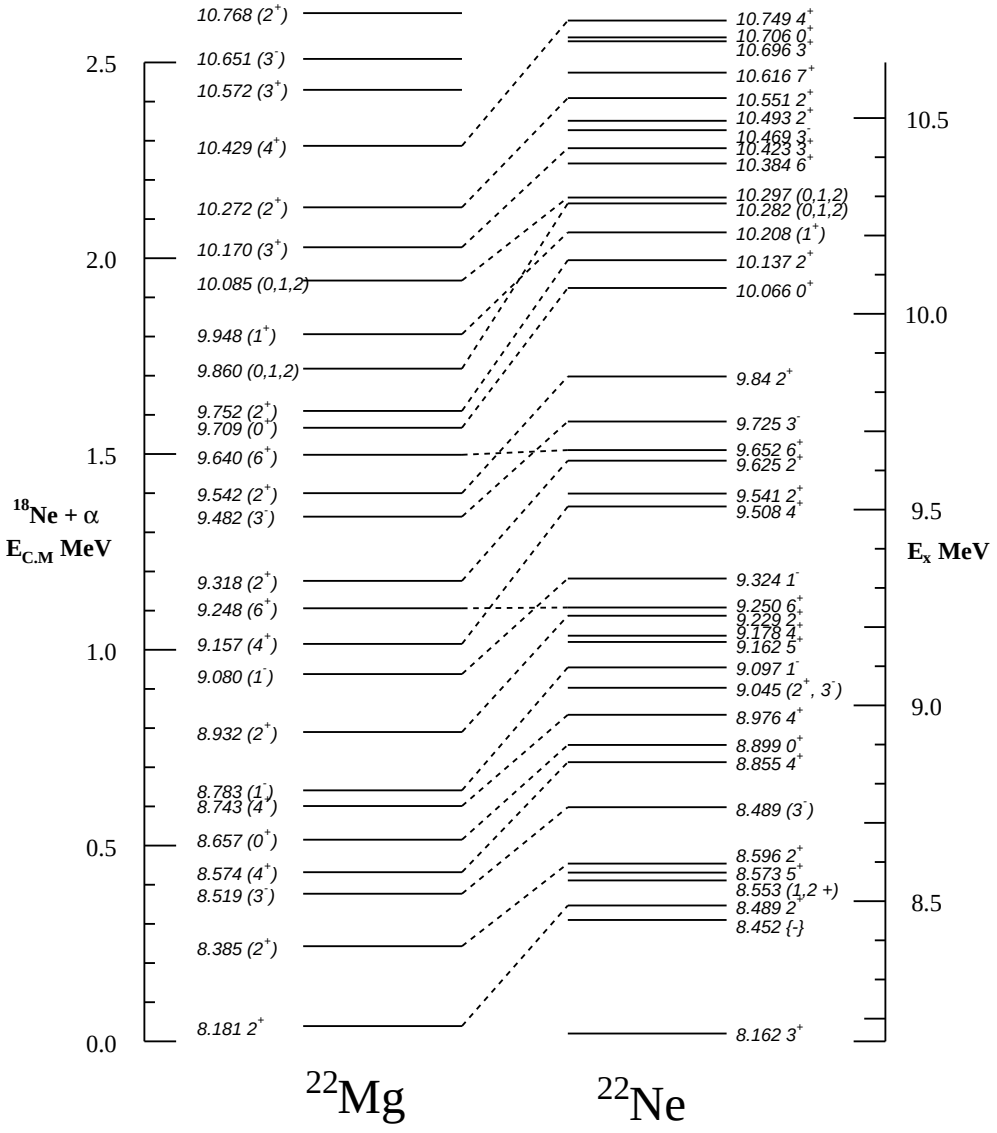

Figure 3.6: *Level schemes for ^{22}Mg and ^{22}Ne. Values taken from [44] and references therein.*

(Section 2.4) calculation, may be employed. Even with only natural parity states being populated the levels are sufficiently dense to warrant a statistical approach.

Chapter 4

Methodology and Experimental Setup

Although the two experiments undertaken during the course of this work vary quite dramatically in reaction type and experimental technique, they share many similarities in experimental setup.

In brief, both experiments make use of a radioactive ion beam from the Cyclotron Research Centre, Louvain-la-Neuve, Belgium. In both cases the beam is incident on a gaseous ^{4}He target inducing nuclear reactions. The reaction products are then detected in a series of segmented silicon detectors.

4.1 CRC Louvain-la-Neuve

The Cyclotron Research Centre (CRC) Louvain-la-Neuve, Belgium, houses the radioactive ion beam facility that was used for both experiments. The Radioactive Ion Beam Project at Louvain-la-Neuve [46] began in 1987 as a collaboration between three Belgian universities, the Université Catholique de Louvain (UCL), the Univerisité Libre de Bruxelles (ULB) and the Katholieke Universiteit Leuven (KUL) and in 1987 accelerated their first beam of ^{13}N. Figure 4.1 shows the layout of the facility.

4.1.1 Radioactive Beam Production

The production of Radioactive Ion Beams (RIB) at the CRC facility makes use of the ISOL (Isotope Separation On-Line) technique. This method requires the use of a high-intensity primary beam of light particles (generally protons)

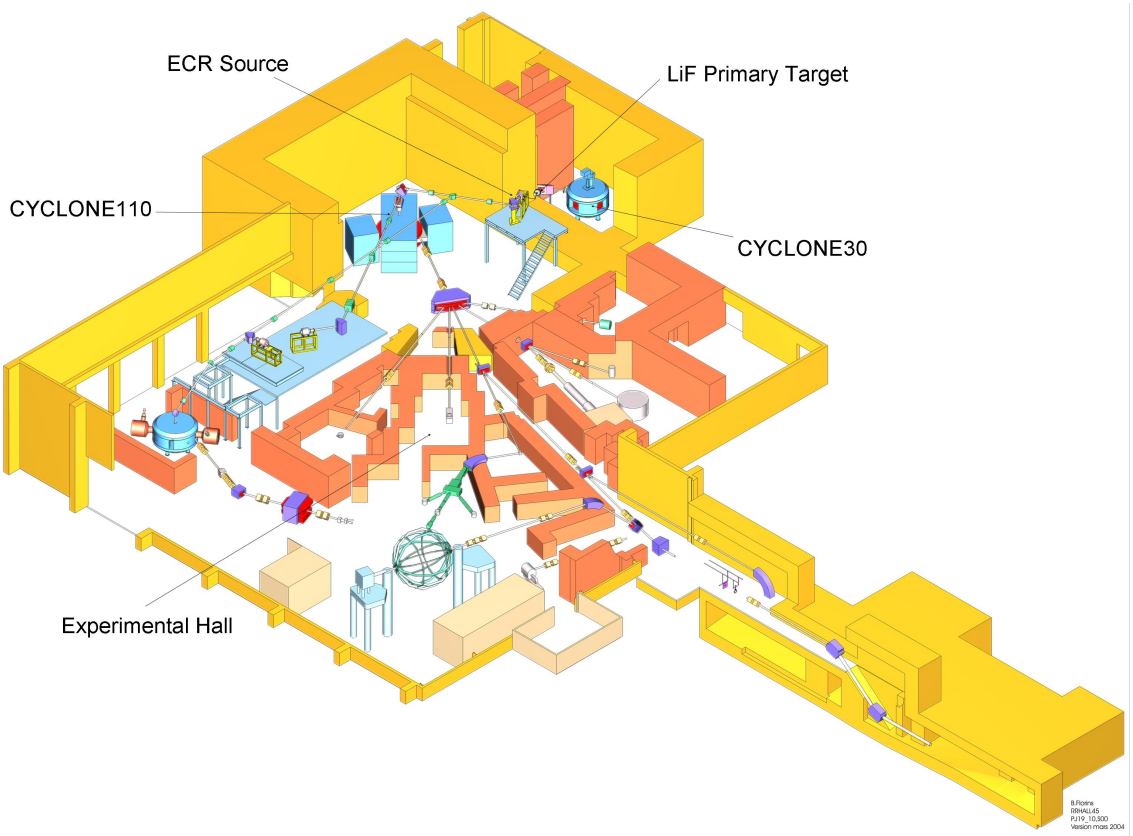

Figure 4.1: *Floor Plan of Experimental Hall, CRC Louvain-la-Neuve [46]*

bombarding a thick, hot target. The products of this initial set of reactions are allowed to diffuse from the target, ionised to a required charge state, and then post-accelerated.

The CRC pioneered the approach of using a cyclotron as a post accelerator as opposed to the more traditional technique of acceleration from a high voltage platform.

4.1.1.1 Primary Beam

A primary proton beam from CYCLONE30 (Figure 4.1), a low energy (30 MeV), high intensity (300μA) proton cyclotron, bombards a lithium fluoride (LiF[1] primary target, Figure 4.2). The target heating to aid fast extraction is provided solely by the beam's power, 9 kW for 300μA, with the beam spot scanning the target (50 mm diameter) using a 50 Hz wobbling magnet. The LiF powder target used will become molten at primary beam intensities of $\sim$100 μA.

The resultant reactions which produce high intensity RIBs are:

$$^{19}\mathrm{F(p,n)}^{19}\mathrm{Ne}\ (t_{1/2} = 17\mathrm{s})$$
$$^{19}\mathrm{F(p,2n)}^{18}\mathrm{Ne}\ (t_{1/2} = 1.7\mathrm{s})$$
$$^{19}\mathrm{F(p,}\alpha\mathrm{n)}^{15}\mathrm{O}\ (t_{1/2} = 122\mathrm{s})$$
$$^{7}\mathrm{Li(p,2p)}^{6}\mathrm{He}\ (t_{1/2} = 0.8\mathrm{s})$$

4.1.1.2 Target Chemistry

The chemical properties of the primary reaction products may hinder their extraction from the target and therefore the intensity of the RIB. This is the case with chemically reactive ^{15}O ions. The original target holder which contained the LiF powder was a hollow graphite cylinder of 45 mm diameter and 17 mm depth. This target holder resulted in a slow and inefficient extraction of ^{15}O. The primary reaction products are transported as molecular flow with the ^{15}O diffusing from the target in the form of C^{15}O or C^{15}O$_2$, the carbon from reactions with the target holder. The LiF powder was mixed with a carbon powder to aid extraction. This did, indeed, result in a faster extraction but the efficiency was still low.

[1]The CRC facility can also use BN, NaCl, ^{13}C and $H_2^{18}O$ targets to produce a range of other RIBs. However for both experiments covered in this thesis a LiF target was used.

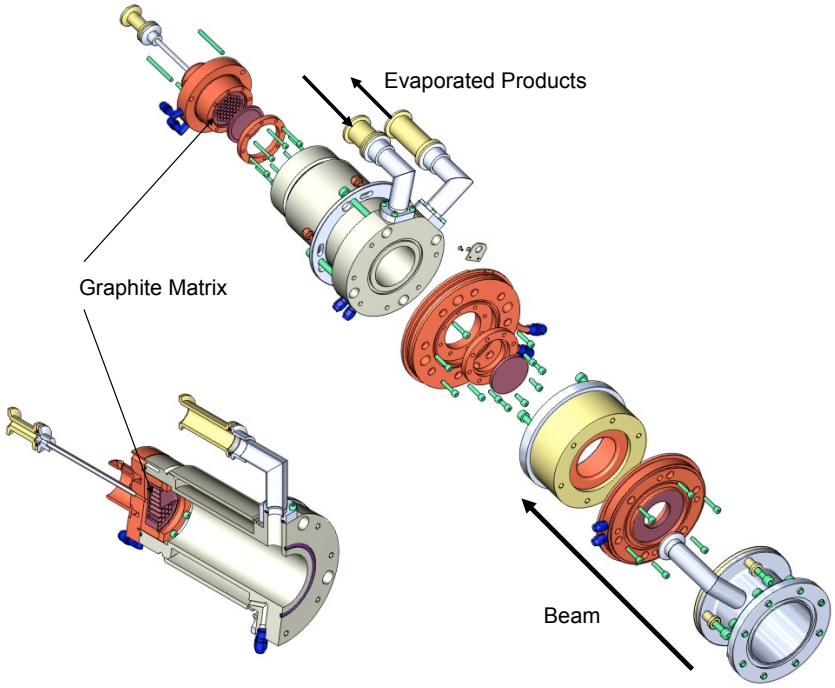

Figure 4.2: *An illustration of the target used at Louvain-la-Neuve. The top left of the expanded figure shows the graphite matrix, the holes of which house the lithium fluoride powder [46].*

The final design of the primary target can be seen in Figure 4.2. A graphite matrix target holder of diameter 50 mm, depth 17 mm, with 48 holes of 5 mm diameter was used as this resulted in a much larger surface area of carbon with respect to the LiF. This final design resulted in an efficiency of 12%[47] with the molecular extraction mode as $C^{15}O$ as opposed to $C^{15}O_2$.

4.1.1.3 Electron Cyclotron Resonance

The reaction products diffuse from the primary target and are transported to an Electron Cyclotron Resonance (ECR) source for ionisation.

An ECR ion source makes use of the ECR phenomenon to heat a plasma. An electron in a static magnetic field will move in a circle due to the Lorentz force. The frequency at which the electrons 'gyrate' is the cyclotron frequency and is dependent on the static magnetic field strength. If microwaves are injected into the ECR ion source volume at this same frequency, in this case 6 GHz [48], the electrons will be resonantly excited.

The energetic free electrons subsequently collide with the low pressure gas atoms from CYCLONE30 ionising them. A low energy (10×q keV) beam of ionised atoms is extracted from the ECR and transported for post-acceleration.

4.1.1.4 Post-Acceleration

The ionised atoms are subsequently sent to CYCLONE110, (Figure 4.1), which, allows for the separation and post-acceleration of the desired ion species. The injected ions from the ECR source will have intense abundances of stable ions with very similar mass/charge ratios, e.g.^{15}O and ^{15}N.

To achieve a high purity RIB the cyclotron is tuned as a radio-frequency mass spectrometer. In an isochronous field the mass resolving power R[49]

$$R = \frac{\frac{q}{m}}{\delta(\frac{q}{m})} \tag{4.1}$$

is given by:

$$R = 2p \times H \times \frac{N_0}{Sin(\Phi_0)} \tag{4.2}$$

where H= Harmonic Number[1], N_0= Number of turns required for the acceleration of particles mass m at charge q to the required energy and Φ_0 = Initial

[1]Number detailing when the particle is in phase with the voltage

Phase. The resolution of the cyclotron is proportional to N_0 and will increase if the dee voltage is decreased.

The accelerated beam is then transported to the experimental hall and then chamber, steered by a series of electromagnets (Figure 4.1). The beam was tuned and centred on the target using scintillators which were monitored by a CCTV camera. The first scintillator was located in the beam pipe before the experimental chamber. The second scintillator was located at the target position, this can be seen in Figure 4.5.

4.2 Experiments with Radioactive Beams

The reactions that take place in explosive stellar scenarios involve unstable nuclei and as such are difficult to study within a laboratory. As a result these reactions are studied in inverse kinematics with radioactive beams. The production and acceleration of these beams (Section 4.1.1) is by no means trivial. The major problem with using RIBs is the intensity of the beams, as the astrophysical reactions studied tend to have low cross-sections (typically millibarns) high beam intensities ($\gg 10^8$ pps)are needed to study them.

4.2.1 Elastic Scattering

Another limitation in using cyclotron post accelerated RIBs is the difficulty in altering the beam energy[1] in small, discrete energy steps in a short period of time, such as in more traditional accelerators, e.g. Van de Graaffs [50] and Cockcroft-Walton machines. This makes the measurement of excitation functions more difficult. To overcome this problem, novel techniques for studying elastic scattering experiments over large energy ranges were pioneered at the CRC Louvain-la-Neuve [51].

The elastic scattering of protons in these early experiments used thick polyethylene targets which slow down the beam thereby yielding various interaction energies through the target, recreating the series of energy steps previously employed with Van de Graafs in normal kinematics.

The ^{15}O(α,α)^{15}O experiment consisted of two stages both of which exploited the thick target technique. The first stage used a stable ^{15}N beam incident on

[1] A particular problem at the CRC, Louvain-la-Neuve.

a helium target to examine the ^{15}N(α,α) elastic reaction, thus probing the well known states of the ^{19}Ne isospin mirror nucleus ^{19}F (Figure 3.1). This was used to validate the technique being used to examine the states in ^{19}Ne, (the second stage), using the same technique but a radioactive ^{15}O beam.

4.2.2 Direct Reactions

As opposed to the thick target employed in the ^{15}O(α,α)^{15}O experiment, the ^{18}Ne(α,p)^{21}Na reaction has been studied directly using a relatively thin target. This allows for a minimal beam energy loss across the target and thus for a discrete energy point to be investigated. In this case, two discrete energies were investigated, at $E_{\mathrm{CM}} = 1.7$ and 2.5 MeV [1].

4.3 Setup

4.3.1 Kinematics

Prior to conducting experiments the kinematics of the reaction being studied were examined to best determine the relative positions of the target and detectors. By studying the kinematics of the reaction under investigation and those of possible background reactions the detectors could be positioned such that the yield from the reaction products of interest could be maximised while those of background reactions minimised. Kinematic considerations such as these are of particular use when the reaction products are to be studied in coincidence. The final position of the detectors and targets are a compromise between geometrical efficiency and the physical constraints of the experimental chamber.

4.3.1.1 ^{15}O(α,α)^{15}O

Due to the nature of elastic reactions detectors are best placed at forward angles to achieve the best experimental resolution. The yield however is much less at $\theta_{lab} = 0°$. A compromise is reached between resolution and yield. This however, brings other factors into consideration, which affect the final position of the detectors. For example, the beam intensity since radiation damage from the beam on a detector at $\theta_{lab} = 0°$ can be significant (beam may be stopped in the

[1] $E_{\mathrm{CM}} = 2.5$ MeV corresponds to a temperature of $\sim 2.4 \times 10^9$ K, well above the temperature region at which this reaction would occur in an astrophysical scenario

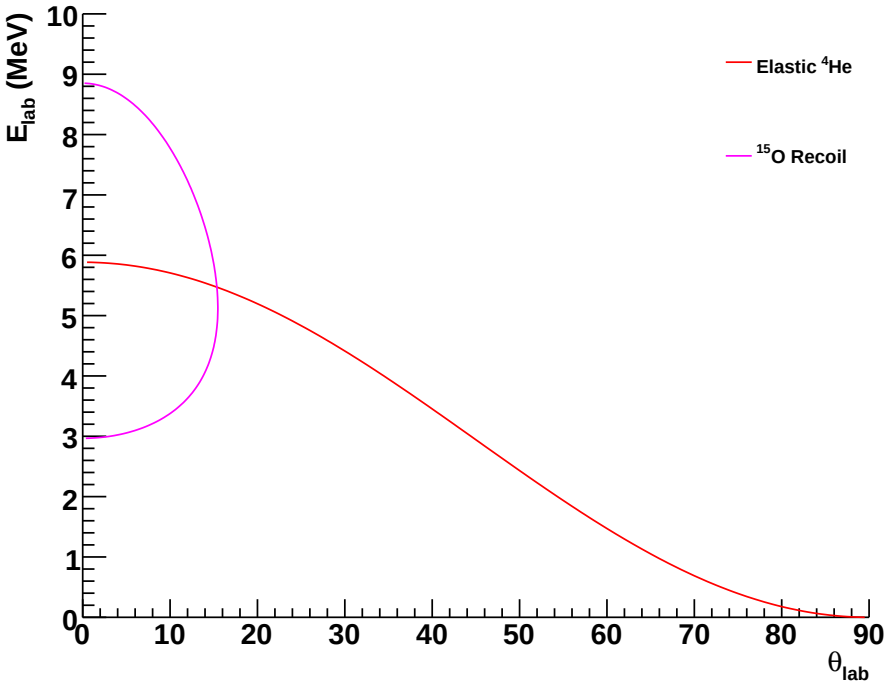

Figure 4.3: *Kinematics of the elastic α-particles and ^{15}O recoils for the $^{15}O(\alpha,\alpha)^{15}O$ reaction. The calculation was performed with a beam energy of E_{Lab} = 20.3 MeV, with no energy losses considered.*

target). A protective shield could be put in front of the $\theta_{lab} = 0°$ detector, but this would increase straggling effects and decrease the experimental resolution.

Kinematics for the ^{15}O(α,α) reaction are shown in Figure 4.3. The ^{15}O(α,α) was not simulated.

4.3.1.2 ^{18}Ne(α,p)^{21}Na

The kinematics of the reaction protons are shown in Figure 4.4, with the angular range of the detector telescope highlighted.

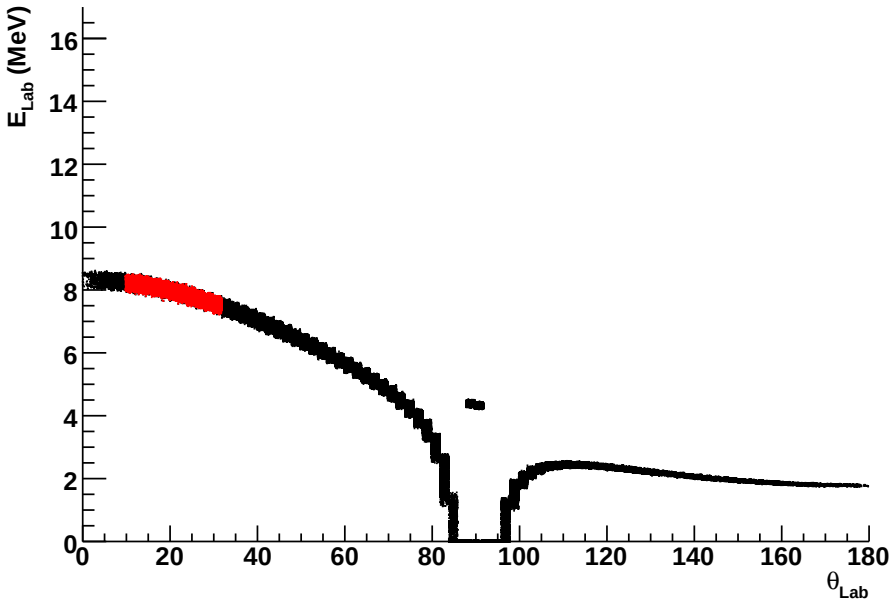

Figure 4.4: *Kinematics of reaction protons from the ^{18}Ne(α,p)^{21}Na reaction. The reaction is assumed to be an $l = 0$ transition with the ^{21}Na recoil being left in the ground state. The beam energy used in the simulation was E_{Lab} = 21.5 MeV, with the area highlighted in red showing the angular range subtended by the detector telescope.*

The main aim of the Monte Carlo simulation was to calculate the geometric efficiency of the detector system for use in calculating the final cross-section.

Through modelling of the beam, target and energy losses, straggling effects through the Mylar entrance window, the ^{4}He gas and the aluminium exit window, a comparison with the experimental data could be made.

The simulation also allowed for examination of the expected proton energies as a result of the ^{21}Na recoil being left in an excited state.

4.3.2 ^{4}He Gas Target

The experiments, both in inverse kinematics, involve a radioactive beam being incident on a gaseous ^{4}He target. The physical characteristics of the target varied between the two experiments. This is due to the different experimental techniques being employed demanding either a thin (^{18}Ne(α,p)^{21}Na) or thick (^{15}O(α,α)^{15}O) target. The same considerations, however, had to be taken into account for the design and construction of both.

The final design of the gas cell was a compromise taking many factors into account. Helium has a diffusion rate three times that of air through solids. This makes it the gas of choice for leak detection, but makes it difficult to contain. It was therefore necessary to construct a cell that was sturdy enough to have a manageable leak rate (design goal of 10% loss of pressure over 48 hours) and yet allow for the radioactive beam to interact with the gas at the desired energy. It was also necessary for the reaction products of interest to have minimal energy loss in the gas cell exit window.

The main body of the cell was made of aluminium with openings at either end for the entrance of the beam and the exit of reaction products. The size of these entrance and exit windows was another consideration. As the cell would be at pressure, it was necessary to keep the window diameters as small as possible[1] while trying to fulfil the target's aims. The entrance window was constrained by the beam spot size available. At Louvain-la-Neuve this is typically in the region of ϕ ~8 mm and thus the window diameter was fixed at 15 mm. The conditions determining the geometry of the exit window depended on the angular range subtended by the detectors, which in turn was a compromise between the physical constraints of the experimental chamber and those of the kinematics of the experiment.

The final matter that had to be taken into account when designing the targets was the choice of material with which to construct the entrance and exit

[1] The larger the window, the greater the stress on the edges of the window (assuming a circular window). This is due to the larger force the window feels as a whole which must be supported by the relatively smaller area of the connection between window and pressure vessel[53]

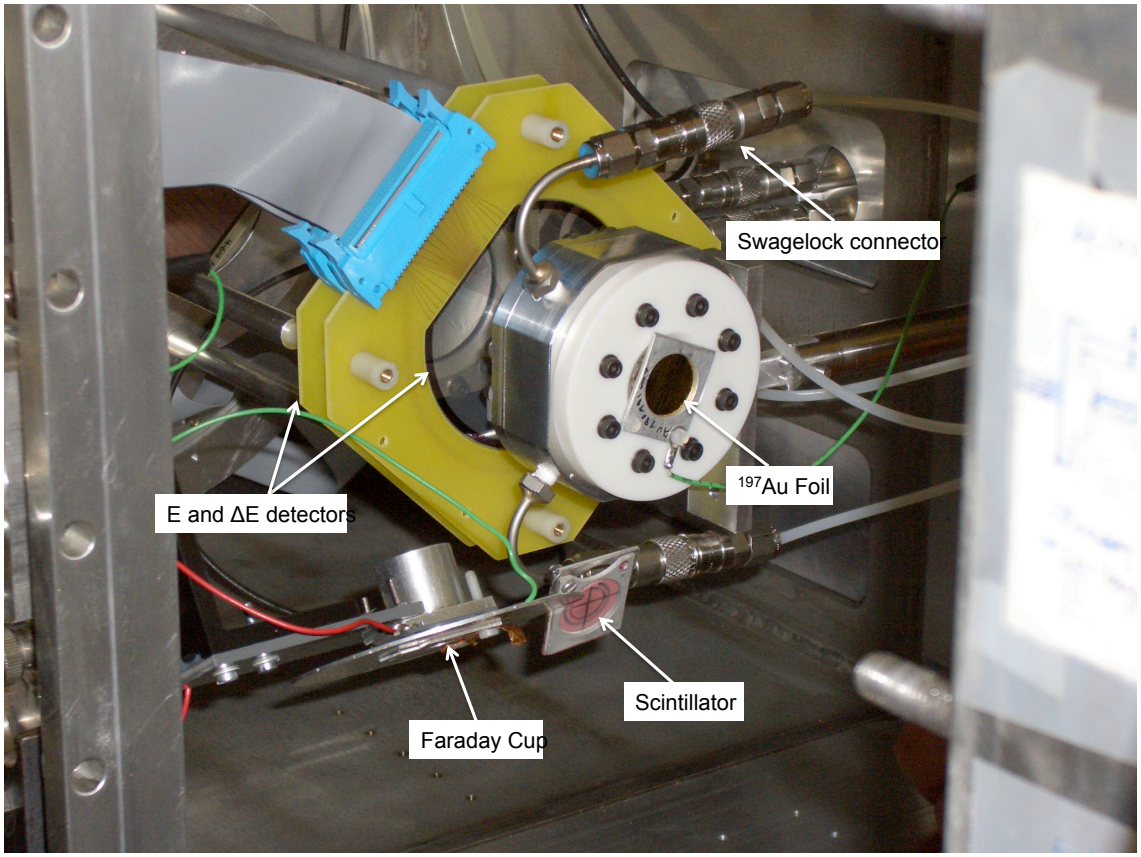

Figure 4.5: *Photograph of gas target used in the* $^{18}Ne(\alpha,p)$ *experiment. Also shown are the scintillator (bottom of the picture - pink) used for beam tuning, the gold foil used for normalisation (mounted directly in front of the entrance window), the gas Swagelok[52] connectors (quick release, 'plug-n-play 'connectors used in the gas system) and the* $\Delta E - E$ *detector telescope system.*

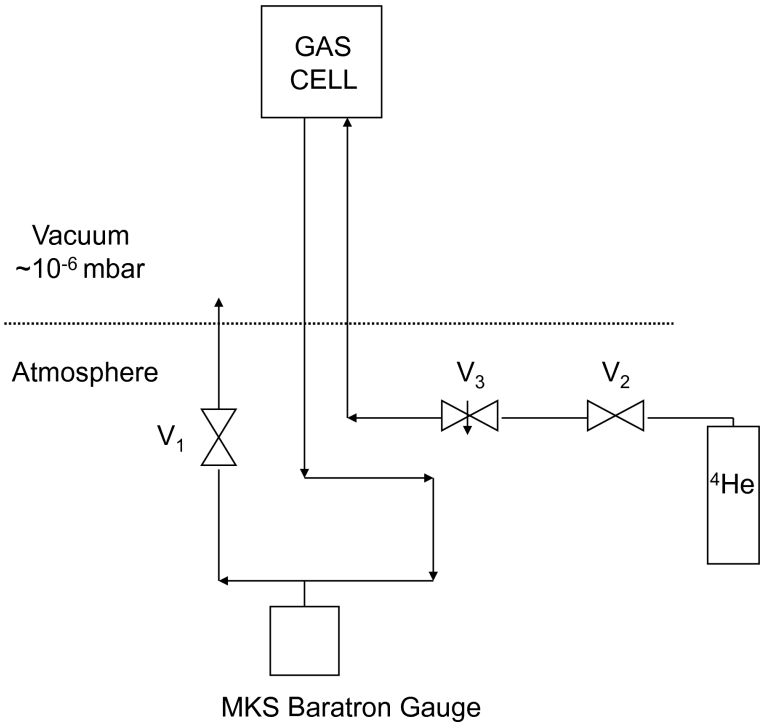

Figure 4.6: *Schematic of Gas Cell Setup. When bringing the chamber down to vacuum the bypass valve (V_1) is open so that the target remains at the same pressure as the chamber. Once at vacuum the bypass valve (V_1) is shut and the cell is filled by opening the valve V_2 and the needle valve V_3. Once at the required pressure these are both closed and the target is ready for beam.*

windows. Two factors were important here. Firstly, the material had to be thick enough to withstand the pressures that it would be subjected to, while at the same time it had to be thin enough to allow the beam to enter the cell and the reaction products to exit with minimal straggling effects. The second condition was that of possible background reactions resulting from (primarily) the beam's interaction with the entrance window. The possible two-body interactions resulting from each material were examined. This information allowed the choice of material for which the background reactions would least impact on the energy region under investigation.

Finally, the pressure in the gas cell was monitored using an MKS Baratron [54] gauge connected to a Baratron gauge control.

4.3.3 LEDA, S2 and W1 Type Segmented Silicon Detectors

Segmented silicon detectors (Appendix A) were used in both experiments. The LEDA (MSL type YY1[55]) detector arrays, manufactured by Micron Semiconductor Ltd. [56] are single sided, p^+n junction type, reversed-biased silicon strip detectors, arranged in a radially symmetric configuration of sixteen annular strips in eight azimuthal segments [55]. Figure 4.7 shows four segments of the LEDA array.

The type S2 detector (Figure 4.8(a)), also manufactured by Micron Semiconductor Ltd [56], is a Double Sided Silicon Strip Detector (DSSSD) with 48 annular p^+n junction strips and 16 azimuthal n^+n ohmic segments, the dimensions of which are given in table 4.1.

The W1 (4.8(b)) type detector is a DSSSD with 16 p^+n junction and 16 n^+n ohmic strips arranged in an orthogonal formation.

4.3.4 Data Acquisition

The experimental data acquisition system is shown schematically in figure 4.9. Signals from a detector were amplified by a charge-sensitive preamplifier (RAL108). For LEDA segments these were placed on the outside of the chamber and were connected by 34-way ribbon cables (16 channels) via a vacuum feedthrough. The ^{18}Ne(α,p) experiment made use of the type S2 detector, the preamplifiers for which were located within the experimental chamber. As a result of this they

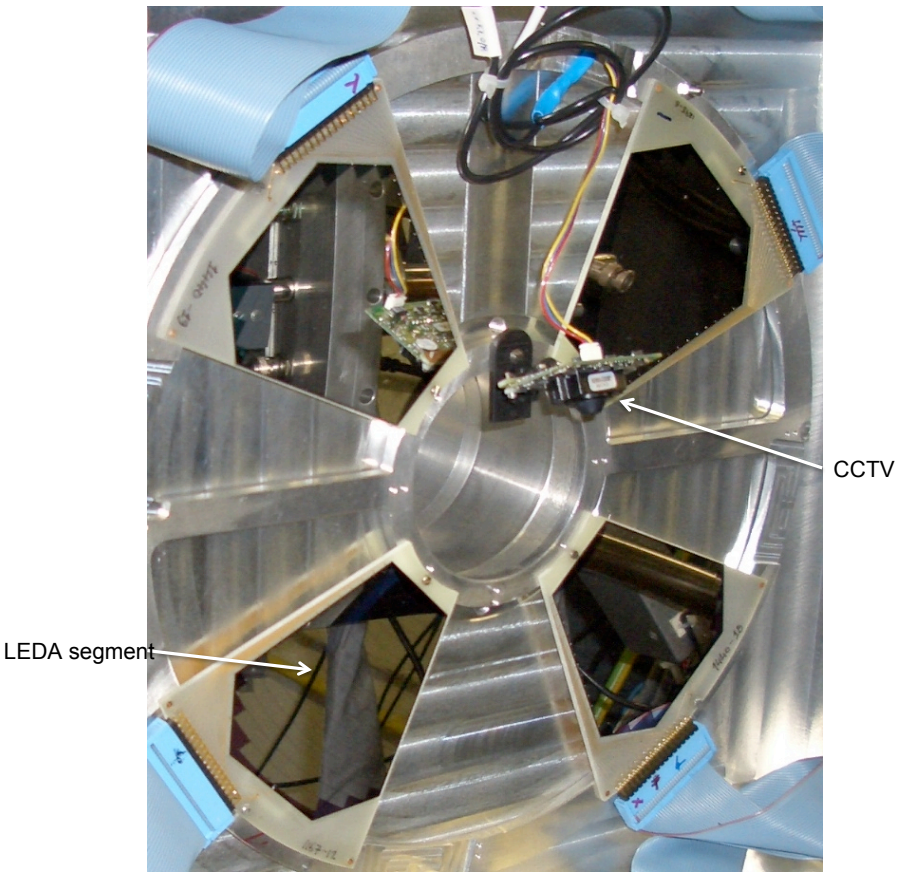

Figure 4.7: *Four segments of LEDA used for detecting the back scattered beam particles from the* ^{197}*Au foil. Also shown is miniature CCTV camera which was used for focusing the beam on the scintillator during beam tuning.*

Table 4.1: Characteristics of an S2 type detector

Design	**S2**
Technology	4”
Active Area	25.37 cm^2
Active Outer Diameter	70 mm
Active Inner Diameter	23 mm
Annular Hole Diameter	20 mm
N$^{\underline{O}}$ of Front Contact Pads	48
N$^{\underline{O}}$ of Back Contact Pads	16
Contact Pitch	0.490 mm
Contact Width	0.390 mm

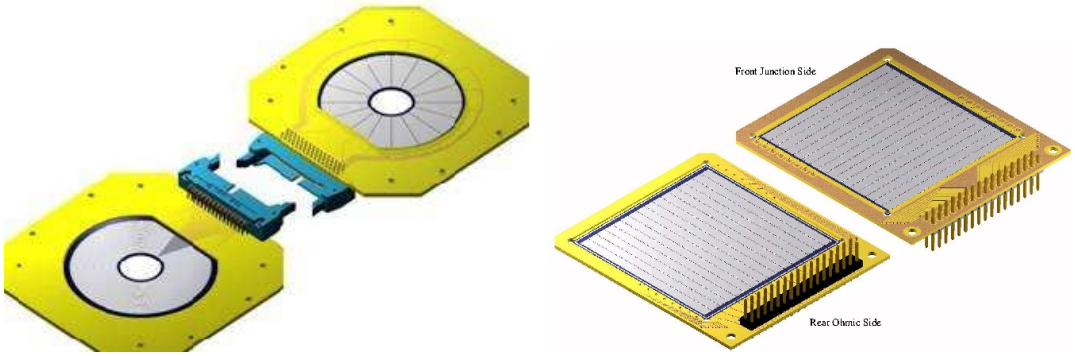

(a) S2 Type Detector (b) W1 Type Detector

Figure 4.8: *The S2 and W1 type detectors. The lower portion of 4.8(a) shows the p^+n junction side for the S2 detector (48 radial strips). The top segment shows the n^+n ohmic side of the type S2 detector (16 annular segments) [56].*

could not be air-cooled during the experimental run, and thus, were mounted on a cooling board through which circulated ethanol at a temperature of -10°C. This resulted in a preamplifier working with a stable temperature between T∼20° - 50°C.

The preamplifier output was sent to a distribution board where the 16 channels were split into two sets of 8 channels, each channel corresponding to a detector element.

The output from the distribution board was sent to an 8 channel shaping amplifier (RAL109) which converted the signal into both analogue and logic outputs. For both the experiments the gain of the shaping amplifier module was set with a 22Ω resistor and 100Ω terminator , corresponding to ∼22 MeV = 10V full scale range.

The analogue output from each amplifier was sent to an ADC (32 channel Silena 9418/6V VME ADC) and the logic signal was daisy chained to both a logic module (4.3.4.1), and a TDC (CAEN V1190 TDCs). The TDCs were in common stop mode, started by the output from the discriminators and stopped by the HF signal from the cyclotron. This allows for the time-of-flight of the particles with respect to the cyclotron to be measured for particle identification.

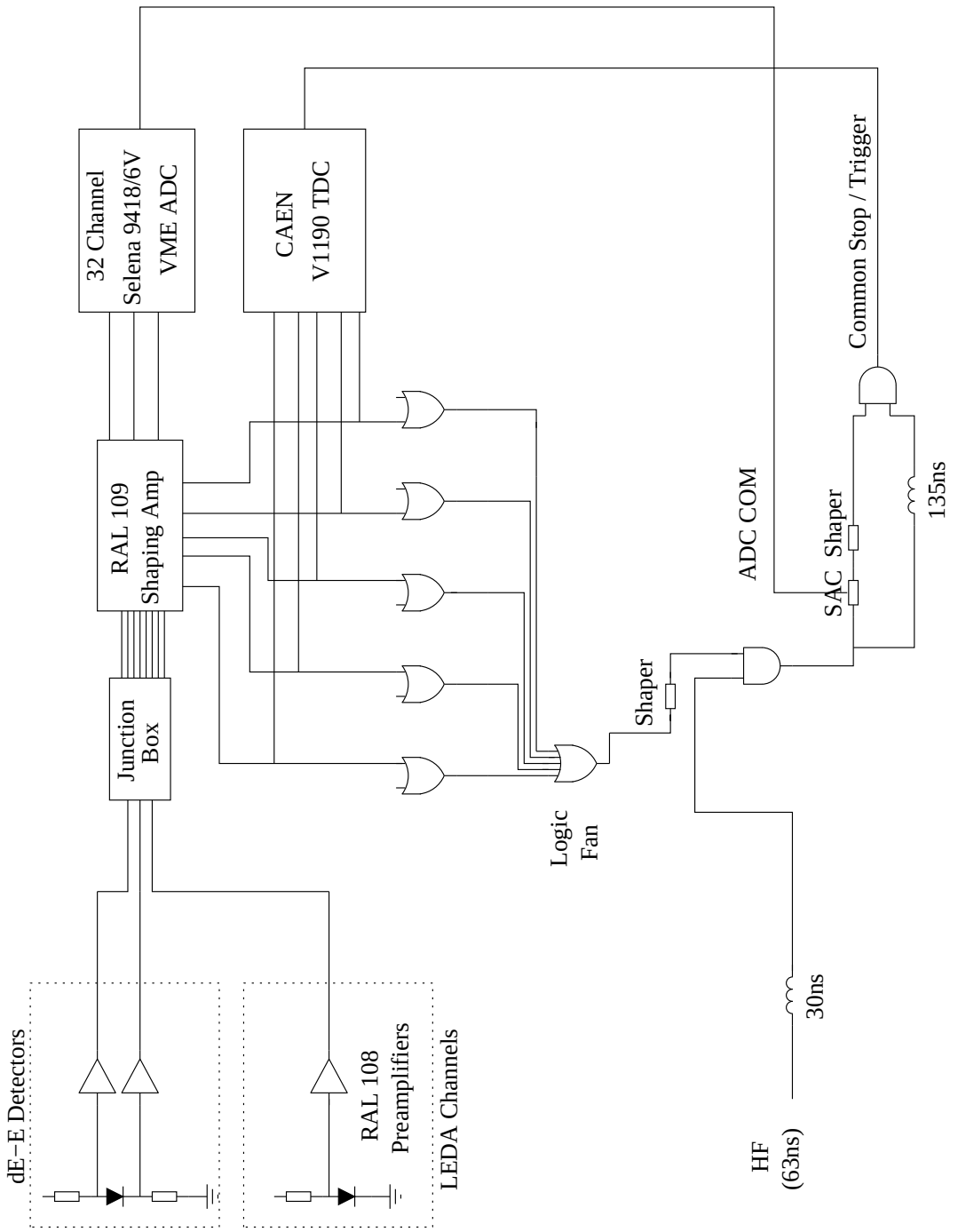

Figure 4.9: *Schematic of data acquisition electronics used in the $^{18}Ne(\alpha,p)$ reaction. The same setup was used for the $^{15}O(\alpha,\alpha)$ experiment.*

4.3.4.1 Trigger

The trigger logic (Figure 4.10) for the acquisition system was generated by taking the total OR of all the detectors in coincidence with the HF signal[1] from the cyclotron.

The logic signal from the leading edge discriminator passed first to the Edinburgh-built CAMAC 48-input logic module. This module had 3×16 channels of inputs with 4 possible outputs. The first 3 outputs gave the OR of each group of 16 channels, the fourth gave the total OR of all 48 channels in the module.

The total OR from the module (output 4) passed to a logic fan in/out module (LeCroy 429A) where a total OR of all the outputs from the logic modules was produced.

Some logic signals were then embedded within the data as scalers. Typically these include the number of triggers, trigger accepted and a clock. These scalers could also then be used to monitor in real time the trigger rate and livetime during the experiment.

This total OR in coincidence with the periodic HF signal was the primary experimental trigger. The trigger signal passed to the SAC (Silena ADC Control) module [57]. The SAC has a logic state engine that is run on a 40 MHz clock. This means that the outputs are not synchronous with the inputs. This 'jitter' is shown schematically in Figure 4.10 as the dashed lines. If the ADCs were not busy the SAC module passed the trigger to the ADCs to initiate conversion. The SAC module then produced a 'Monitor 2' output indicating an accepted trigger. This accepted trigger was shaped and put in coincidence with the delayed trigger. This became the 'common stop' for the TDCs[2].

This signal was also read out as a scaler. The ratio between total triggers and triggers accepted gave the live time of the acquisition system.

The ADCs and TDCs were read out by VME CPU using the MIDAS data acquisition software. The DAQ built events and appends them to data blocks which were sent to the tape server for storage and online analysis.

[1] The time period varies with beam energy, in the region ∼60-90 ns

[2] The TDC is not controlled by the SAC module directly. The TDC must convert when, and only when, the ADC does so that the ADC and TDC data remain synchronised.

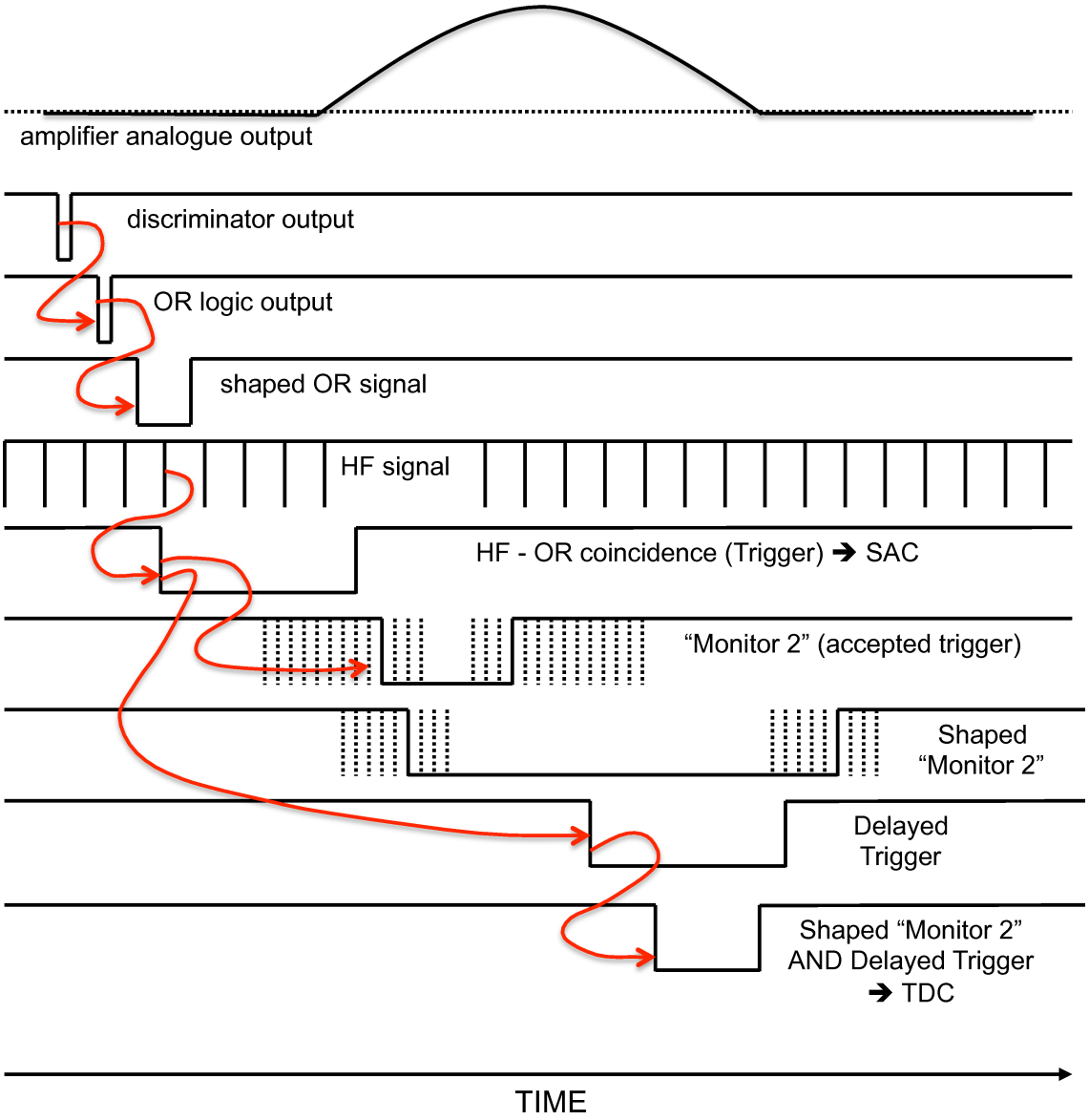

Figure 4.10: *Schematic diagram of timing and trigger logic*

4.4 Experimental Setup

4.4.1 ^{15}O(α,α) Setup

The beam, ^{15}O or ^{15}N, was incident upon a ^{4}He gas target cell designed specifically for the experiment. The 6 cm long, aluminium gas cell had an aluminium metallised Mylar entrance window (ϕ = 15 mm, thickness = 3.5 μm), and an aluminium metallised Mylar exit window (ϕ = 48.5 mm, thickness = 6 μm), which held the 99.999% pure ^{4}He at $\sim$ 300 mbar ($\sim 4.45 \times 10^{19}$ particles cm^{-2} at 293 K). The ^{15}O beam was stopped in the exit window. Mounted directly in front of the entrance window was a $\sim$ 180 μg/cm^2 ^{197}Au foil used for beam normalisation. Upstream from the centre of the target at a distance (84.1 $\pm$ 1) mm, four sectors of LEDA were used for detection of the back-scattered ^{15}N and ^{15}O.

The downstream detector system consisted of 7 sectors of LEDA (thickness 300 μm) at a distance of (575 $\pm$ 1) mm from the centre of the target, with a zero degree detector (type W1) 20 mm $\pm$ 1 mm behind this LEDA array. The LEDA array covered an angular range between θ_{lab} $\sim$5° - 12°.

Using the 110 MeV cyclotron the ^{15}O was accelerated to the required energy, in this case E_{Lab} = 20.3 MeV. Following calculated energy losses [58] through ^{197}Au foil (normalisation) and the Mylar entrance window of the gas target cell these beam energies yielded an interaction energy range of E_{CM} = 2.54-3.17 MeV. Data were recorded for a full gas cell and an empty gas cell, the time taken for each was $\sim$52 hrs and $\sim$5 hrs respectively. The beam had a typical time-averaged intensity of 9.28×10^6 pps for both foreground and background runs. The beam spot size was 0.8 cm ϕ and the energy resolution of the beam was $\sim$200 keV FWHM.

To validate the experimental method and data analysis, the level structure of the well known mirror, ^{19}F, was studied using the same target and detector setup with a stable ^{15}N beam. The ^{15}N beam, also produced at the CRC, had a time-averaged intensity of 2.37×10^8 pps with a beam energy of 18.9 MeV and an intensity of 3.01×10^8 pps for a beam energy of 20.3 MeV for both foreground and background runs. The total time taken for data runs and background runs were $\sim$5 hrs and $\sim$6 hrs respectively.

The excitation energy range covered in ^{19}F, E_{CM} = 2.6 - 3.4 MeV, overlaps with that studied in ^{19}Ne and thus allows for direct comparison of the mirror nuclei ^{19}F and ^{19}Ne.

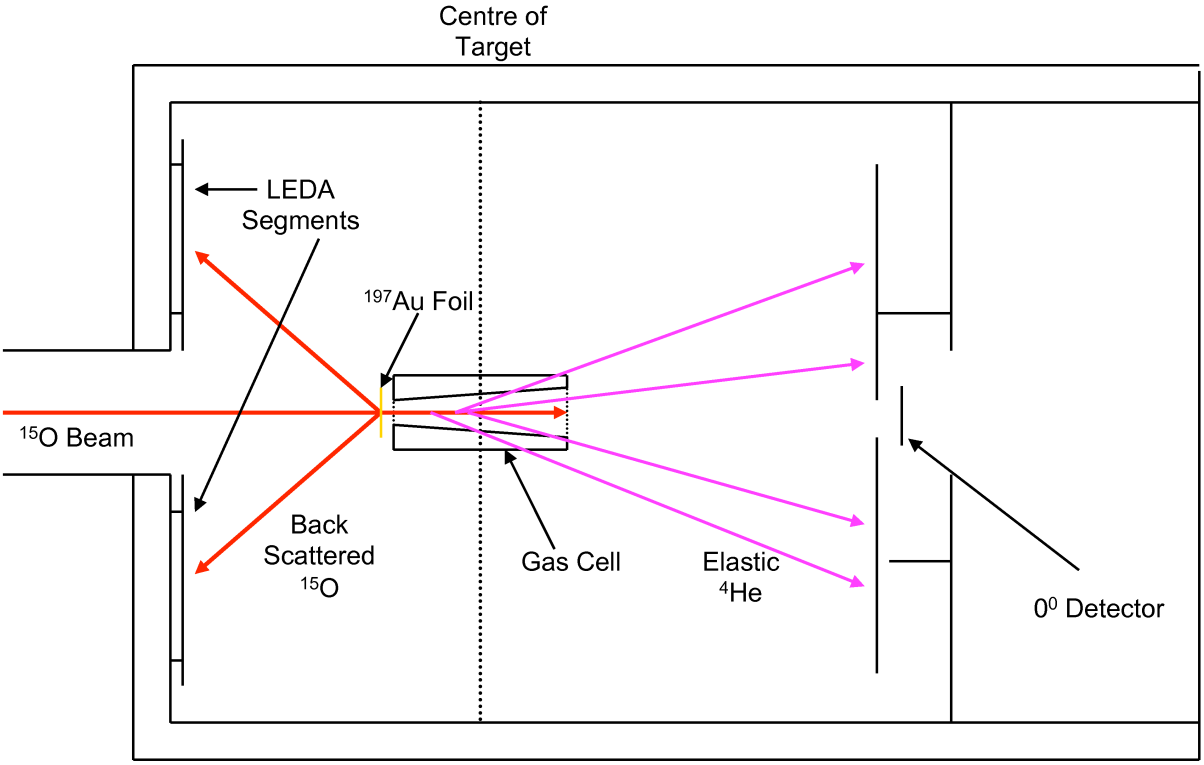

Figure 4.11: *Schematic of the $^{15}O(\alpha,\alpha)$ experiment chamber setup. It must be noted that the diagram is not to scale.*

4.4.2 ^{18}Ne(α,p) Setup

The radioactive beam species in this experiment was ^{18}Ne. The primary target reaction products were extracted and sent to the ECR source where the ^{18}Ne was ionised into the 3^+ state. Using Cyclone110 the ^{18}Ne was post-accelerated to the required energies of, E_{Lab} = 17.5 MeV and 21.5 MeV. Following calculated energy losses (SRIM2003 [58]) through the ^{197}Au foil (normalisation) and the Mylar entrance window of the gas target cell these beam energies yielded interaction energies of E_{CM} = 1.7 MeV and 2.5 MeV respectively in the centre of the ^{4}He gas target. At each interaction energy data were recorded for a full gas cell and an empty gas cell, at E_{CM} = 2.5 MeV the time taken for each were ∼75.6 hrs and ∼10.9 hrs respectively and at E_{CM} = 1.7 MeV ∼52.4 hrs and ∼25.4 hrs respectively. The beam, had a typical time-averaged intensity of 4.5 × 10^5 pps at E_{CM} = 2.5 MeV and 1.5 × 10^6 pps at E_{CM} = 1.7 MeV (following a production target change). The beam spot size was 0.8 cm ϕ and the energy resolution of the beam was 200 keV FWHM.

The beam was incident upon a ^{4}He gas target cell designed specifically for the experiment with a thickness $\Delta E_{\mathrm{CM}} \sim$ 220 keV comparable to that used in the time-reverse measurement, $\Delta E_{\mathrm{CM}} \sim$ 140 keV [41].The 2 cm long, aluminium gas cell had an aluminised Mylar entrance window (ϕ = 15 mm, thickness = 3.5 μm), and an aluminium exit window (ϕ = 48.5 mm, thickness = 15 μm), which was held at ∼ 200 mbar (∼ 9.89 × 10^{18} particles cm^{-2}).

Mounted directly in front of the entrance window was a ∼ 180 μg/cm^2 ^{197}Au foil used for beam normalisation. Upstream from the centre of target at a distance of (96 ± 1) mm, four sectors of LEDA [55] were used for detection of the back-scattered ^{18}Ne.

The ΔE detector was 6 cm downstream from the centre of the target, with the E detector being a further 15 mm downstream. Both the ΔE and E detector were annular type S2 DSSSD detectors [56] of thickness 70 μm and 500 μm respectively, with the E detector covering an angular range θ_{lab} ∼10° - 28°.

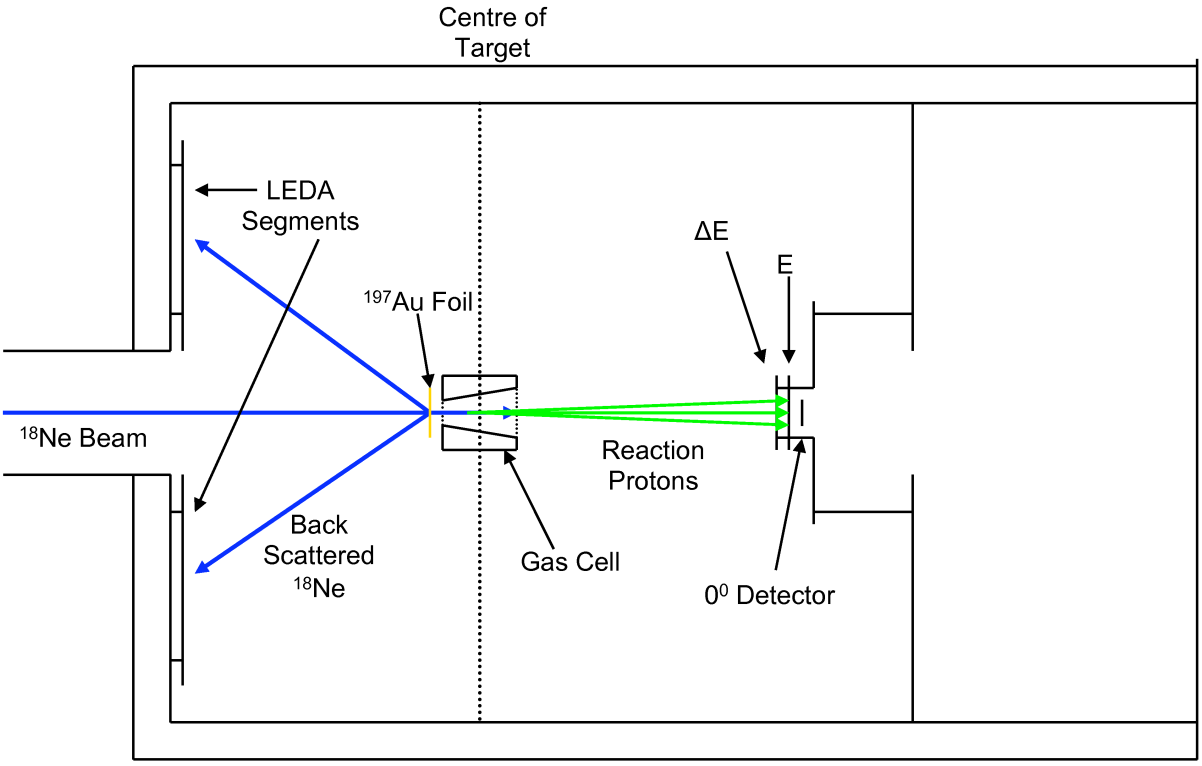

Figure 4.12: *Schematic of $^{18}Ne(\alpha,p)$ Chamber Setup*

Chapter 5

^{15}O(α,α) Data Analysis

This chapter will detail the methods used to convert the raw experimental data for the ^{15}O(α,α) reaction into differential cross-sections. The R-matrix fitting procedure applied to extract resonance energies and widths will also be outlined. Since the same experimental setup was employed to study the ^{15}N(α,α) reaction almost identical analysis methods were used. Relevant differences between the two will be highlighted.

The data analysis procedure can be summarised as follows:

1. Calibrations were applied to convert the raw ADC and TDC values to physical units.

2. α particles detected in the LEDA strips were identified via a Time of Flight method.

3. A correction was applied to the identified α-particle energies to correct for energy lost traversing the target materials and therefore calculate the origin of the interaction.

4. The data were normalised with respect to the beam intensity and differential cross-sections calculated.

5. The data were fitted using the R-matrix method to extract resonance parameters.

These steps will now be described in more detail.

5.1 Calibration of Segmented Silicon Detectors

Each of the strips on the segmented silicon detectors have individual preamplifiers, amplifiers and ADCs and thus each must be calibrated individually. The calibrations were performed at the beginning and end of each experiment to check for any energy drift during the runs. For a linear[1] energy calibration two known parameters are needed, a gain and offset such that

$$\text{Energy(keV)} = \text{gain(keV/channel)} \times (\text{ADC(channel)} + \text{offset(channel)}) \quad (5.1)$$

The first step of the energy calibration was to calculate the offset for each channel via a pulser walkthrough. This was done by varying the pulser signal amplitude in a known ratio into the test input of the preamplifier, resulting in equally-spaced sharp peaks (in this case 9), the positions of which could be used to calculate the offset for each channel.

To calculate the gain for each element a mixed α source (activity 3 kBq) of ^{239}Pu-^{241}Am-^{244}Cm with principal energies 5.15659, 5.48556 and 5.80477 MeV [37] respectively was used. The source was placed at the target position. Statistics were accumulated until three prominent peaks could be identified, typically over a time period of approximately 2 hours, (Figure 5.1). Once the statistics had been accumulated, an offline gain match could be applied to rescale each ADC to give an absolute energy value for each channel. α-particle energy losses through the aluminium and p^+n junction dead layers of the detector are taken into account.

5.2 Particle Identification

With the gains and offsets calculated for each strip (Section 5.1) the experimental data could be sorted and examined. As described in section 4.3.4, each of the individual silicon detectors was instrumented with an ADC and TDC providing information on the energy deposited in the detector and the time of the deposition. The time resolution of the instrumentation was sufficient to differentiate between protons, α-particles and heavy ions through examination of their respective flight times. This method exploits the mass difference between

[1] This is a reasonable assumption as the pulser walkthrough gives a linear correlation between pulser amplitude and channel number, e.g. integral non-linearity < 0.1 %, typically ~ 0.05 %.

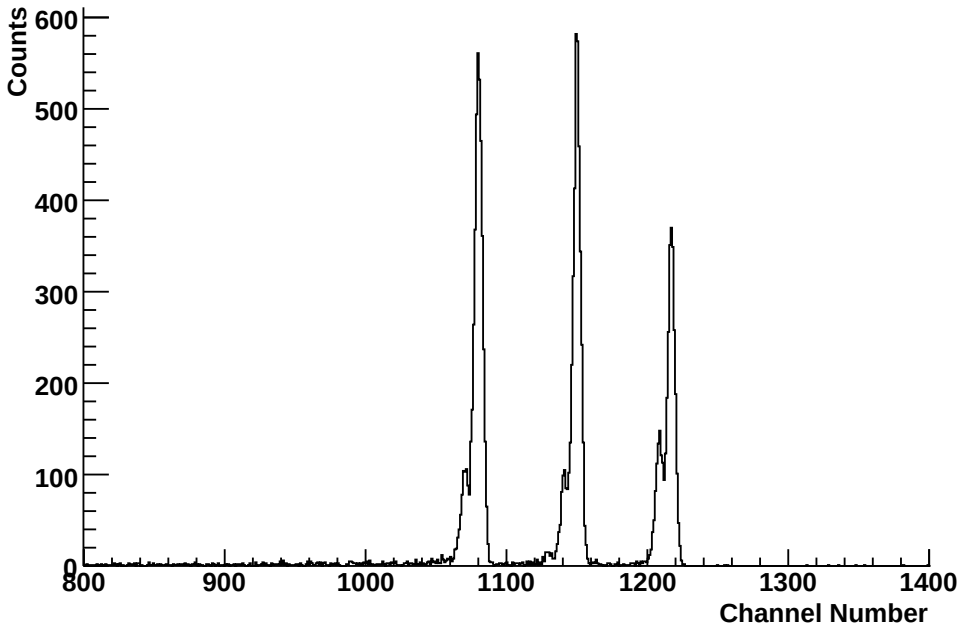

Figure 5.1: *Typical alpha spectrum used for calibration. The peaks shown are* ^{239}Pu-^{241}Am-^{244}Cm *with principal energies 5.16, 5.49 and 5.80 MeV respectively. The FWHM for the* ^{241}Am *peak is* $\sim$*35 keV FWHM.*

different particle species e.g. a 5 MeV α particle will take longer to reach the experimental detectors than a 5 MeV proton. As a result, in plots of Energy vs Time, events are grouped together in bands corresponding to different particle species. Figures 5.2 and 5.3 detail a typical ADC *vs* TDC spectrum for the two reactions ^{15}O(α,α) and ^{15}N(α,α) respectively.

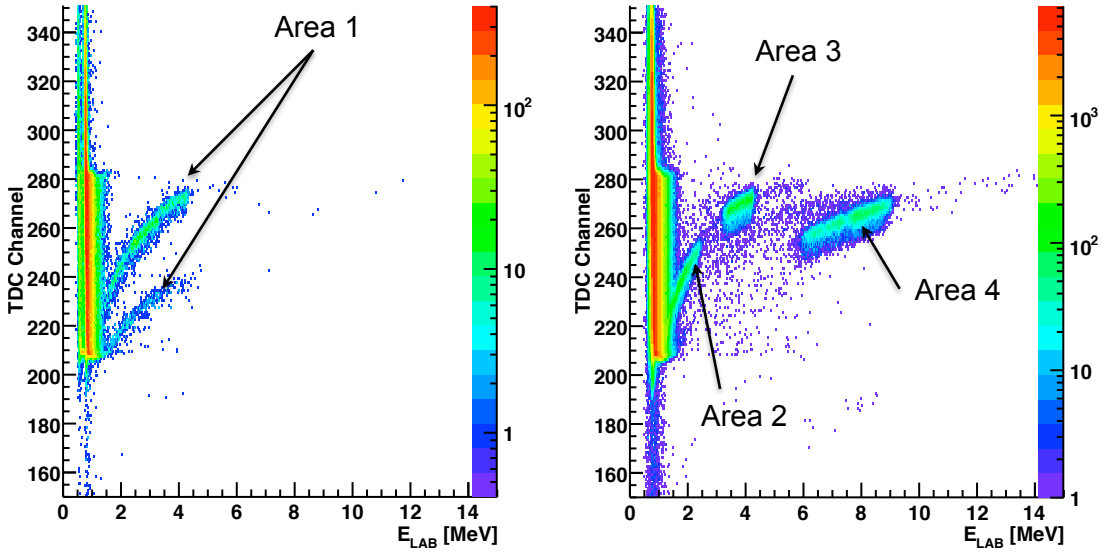

Figure 5.2: *Energy vs raw TDC spectrum for the $^{15}O(\alpha,\alpha)$ reaction. The left hand figure shows a spectrum from an 'empty' gas cell, with the right hand figure showing a 'full ' gas cell. On each plot running along the y-axis are uncorrelated events from the β decay of the beam.*

The spectra show an 'empty' background run and a 'full' gas cell run. The spectra shown are typical examples and taken from one strip of one segment (LEDA sector 2, Strip 0), from which four main areas of interest become apparent, these are detailed in table 5.1. As can be seen the spectra are relatively clean and the particles of interest readily identifiable, especially in the ^{15}O(α,α) data set.

The offset of data as indicated in the 'empty' spectrum of Figure 5.2 is due to a timing change between the background runs and was corrected for within the sorting software. It should be noted that in the 'full' gas cell spectra the gap between the two groupings of elastic protons is an indication of the energy loss of the beam through the ^{4}He target gas.

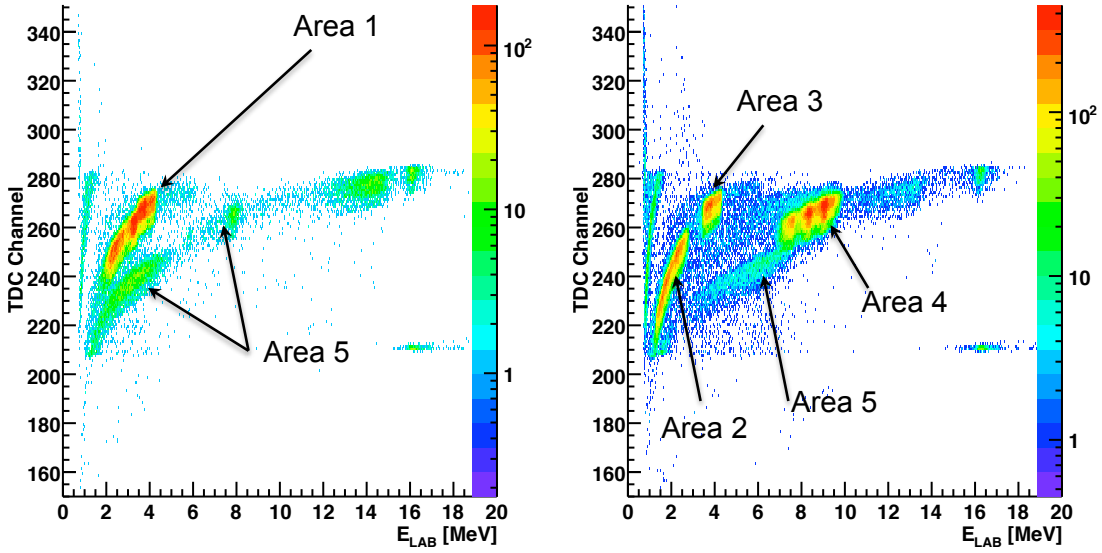

Figure 5.3: *Energy vs raw TDC spectrum for* $^{15}N(\alpha,\alpha)$*. The left hand figure shows a spectrum from an 'empty' gas cell, with the right hand figure showing a 'full ' gas cell. The area labelled* 5*, although its origin remained undetermined, did not impact upon the area of interest (*4*).*

Table 5.1: Identification of areas in ADC *vs* TDC spectrum for $^{15}O(\alpha,\alpha)$ and $^{15}N(\alpha,\alpha)$

Area	**Detected Particle**	**Reaction**	**Target**
1	Proton	$^{15}O(p,p)$ or $^{15}N(p,p)$	Mylar (gas cell windows)
2	Proton	$^{15}O(p,p)$ or $^{15}N(p,p)$	Mylar (gas cell windows)
3	Proton	$^{15}O(p,p)$ or $^{15}N(p,p)$	Mylar (gas cell windows)
4	Alpha	$^{15}O(\alpha,\alpha)$ or $^{15}N(\alpha,\alpha)$	^{4}He gas
5	?	$^{15}N(?, ?)?$	Mylar

As differential cross-sections needed to be extracted for the R-Matrix fits the 112 downstream LEDA strips were collated into 16 annuli. As each strip had been calibrated for energy and all timing offsets corrected for it was simply a case of summing the data from each strip.

With the data now sorted into angular bins the alpha particles of interest could be isolated. This was done using 16 manually configured 2D gates over the area of interest, area 4 (Figure 5.1). As the experimental data was free from background reactions impinging on the energy region under investigation this was the only method employed to isolate the particles of interest.

5.3 Reconstruction of Interaction Energies

The detected energy of the α-particles is not a measure of the true α-energy produced by the nuclear reaction. Instead it is the result of the elastically scattered α particles losing energy in various materials. In order to reconstruct the true α particle energy this energy loss must be corrected for. This was achieved by using an iterative energy-loss algorithm using various look up tables of energy losses from SRIM [58]. The elastic alphas mainly lost energy in three stages:

1. The remainder of the ^{4}He gas target.
2. The Mylar exit window.
3. The aluminium dead layer of the detector.

The only information from the detectors was the energy of the detected particle and the detector strip and therefore the angle upon which it was incident. As the target was thick and the energy loss of the beam through it much larger than the experimental resolution it was not sufficient to assume that all events occurred at the centre of the target. However four major assumptions were made:

1. Angular straggling effects were ignored with straight line paths assumed for each of the detected particles.
2. All events were assumed to be detected at the centre of the strip.

3. Interaction events were assumed to occur along the z-axis.

4. The gas volume divided into segments of 1mm in depth.

The process of energy loss correction was thus:

1. From the measured energy and strip number and assuming that the point of interaction was at the centre of the gas target the scattering angle was estimated.

2. Using this angle the alpha energy was corrected for energy losses through the various media in reverse order, i.e. the dead layers of the detector, the exit window and then ^{4}He.

3. The energy was converted into a centre of mass energy, E_{CM} (interaction energy) [59] via:

$$E_{\mathrm{CM}} = E_{\mathrm{lab}} \times \left(\frac{M_b + 4}{4M_b \cos^2 \theta_{LAB}}\right) \tag{5.2}$$

where E_{CM} is the centre of mass energy, E_{lab} the recoiling particle's energy in the lab, M_b the mass number of the beam and θ_{lab} the recoiling particle's laboratory angle.

4. From a look up table of the energy loss of the beam through 300mbar of ^{4}He (split into 1mm segments) the interaction energy was compared to that of the beam. The interaction energy then gave a new point of origin within the cell. This was assumed to be the origin and the process was started again with a new calculated angle.

5. The process continued until the calculated point of interaction did not change by more than 2mm. An event which did not converge after 10 iterations was discarded, this condition however was never met. The final energy calculated was taken to be the fully corrected α-particle energy.

The effects on the experimental data can be seen clearly in Figure 5.4.

The data now energy corrected and converted into centre of mass energies were then examined for consistency. It was during this stage of the analysis that it was noticed that two of the seven segments of LEDA were not functioning correctly. The data from the two segments showed fluctuating yields and energy drifts. For the remainder of the analysis the data from these two segments were ignored.

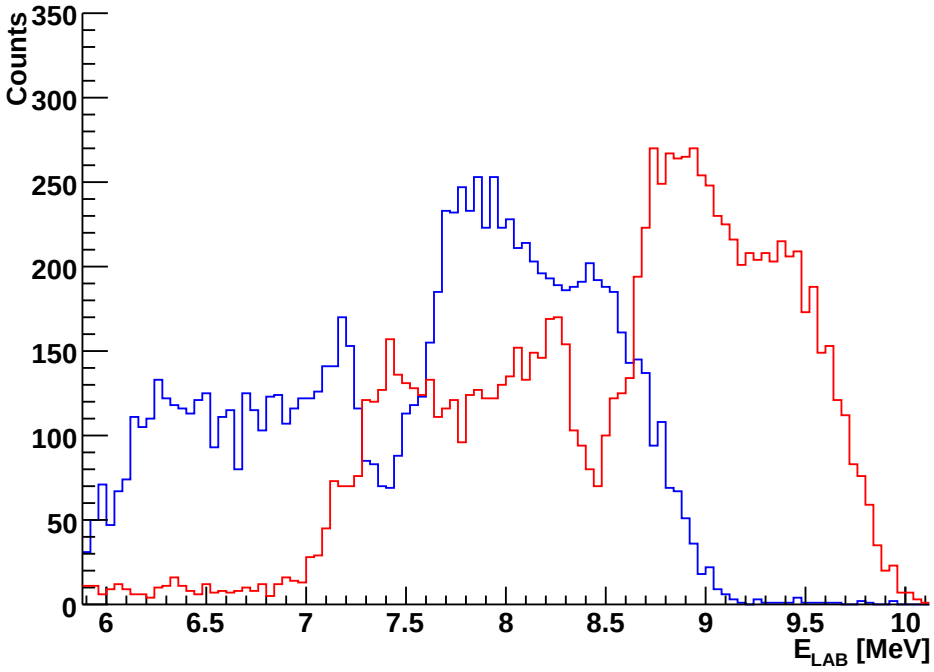

Figure 5.4: *An ADC spectrum illustrating the α correction algorithm. The blue line shows the raw $^{15}O(\alpha,\alpha)$ data at beam energy E_{lab} = 20.3 MeV, the red line shows the amended spectrum.*

5.4 Beam Normalisation and Differential Cross-Sections Calculated

A time averaged beam intensity was calculated using the Rutherford backscattering ^{15}O / ^{15}N from the ^{197}Au target mounted directly in front of the target. The intensity for each beam species was calculated for both their respective foreground and background runs. The average intensity was then calculated over all 4 segments of LEDA from those which satisfied Chauvenet's principle[1]. The calculated beam current had two uses:

1. Normalisation of data, firstly between foreground and backgrounds runs to allow for subtraction. It also allowed for normalisation between different data sets on the same target but with different beam energies as in the case of the ^{15}N(α,α) reaction.

2. To calculate the differential cross-section for each of the reactions.

The normalisation of the data is best illustrated in the ^{15}N(α,α) data set. Figure 5.5 shows two spectra, the first presents the un-normalised elastic alpha yields *vs* E_{CM} spectra for the two beam energies (E_{LAB}=18.9 and 20.3 MeV) on the same axis, the second shows the same data set but normalised and background subtracted.

The data, now fully energy corrected and normalised, allowed for background subtraction and, in the case of ^{15}N(α,α) were summed to form one data set. At this stage data from interactions at the beginning and end of the target were also discarded. The fully normalised yields in conjunction with other known factors allowed for the calculation of the differential cross section for each reaction. This was calculated for each of the 16 annuli via equation 5.3:

$$(\frac{d\sigma}{d\Omega}) = \frac{\text{yield per annulus}}{N_t \times N_p \times d\Omega \times L.T.} \tag{5.3}$$

where N_t is the number of ^{4}He target atoms. This was calculated from the thickness of ^{4}He needed for the beam species to lose E_{CM} = 10 keV[2] using equation 5.4, N_p the time averaged beam current, $d\Omega$ the solid angle (centre of

[1]Data which differs from the mean by two standard deviations were rejected.
[2]The data are plotted in E_{CM} = 10 keV bins

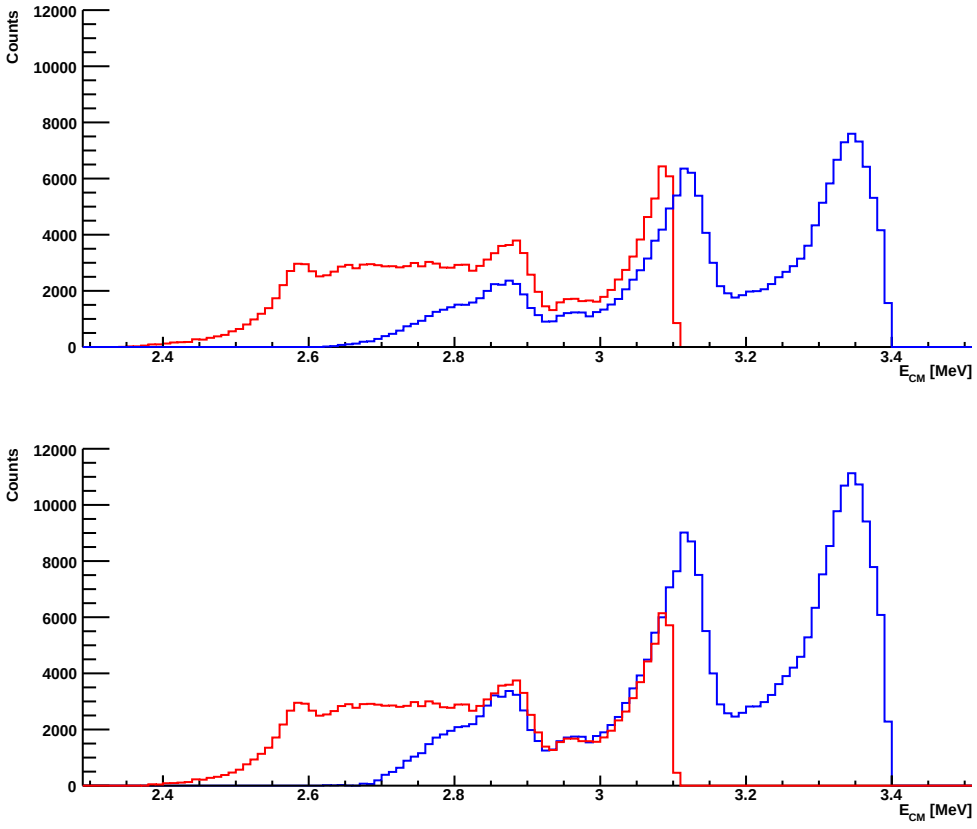

Figure 5.5: *Un-normalised and normalised ^{15}N data. The top figure shows the un-normalised $^{15}N(\alpha,\alpha)$ data, the red line being that from beam energy E_{LAB}=18.9 MeV, the blue data from beam energy E_{LAB}=20.3 MeV. The bottom figure illustrates the data background subtracted and fully normalised with respect to the E_{LAB}=18.9 MeV data set*

mass) subtended by the annuli of LEDA being examined and $L.T.$ is the live time, the ratio of triggers accepted to the number of triggers.

$$N_t(atoms\ cm^{-2}) = \text{Thickness } {}^4\text{He(cm)} \times 9.66 \times 10^{18}(atoms\ cm^{-3} \times \frac{\text{Gas Pressure(Torr)}}{\text{Temperature(K)}} \quad (5.4)$$

Figures 5.6 and 5.7 show the final excitation functions for each of the 16 annuli to be fitted for ^{15}O(α,α) and ^{15}N(α,α) respectively.

Due to the limited statistics in the ^{15}O(α,α) data set the excitation functions that are fitted are the result of summing the data from 4 annuli and calculating the differential cross-section. The data was then analysed via the R-matrix method.

5.5 *R*-Matrix Fits

The experimental data was analysed using the R-matrix code DREAM [60]. The R-matrix functions were calculated from input parameters and the best fit determined using MINUIT [61], a FORTRAN function which fits via minimisation of χ^2.

Due to the high experimental yields attained in the experiments the statistical errors were very small, ∼1-2% for ^{15}N(α,α) and ∼2-3% for ^{15}O(α,α). If the data were fitted with only statistical errors included the fitting algorithm was hindered from working optimally. The systematic experimental error arises from uncertainties in calculating the differential cross-section from the yields. The data was fit with both statistical and systematic errors included. An error of 10% on the cross-section was set for all experimental data points.

This 10% error was calculated via summing in quadrature the respective errors from the individual factors that are used to calculate $\frac{d\sigma}{d\Omega}$. These are as follows:

1. 2% statistical error within the yield.
2. 10% error in N_t. Gas pressure during experimental runs was kept within a ±10% limit.
3. 1.7% error in N_p
4. 1% error in $d\Omega$

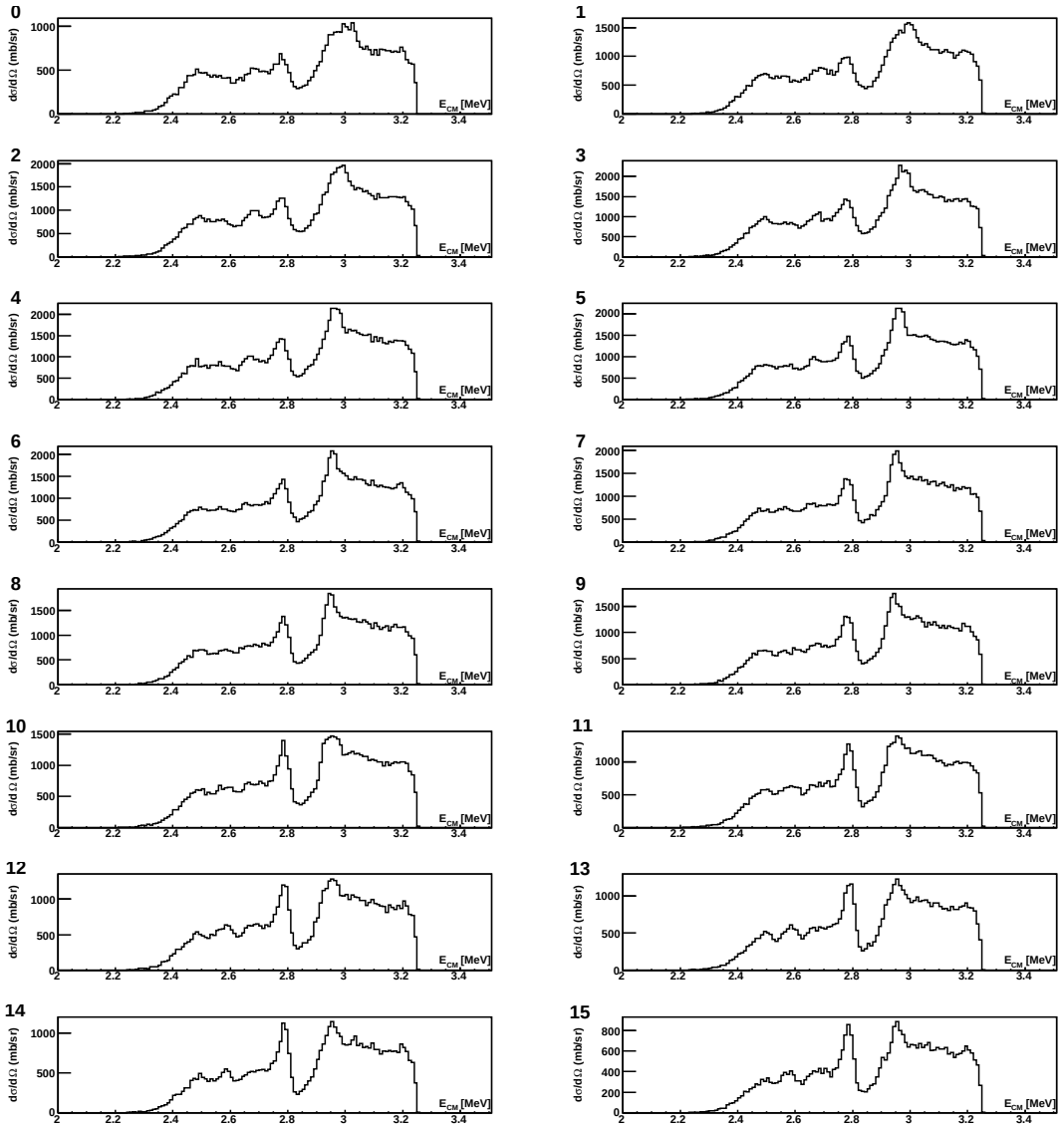

Figure 5.6: $\frac{d\sigma}{d\Omega}$ *vs* E_{CM} *for the 16 annuli of LEDA for the* $^{15}O(\alpha,\alpha)$ *reaction. The top left spectrum is that of strip 0 (most backward laboratory angle), the bottom right spectrum is that of strip 15 (most forward laboratory angle)*

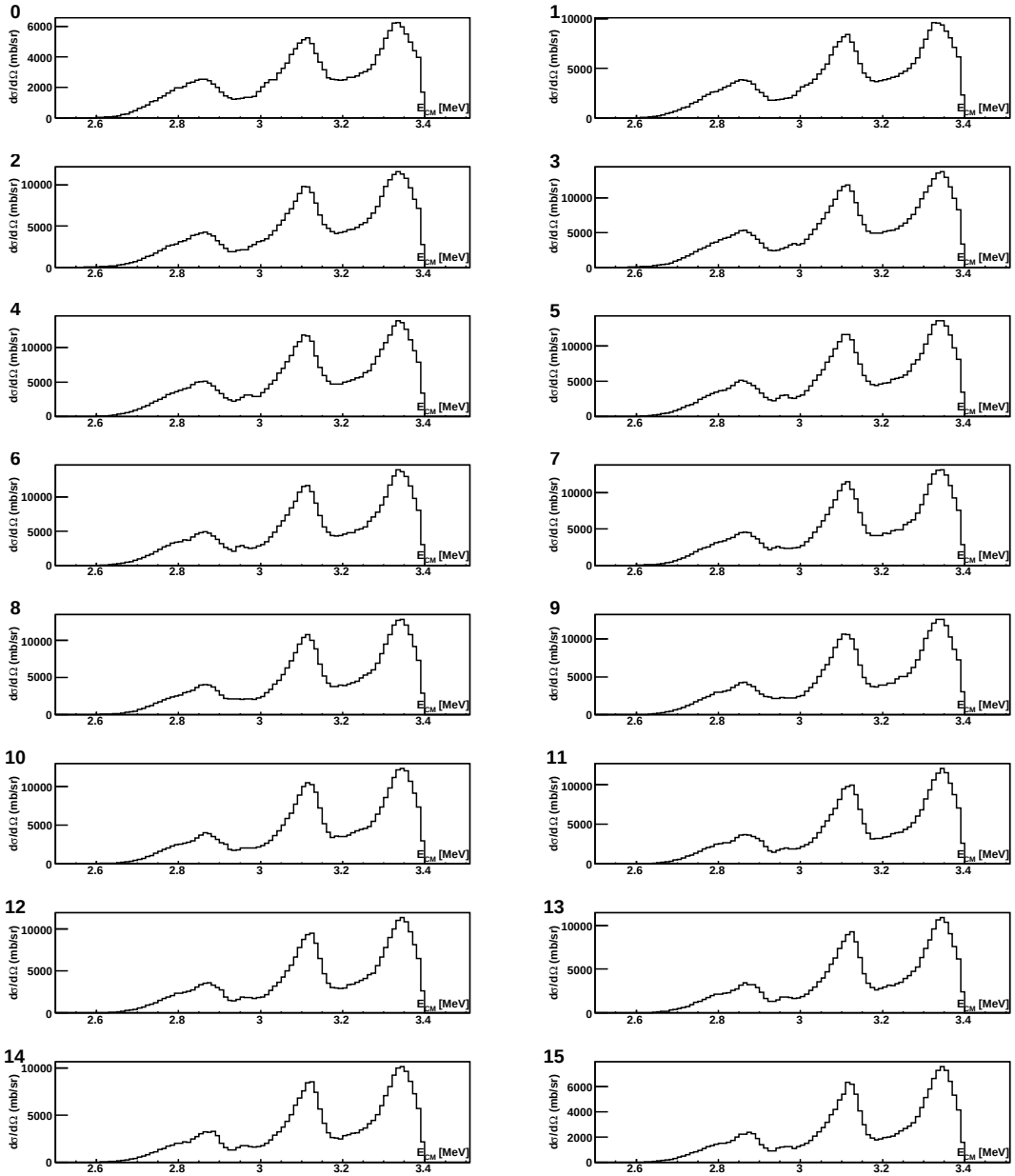

Figure 5.7: $\frac{d\sigma}{d\Omega}$ *vs* E_{CM} *for the 16 annuli of LEDA for the* $^{15}N(\alpha,\alpha)$ *reaction. The top left spectrum is that of strip 0 (smallest centre of mass angle), the bottom right spectrum is that of strip 15 the most forward laboratory angle*

5. 1% error in the live time

Summing these in quadrature gives a total error of 10.4 %.

5.5.1 ^{15}N(α,α) fits

As discussed in Chapter 4.2.1 the primary reason to study the ^{15}N(α,α) reaction was to validate the experimental and analysis techniques employed. The R-Matrix fitting code used minimises the reduced χ^2 on a calculated R-matrix excitation function calculated with initial input parameters of spin, parity, energy and alpha width. These initial parameters were taken from the most recent study of the level structure of ^{19}F, a re-analysis of Smotrich *et al* [50] by Bardayan *et al* [1]. The experiment consisted of alpha particles being elastically scattered by ^{15}N.

With the error of 10% set the initial input parameters were varied both individually and simultaneously to minimise the χ^2[1]. Once no further reduction could be achieved the fits were optimised via two other parameters, r_{max} (section 2.3) the nuclear radius and ΔE, the experimental resolution. The parameter r_{max} is a direct result of the R-matrix theory itself. ΔE is a factor which models the 'smearing' of the data as a result of the factors affecting the overall energy resolution, such as, straggling, kinematic shifts and detector resolution. The larger the value of ΔE the less detail is apparent within the excitation function. Through variations of this parameter an optimum ΔE can be set which results in the smallest reduced χ^2. The effects of variations of these two parameters on the reduced χ^2, and their subsequent optimal values can be seen in Figures 5.8 and 5.9.

It can be seen that the values achieved agree with the calculated values shown in Appendix B of $\Delta E_{\mathrm{CM}} \sim 18.5$ keV (FWHM) and r_{max} of 6.08 fm.

With this done the reduced χ^2 was again minimised with respect to the energies and α-widths of the states. Through subsequent and successive minimisation of the energy and width of each excited state at two angles (θ_{CM} 167.9° and 161.8°) simultaneously an optimum fit was reached with a χ^2 of 0.74 at 167.9° and a χ^2 of 0.68 at 161.8°, with a total χ^2 of 0.71. The experimental data and fits can be seen in Figure 5.10.

[1] Initial values of $r_{\mathrm{max}} = 5.9$ fm and $\Delta E = 22$ keV were used

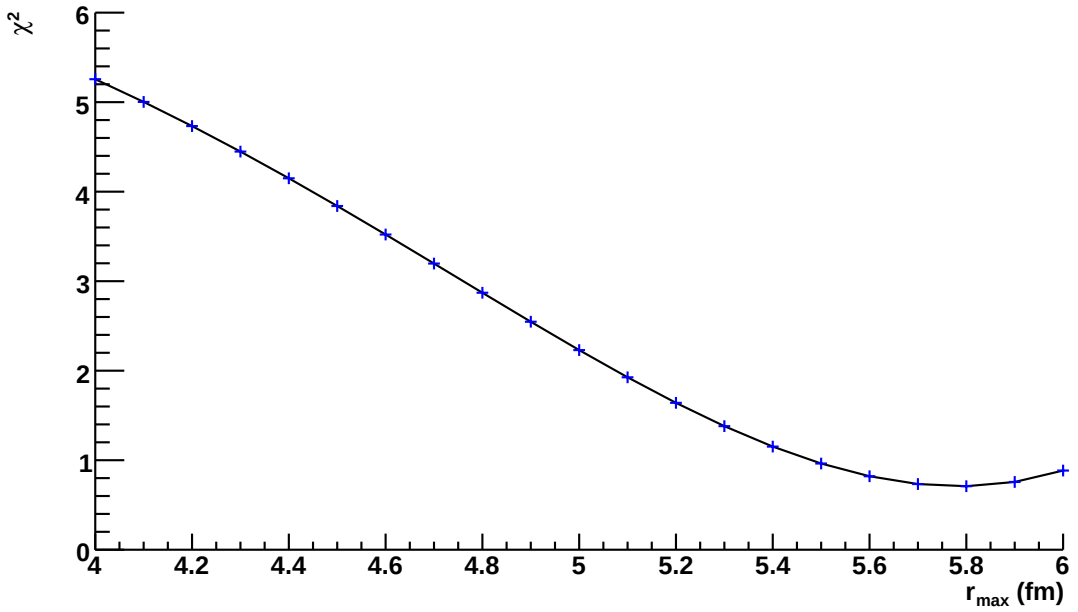

Figure 5.8: χ^2 *versus* r_{max} *for the* $^{15}N(\alpha,\alpha)$ *reaction. The minima at* r_{max} = *5.8 fm is used in the final fits.*

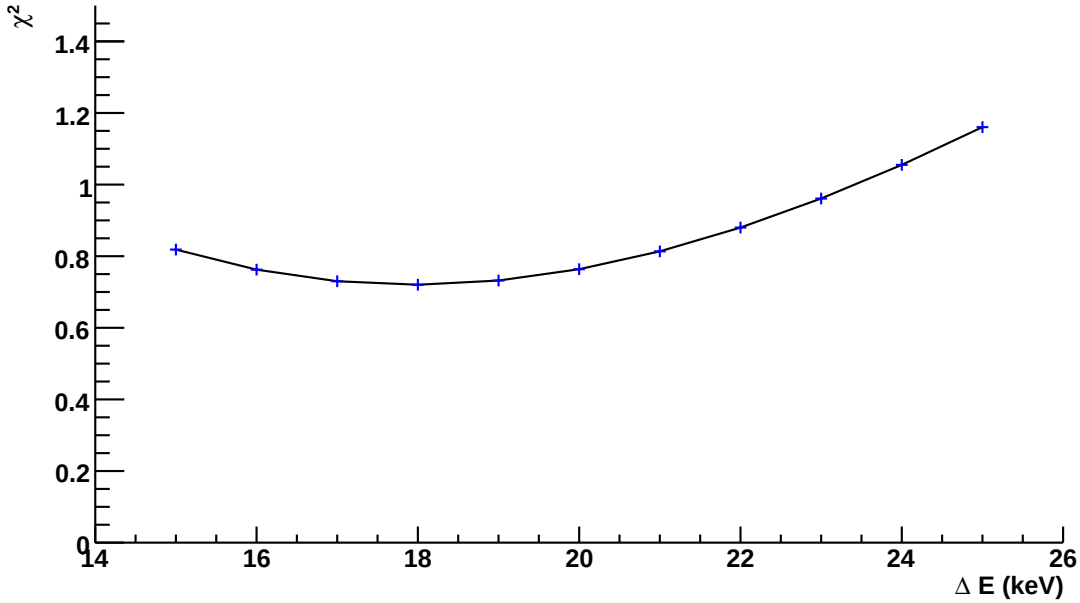

Figure 5.9: χ^2 *versus* ΔE *for the* $^{15}N(\alpha,\alpha)$ *reaction. The minima at* ΔE = *18 keV is used for the final fits.*

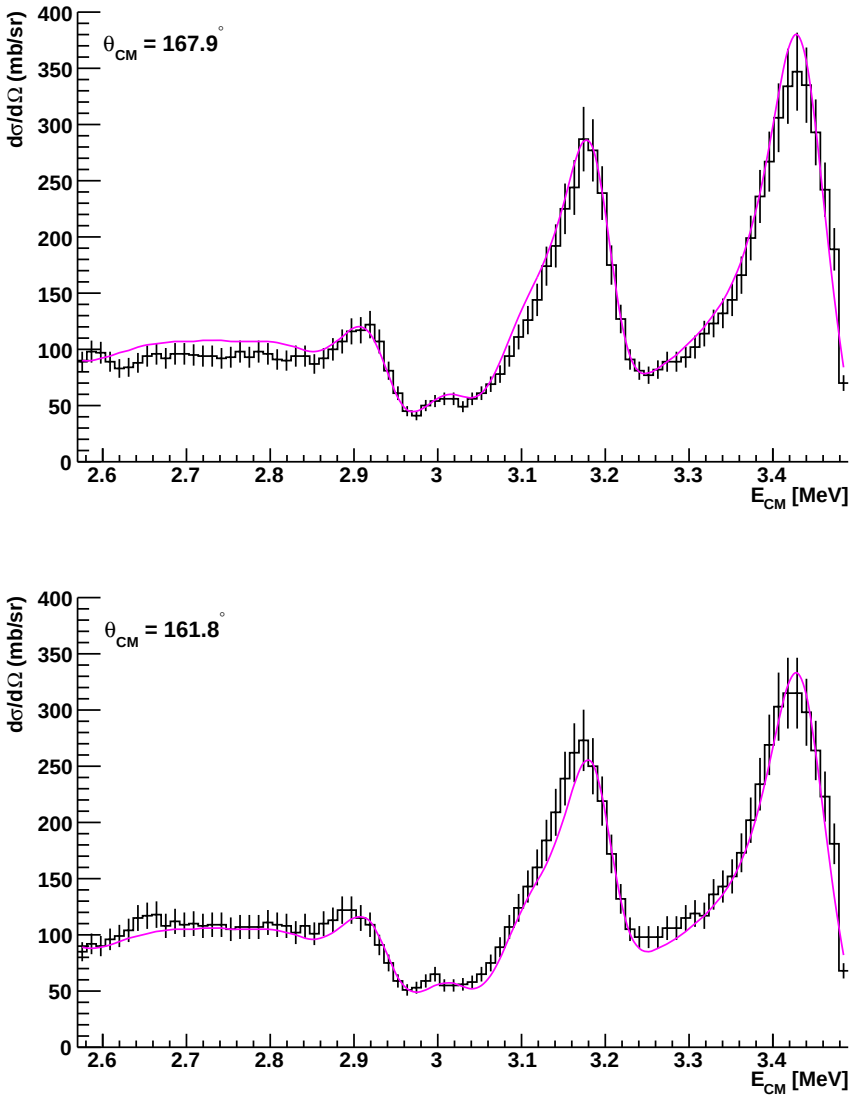

Figure 5.10: *R-matrix data and fits for the two angles (θ_{CM} 167.9° and 161.8°) studied in the $^{15}N(\alpha,\alpha)$ reaction. The resultant χ^2 is 0.71.*

The final resonance parameters are detailed in Table 5.2 alongside those from the Bardayan *et al* [1] paper, with 5.12 illustrating this graphically.

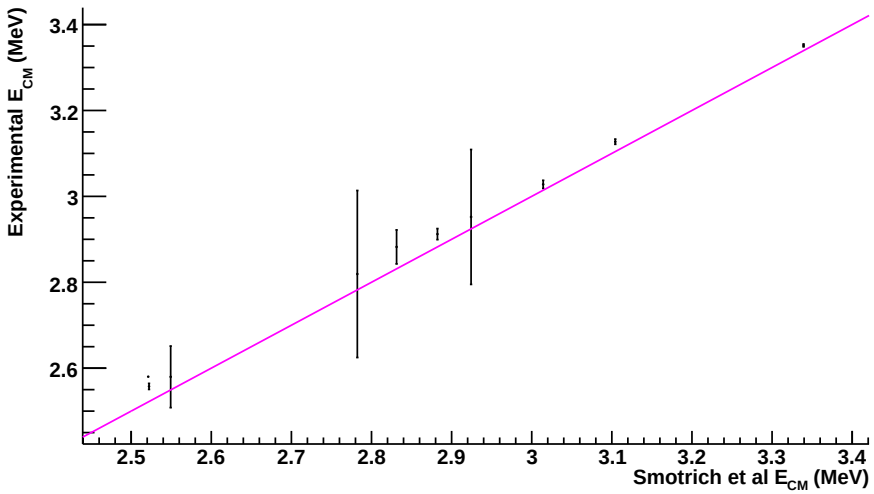

Figure 5.11: *Comparison of experimental* ^{19}F *resonance energies with those from the re-analysis of the Smotrich et al data [1]. The figure illustrates a systematic difference of* $\sim$ *30 keV between the two data sets. The red lines is* $y = x$.

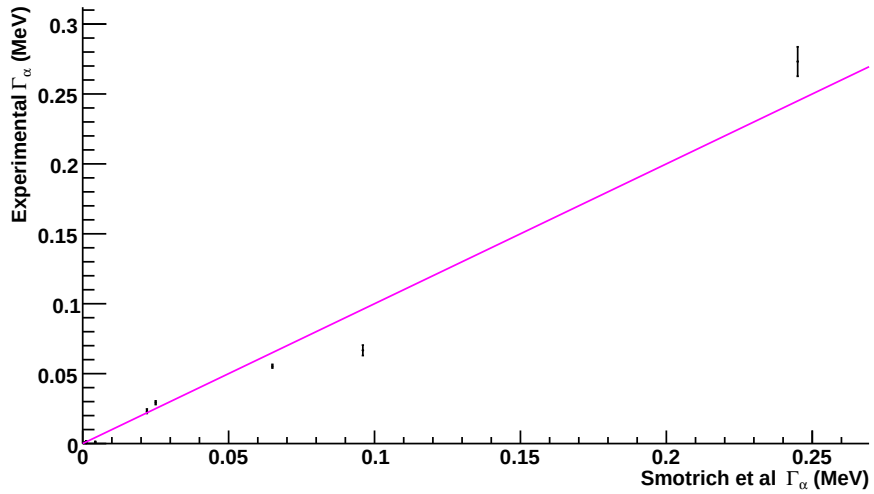

Figure 5.12: *Comparison of experimental* ^{19}F *resonance* Γ_α *with those of the re-analysis of the Smotrich et al data [1]. The red lines is* $y = x$.

Table 5.2: Level structure of ^{19}F resulting in experimental data best fit. Also shown is [1] for comparison.

Current Experimental Data				Smotrich Re-Analysis[1]			
E_r (MeV)	J^π	Γ_α(keV)	γ_α(keV)	E_r (MeV)	J^π	Γ_α(keV)	γ_α(keV)
2.56(0.007)	$\frac{1}{2}^-$	273(11)	207	2.52	$\frac{1}{2}^-$	245(6)	196
2.57(0.072)	$\frac{7}{2}^+$	0.45(0.05)	0.33	2.55	$\frac{7}{2}^+$	0.3(0.2)	0.23
2.58( )	$\frac{3}{2}^+$	3.5(0.06)	0.26	2.52	$\frac{3}{2}^+$	1.2(0.4)	0.96
2.82(0.194)	$\frac{3}{2}^-$	1.1(0.42)	0.58	2.78	$\frac{3}{2}^-$	4.3(0.5)	2.41
2.88(0.040)	$\frac{5}{2}^+$	1.7(0.26)	0.83	2.83	$\frac{5}{2}^+$	1.2	0.64
2.91(0.013)	$\frac{3}{2}^-$	23.1(1.6)	11.2	2.88	$\frac{3}{2}^-$	22(2)	11.0
2.95(0.157)	$\frac{7}{2}^-$	0.9(0.29)	0.42	2.92	$\frac{7}{2}^-$	0.9(0.2)	0.43
3.03(0.009)	$\frac{1}{2}^-$	66.7(3.7)	28.9	3.01	$\frac{1}{2}^-$	96(6)	42.1
3.13(0.006)	$\frac{5}{2}^+$	29.2(1.3)	11.6	3.10	$\frac{5}{2}^+$	25(4)	10.1
3.35(0.003)	$\frac{7}{2}^+$	55(1.3)	18.5	3.34	$\frac{7}{2}^+$	65	21.9

5.5.2 ^{15}O(α,α) fits

The excitation functions were calculated in the same manner as for the ^{15}N data using the DREAM code with the initial input parameters taken from a host of previous experimental data, Nesaraja *et al* [36], Bardayan *et al* [34] and Utku *et al* [30]. As the data collected also included the energy range below the threshold where no previous direct measurements have been taken resonance properties were inferred from information from the mirror nucleus [1]. All known states were included when fitting the data bar the higher spin states (J = $\frac{9}{2}$ and above) to which the experimental method was not sensitive as the momentum cross product of the entrance and exit channel did not reach this value.

As per the ^{15}N data, the excitation function and χ^2 were computed with the initial resonance parameter inputs and errors of 10%. In this case three[1] angles were fitted simultaneously, the yields of which were as a result of summing 4 annuli to achieve adequate statistics. Following an initial fit of the data the resonance parameters of $r_{\max}$ and ΔE were varied until a minimum χ^2 was found, the results and values attained can be seen in Figures 5.13 and 5.14.

The energies and alpha widths were then once again varied to optimise the fits on the data. The final fits can be seen in Figure 5.15, with the input parameters giving the best fit detailed in Table 5.3. The resultant $\chi^2 = 0.34$ was achieved over the three angles fitted simultaneously ($\chi^2 = 0.51$ at 168.1°, $\chi^2 = 0.27$ at 164.2° and $\chi^2 = 0.23$ at 160.3°.)

The reduced widths were calculated for each state to allow for a more robust comparison with the mirror nucleus as it is not an energy dependent term. The $\frac{5}{2}^+$ at -94keV[2] had not been previously observed directly. The area of astrophysical interest lies above the threshold with explicit interest in the possible $\frac{3}{2}^+$ doublet. Previous experiments had found the two $\frac{3}{2}^+$ states to be above threshold however this experiment found the optimal excitation function fit with the two states straddling the threshold.

The errors stated in table 5.3 are calculated individually, however, due to the nature of the excitation function it is safe to assume that there will be a correlation between one state's properties and that of another when minimising the χ^2. The DREAM code outputs the correlation matrices for given states. Due

[1] Data from the full angular range of LEDA were not included as the most backward of laboratory angles was of poor quality

[2] With respect to the ^{18}F + p threshold

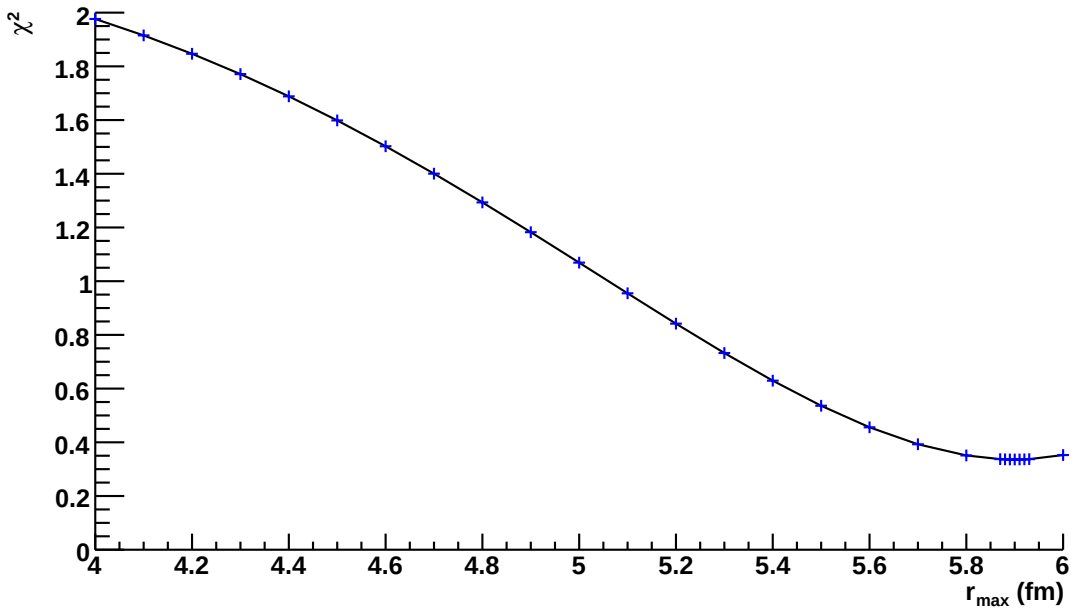

Figure 5.13: χ^2 *versus* r_{max} *or the* $^{15}O(\alpha,\alpha)$ *reaction. The minima at* r_{max} = *5.9 fm is used for the final fits.*

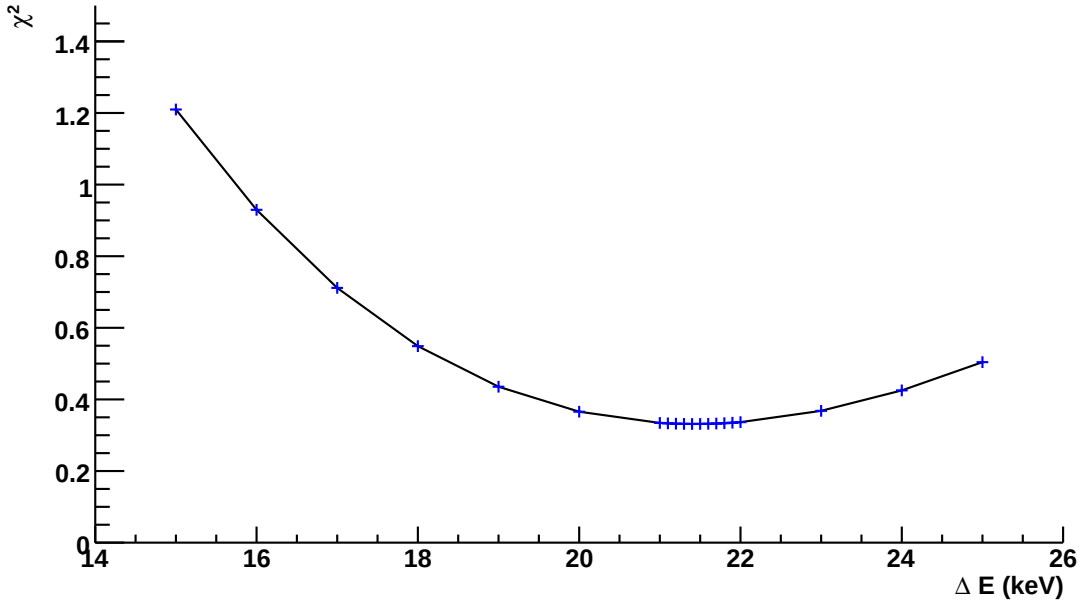

Figure 5.14: χ^2 *versus* ΔE *for the* $^{15}O(\alpha,\alpha)$ *reaction. The minima at* ΔE = *21.4 keV is used for the final fits.*

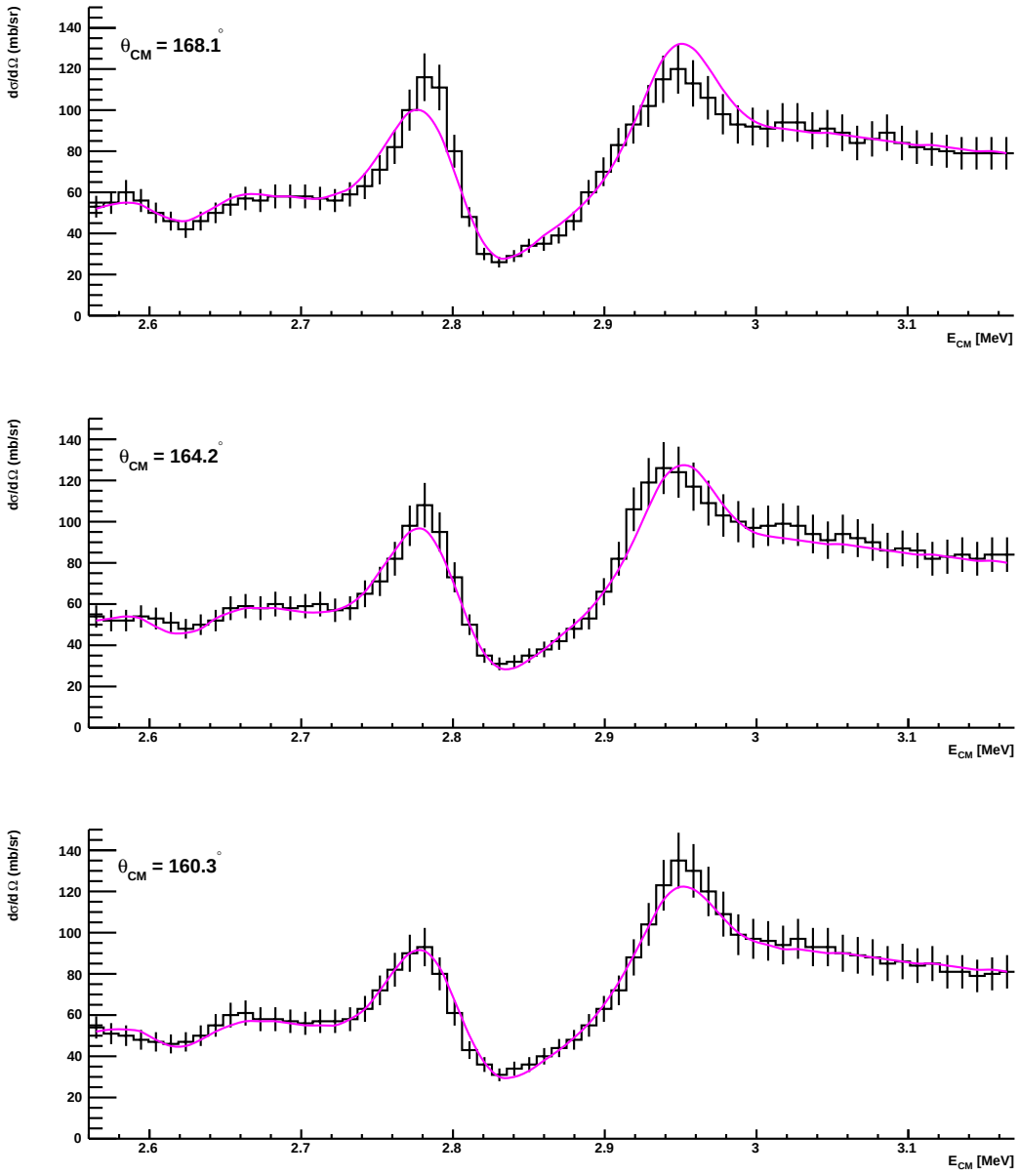

Figure 5.15: *R-matrix data and fits for the three angles (θ_{CM} 168.1°, 164.2° and 160.3°) studied in the $^{15}0(\alpha,\alpha)$ reaction. The resultant total χ^2 is 0.34.*

Table 5.3: Experimental level Structure of ^{19}Ne. Also shown are initial fitting parameters

Current Experimental Data					Initial Parameters			
E_x (MeV)	E_r(keV)	J^π	Γ_α(keV)	γ_α(keV)	E_x (MeV)	E_r(keV)	J^π	Γ_α(keV)
6.119	-292(85)	$\frac{7}{2}^+$	0.33(0.015)	0.437	-	-	-	-
6.154	-257(18)	$\frac{1}{2}^+$	18.8(1.9)	23.2	-	-	-	-
6.158	-253(131)	$\frac{3}{2}^-$	0.80(0.7)	0.98	-	-	-	-
6.196	-215(120)	$\frac{1}{2}^+$	2.04(1.4)	2.32	6.149	-262	$\frac{1}{2}^+$	2.4
6.317	-94(6.5)	$\frac{5}{2}^+$	12.6(0.4)	11.7	6.31	-102	$\frac{5}{2}^+$	10.3
6.389	-22	$\frac{3}{2}^+$	0.15(0.2)	0.126	6.419	8	$\frac{3}{2}^+$	0.27
6.414	3(17)	$\frac{3}{2}^+$	3.33(0.5)	2.67	6.449	38	$\frac{3}{2}^+$	1.3
6.445	34(3.4)	$\frac{1}{2}^-$	189(6.5)	145	6.439	28	$\frac{1}{2}^-$	220
6.479	68	$\frac{7}{2}^+$	0.15(0.4)	0.11	6.499	88	$\frac{7}{2}^+$	0.01

Table 5.4: Correlation matrix of resonance energies

J^π	$\frac{1}{2}^-$(34)	$\frac{5}{2}^+$(-94)	$\frac{3}{2}^+$(-22)	$\frac{3}{2}^+$(3)
$\frac{1}{2}^-$(34)	1	-0.079	-0.35	0.50
$\frac{5}{2}^+$(-94)	-0.079	1	0.11	0.04
$\frac{3}{2}^+$(-22)	-0.35	0.11	1	-0.30
$\frac{3}{2}^+$(3)	0.50	0.04	-0.30	1

Table 5.5: Correlation matrix of resonance widths

J^π	$\frac{1}{2}^-$(34)	$\frac{5}{2}^+$(-94)	$\frac{3}{2}^+$(-22)	$\frac{3}{2}^+$(3)
$\frac{1}{2}^-$(34)	1	-0.76	0.16	0.26
$\frac{5}{2}^+$(-94)	-0.76	1	-0.37	-0.41
$\frac{3}{2}^+$(-22)	0.16	-0.37	1	0.84
$\frac{3}{2}^+$(3)	0.26	-0.41	0.84	1

to the number of parameters used in the fitting (9 E_x and 9 Γ_α) the number of possible combinations to examine the correlations between them is very large. Tables 5.4 and 5.5 details the correlation matrices of the energies and widths for the $\frac{5}{2}^+$, both $\frac{3}{2}^+$ and $\frac{1}{2}^-$ states.

As can be seen there is a strong correlation between each of the parameters considered, most profound of which is the strong correlation between the Γ_α of the two $\frac{3}{2}^+$ states.

The implication of these strong correlations is that any errors estimated by DREAM for the properties of the states are in fact underestimated and should be treated with caution. This is turn impacts directly upon the properties stated in Table 5.3, as there is a strong correlation between the states.

This is further investigated in section 6.1.1. States are removed from the initial fitting parameters and other inputs adjusted to re-minimise χ^2.

Chapter 6

^{15}O(α,α) Results and Interpretation

This chapter examines the results obtained from the analysis detailed in Chapter 5 and what can be inferred from them with regards to nuclear structure and therefore astrophysical scenarios.

6.1 Investigations of *R*-Matrix Fit Stability

The parameters obtained (Table 5.3) giving the optimal R-matrix fits to the data form the base from which it was possible to try various other resonance scenarios. The resultant changes in the fitted excitation function illustrate the importance of the parameters varied and therefore the validity of the conclusions regarding the nuclear structure which can be inferred from the experiment.

6.1.1 State Removal

The scenarios examined involved the removal of key individual states and monitoring their effects on the χ^2[1] of the fit. With the removal of a given state, alterations were made to the remaining resonance parameters with the aim of compensating for their removal. The following states were examined: $\frac{5}{2}^+$ (E_x = 6.317 MeV, E_r = -94 keV), both $\frac{3}{2}^+$(E_x = 6.389 MeV, E_r = -22 keV and E_x = 6.414 MeV, E_r = 3 keV), $\frac{1}{2}^-$ (E_x = 6.445 MeV, E_r = 34 keV) and the $\frac{7}{2}^+$ (E_x = 6.479 MeV, E_r = 68 keV) . The $\frac{5}{2}^+$, $\frac{1}{2}^-$ and the $\frac{7}{2}^+$ removal resulted with χ^2 values of 6.25, 13.2 and 1.09 respectively and their effects could not be

[1]The best fit of the data had a χ^2 = 0.34.

compensated for by manipulation of the remaining states, see Figure 6.1 for the effect of removing the $\frac{7}{2}^+$ state.

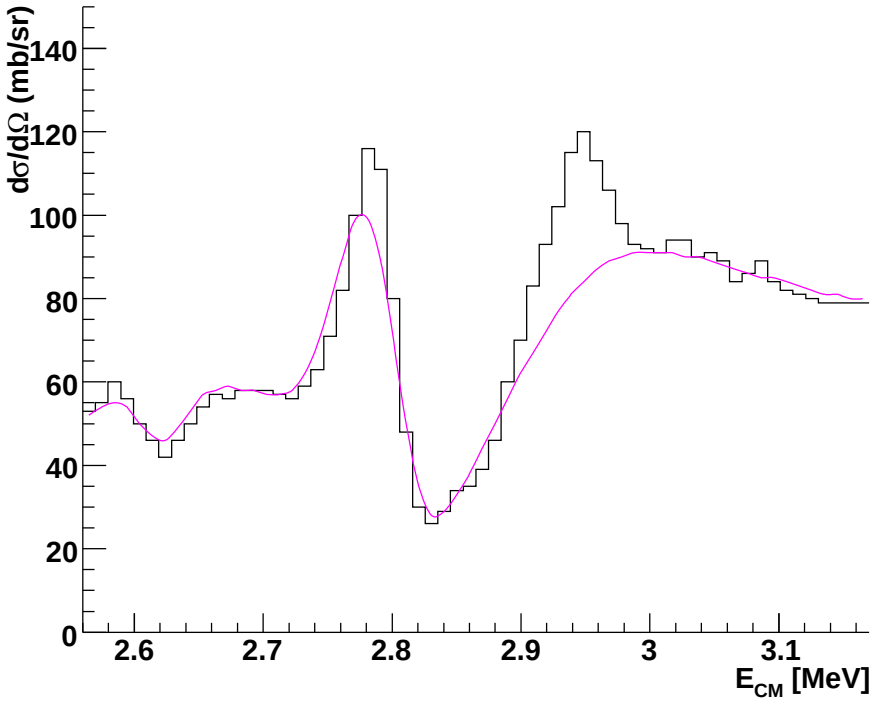

Figure 6.1: *The data at θ_{CM} 168.1° and the resultant best fit if the $\frac{7}{2}^+$ state at $E_{\mathrm{r}} = 68$ keV is removed.*

The removal of the $\frac{3}{2}^+$ did not result in such pronounced changes in the reduced χ^2. Each $\frac{3}{2}^+$ state was removed in turn and the χ^2 monitored. Removal of the -22 keV state gave a new χ^2 of 1.16. Through variation of the resonance parameters of the remaining $\frac{3}{2}^+$ state at 3 keV the χ^2 was minimised to 0.63. Further minimisation with respect to the $\frac{5}{2}^+$, $\frac{1}{2}^-$ states resulted in an optimum χ^2 of 0.54.

The process was repeated with the removal of the 3 keV state resulting in successive χ^2 values of 0.48, 0.45 and 0.42. In the two scenarios detailed above the state shifts for the 'compensation' can be seen in tables 6.1 and 6.2, the most noticeable change being the shift of the -22 keV state to +25 keV.

The effects of removing both $\frac{3}{2}^+$ states was also examined and resulted in a χ^2 of 1.01, the effects of which can also be seen in Figure 6.2. Adjustments

Table 6.1: Alterations to results to compensate for the removal of -22 keV $\frac{3}{2}^+$ state

	Optimal		Compensated	
J^π	E_{CM}(keV)	Γ_α(keV)	E_{CM}(keV)	Γ_α(keV)
$\frac{5}{2}^+$	-94	12.6	-94	12.9
$\frac{3}{2}^+$	3	3.33	5	1.66
$\frac{1}{2}^-$	34	189	19	205

Table 6.2: Alterations to results to compensate for the removal of 3 keV $\frac{3}{2}^+$ state

	Optimal		Compensated	
J^π	E_{CM}(keV)	Γ_α(keV)	E_{CM}(keV)	Γ_α(keV)
$\frac{5}{2}^+$	-94	12.6	-94	13.4
$\frac{3}{2}^+$	-22	0.15	25	0.0015
$\frac{1}{2}^-$	34	189	15	211

made to the $\frac{5}{2}^+$ and $\frac{1}{2}^-$ resonance parameters gave a reduced χ^2 of 0.42, the details of which are given in Table 6.3.

From these results it can be concluded that this experiment alone cannot determine convincingly the nature of the $\frac{3}{2}^+$ states, whether a doublet exists or if, in fact, there is a single $\frac{3}{2}^+$ state.

6.1.2 Upper Limits

Attempts to determine upper limits on the widths for the two $\frac{3}{2}^+$ states are shown in figure 6.3. The widths were examined individually while keeping all other resonance parameters as they were for the optimal fit. Γ_α was increased in a stepwise manner until the χ^2 had varied by one. For the -22 keV state the upper limit for Γ_α was $\sim$9 keV, the 3 keV state had an upper limit of 10 keV.

Table 6.3: Alterations to results to compensate for the removal of both $\frac{3}{2}^+$ states

	Optimal		Compensated	
J^π	E_{CM}(keV)	Γ_α(keV)	E_{CM}(keV)	Γ_α(keV)
$\frac{5}{2}^+$	-94	12.6	-94	13.6
$\frac{1}{2}^-$	34	189	14	211

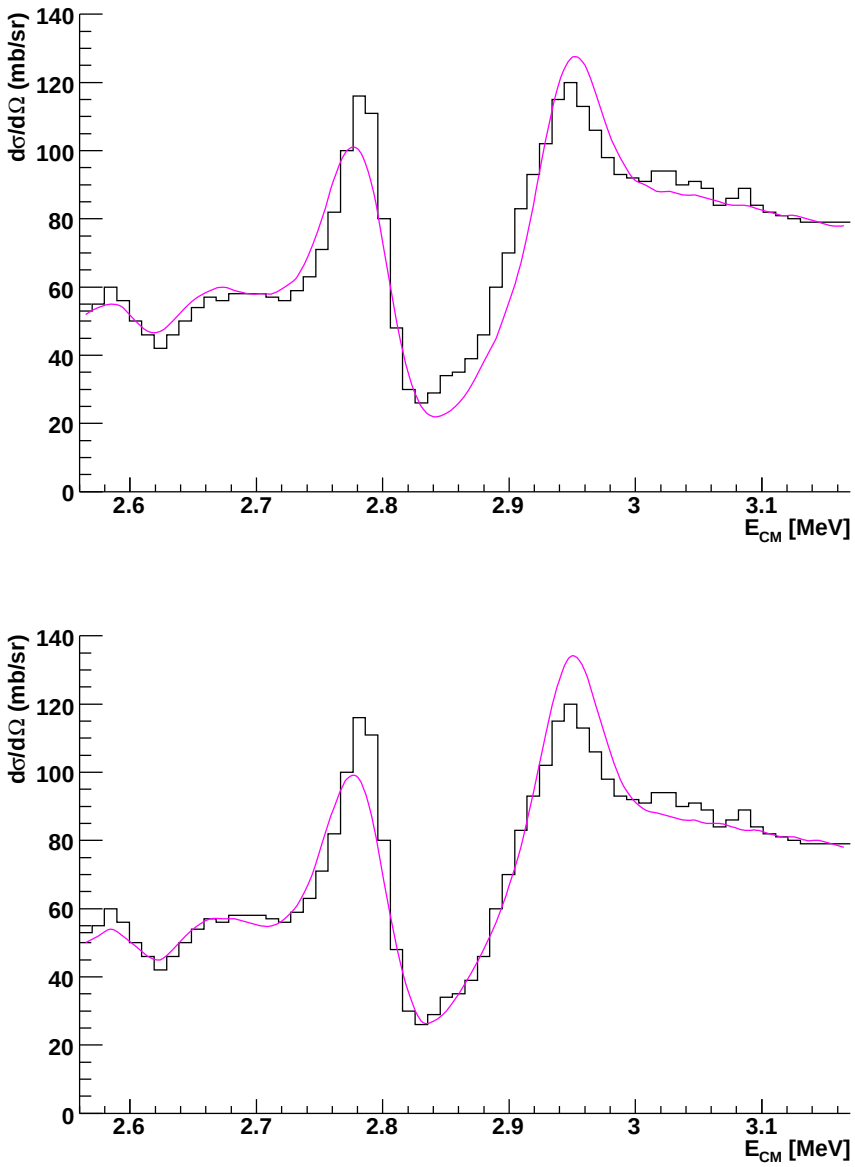

Figure 6.2: *The top figure shows data at* θ_{CM} *= 168.1° and the resultant excitation function if both* $\frac{3}{2}^+$ *states at* E_{r} *= -22 and 3 keV are removed. All other resonance state parameters are unchanged. The bottom plot shows the best fit of the same data with both* $\frac{3}{2}^+$ *states removed but with the resonance parameters of the* $\frac{5}{2}^+$ *and* $\frac{1}{2}^-$ *states to be re-optimised.*

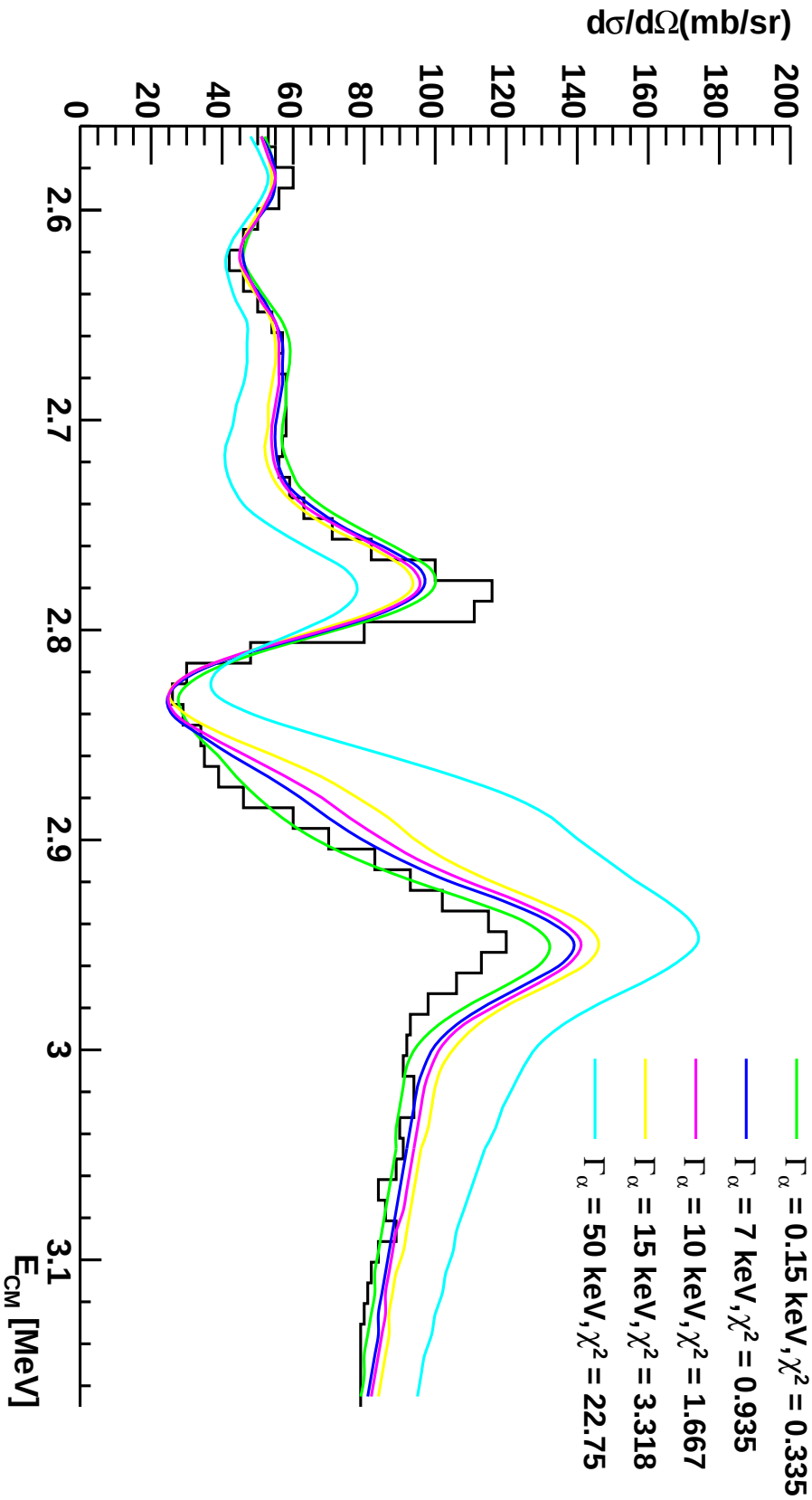

Figure 6.3: *Data at $\theta_{\mathrm{CM}} = 168.1°$ and the resultant fits with changes in Γ_α for the $\frac{3}{2}^+$ state at $E_\mathrm{r} = 3$ keV. This process was used to set an upper limit on Γ_α for this state.*

6.1.3 Energy Offset

From figure 5.12 it can be seen that the energies extrapolated from the experimental fits of the ^{15}N(α,α) reaction are systematically higher than those detailed in [1]. The average difference was ∼30 keV. Although this systematic difference cannot be transferred directly to the ^{15}O(α,α) as they are different reactions[1], the effects of shifting the experimental data down by 30 keV were examined. The input parameters for the resonance energies were also decreased by 30 keV and the data fitted to. The total χ^2 fit over the three angles simultaneously was 0.35.

This result is not surprising as the whole data set and input parameters were shifted by the same amount and thus one would expect similar χ^2. The result of the shift however would lead to the result of having both $\frac{3}{2}^+$ states well below threshold. This result would disagree with [30], the only experiment to date which has directly observed a $\frac{3}{2}^+$ state (original $\frac{3}{2}^+$ state at 8 keV) above the threshold.

6.1.4 Spin Parity Limits

The final scenario that was examined was whether the experimental data allowed one to determine the spin and parity of the $\frac{3}{2}^+$ states. The J^π for the two $\frac{3}{2}^+$ states were altered successively to $\frac{1}{2}^+$, $\frac{1}{2}^-$, $\frac{3}{2}^-$ with fits performed following each alteration. This yielded no dramatic affects on the χ^2. However at spins of $\frac{5}{2}^+$ and above there was a marked affect on the fits. This is not altogether surprising as the experimental setup (^{15}O(α,α)) is more sensitive to higher spins from the momentum cross-product than observing states in ^{19}Ne via the ^{18}F + p reaction.

6.2 Astrophysical Interpretation

Figures 6.4 and 6.5 show the four interference scenarios on the S-factor using the experimental resonance parameters and their derived upper limits respectively. Three $\frac{3}{2}^+$ states at E_x = -22, 3 and 665 keV are included within the calculation.

Figure 6.4 can be compared to Figure 3.2, which, detailed the same 4 calculated S-factors but using the previously known resonance parameters of the

[1] For this experiment the primary difference is in the energy losses of the projectiles through the target due to their differing Z

three $\frac{3}{2}^+$ states. As can be seen the main difference between the two calculations is as a result of one of the $\frac{3}{2}^+$ states being below the ^{18}F + p threshold. The interference effects between the doublet in all four cases are now likely to have the greatest impact below the threshold.

In [62] the ^{18}F + p reaction was studied directly between E_r = 400 - 700 keV. The aim of the experiment was to examine the tail ends of the $\frac{3}{2}^+$ state at E_r = 665 keV. From the results of the experiment and comparison to the S-factor plots of those detailed in Figure 3.2, the author was able to dismiss the interference scenario +++.

Future direct experiments coupled with the new spectroscopic information derived from this experiment should further narrow down the likely interference scenario and thus better determine the rate of the ^{18}F + p reaction.

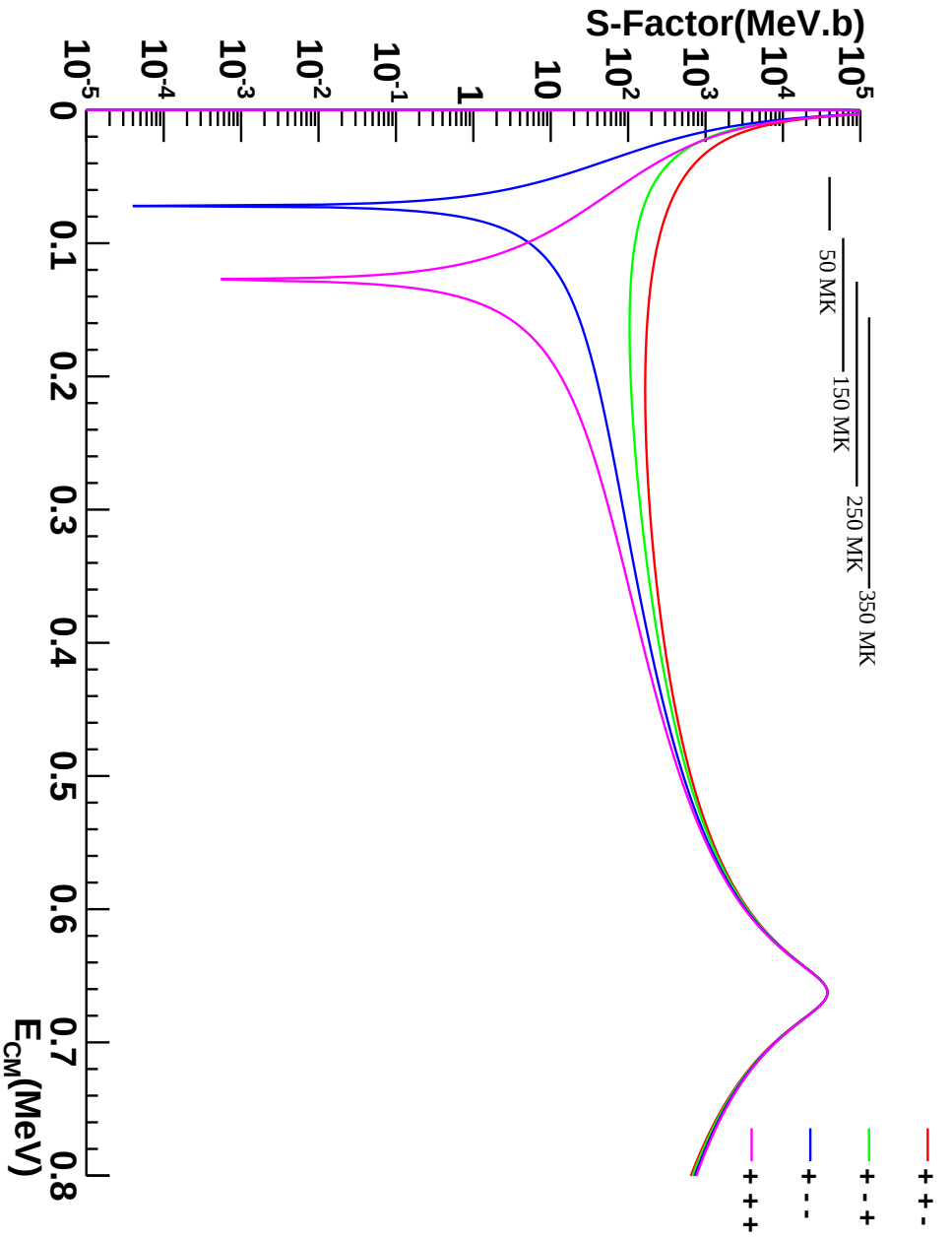

Figure 6.4: *Interference effects on the S-factor for the* $^{18}F(p,\alpha)$ *reaction calculated with the experimental parameters. For each case the only factor that has been altered are the interference effects. The nuclear radius has been kept constant at 5.9 fm. The temperature scales (top left) illustrate the Gamow energy window for the quoted temperatures. The area of interest for this reaction is therefore below* E_{CM}*=0.4 MeV as this corresponds to the astrophysical energy of interest.*

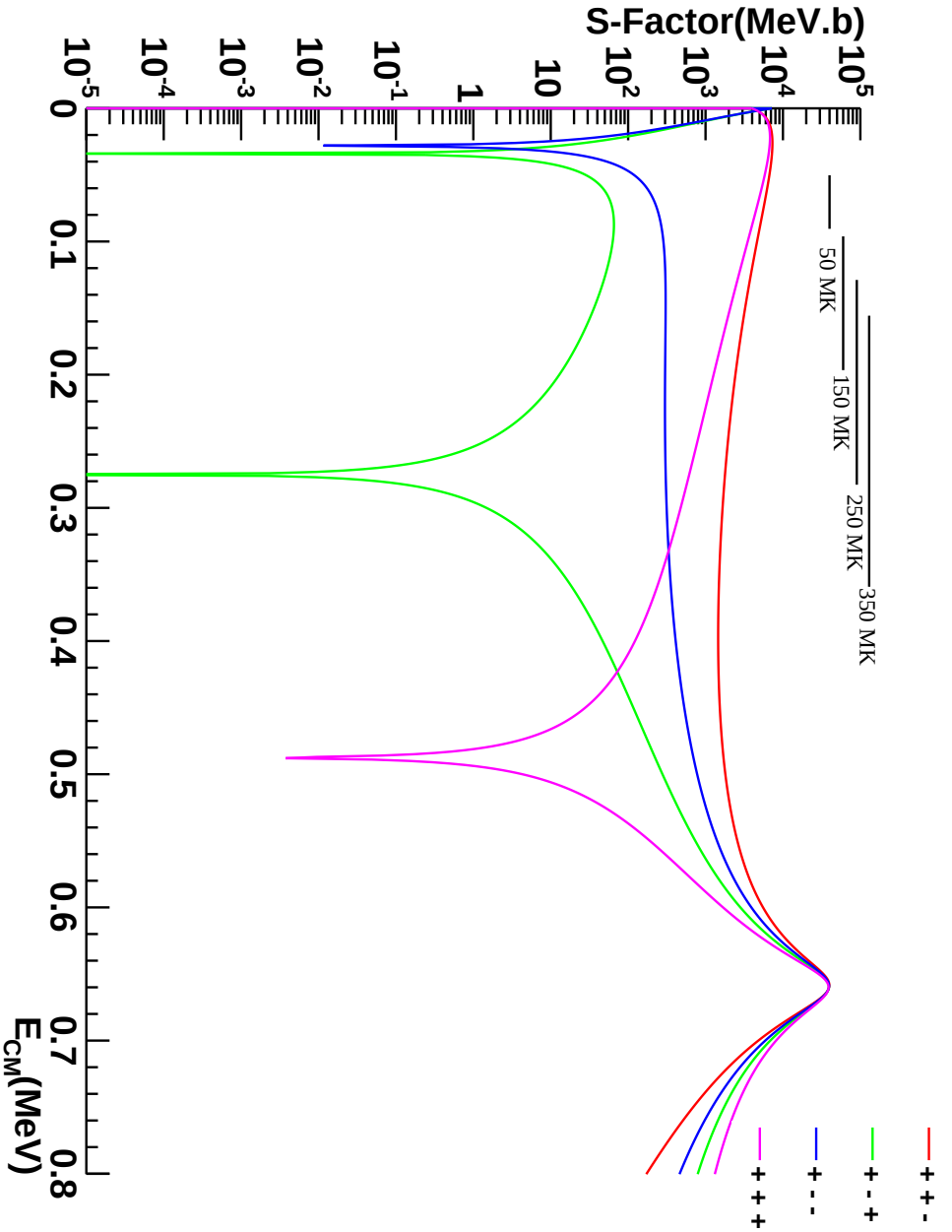

Figure 6.5: *Interference effects on the S-factor for the* $^{18}F(p,\alpha)$ *reaction calculated with the upper limits of* Γ_α *calculated for the two* $\frac{3}{2}^+$ *states at* E_r *= -22 and 3 keV. The nuclear radius has been kept constant at 5.9 fm.*

Chapter 7

^{18}Ne(α,p) Data Analysis and Results

This chapter will detail the methods employed for calibrating, sorting and fitting the experimental data for the ^{18}Ne(α,p) reaction. Given the similarities in the experimental setup with the ^{15}O(α, α) experiment the data analysis technique is also similar. Important differences are highlighted below.

7.1 ^{18}Ne(α,p) calibration

Although the type of silicon detector used in this experiment varied from those used in the ^{15}O(α,α) reaction the method for calibrating them was identical. As a $\Delta E - E$ detector configuration was employed the two detectors were calibrated individually over two runs since the ΔE detector stopped all the α particles reaching the E.

It is important to note that this technique normalises the detector calibration to α-particles, which was ideal for the ^{15}O(α,α). However for the ^{18}Ne(α,p) experiment the particles of interest are protons. It is known that silicon detectors have a non-linear response to low Z ions. This response has been measured [63] and a correction factor of 0.986 was thus applied to the detected proton energies to account for this effect.

7.2 Particle Identification

The relevant gains and offsets were incorporated into the analysis program and the experimental data sorted. The raw data was examined by considering the

2D spectra of ADC *vs* TDC hits. A typical ADC *vs* TDC spectrum for the ΔE and E detectors are shown in Figure 7.1.

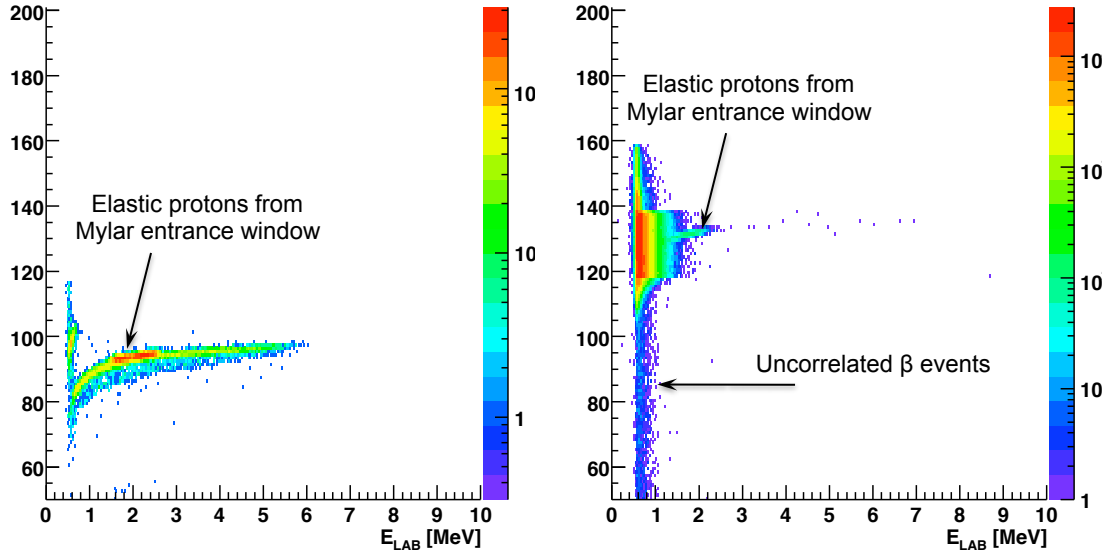

Figure 7.1: *Energy vs raw TDC spectrum for the* $^{18}Ne(\alpha,p)$ *reaction. The left hand figure shows a spectrum from the* ΔE *detector, with the right hand figure showing a typical spectrum from the* E *detector. In both cases a full gas target is in place. On each plot running along the y-axis are uncorrelated* β*-particles from the radioactive decay of the* ^{18}Ne *beam which have no timing information.*

From the spectra two main areas of interest can be identified:

1. Elastically scattered protons from the Mylar entrance window of the gas cell.

2. Reaction protons, maximum at $\sim$ 8 MeV (Final energy comes from summing the $\Delta E - E$ detector energies).

The spectra were not as clean (due to a shorter flight-path) as those of the $^{15}O(\alpha,\alpha)$ reaction and thus the 2D gating system employed in that analysis could not be used here. Instead the $\Delta E - E$ detector configuration was exploited for particle identification using the semi-empirical formula, Equation 7.1 [64]:

$$\frac{t}{a} \sim (\Delta E + E)^b - E^b \tag{7.1}$$

where t is the detector thickness, $a = 1/mZ^2$ and $b \sim 1.73$ for protons.

Figure 7.2 shows this particle identification plotted against energy in 10 keV bins. This spectra shows various particles which earlier were encroaching on the area of interest. The proton band of interest is highlighted. Underneath the bands a line appeared as a result of β-particles in random coincidence.

The particles identified as protons can be easily discerned and gated around. One should note that all detected protons, including the elastic ones from the Mylar windows are included in this spectrum, i.e. up to this point no data have been discarded.

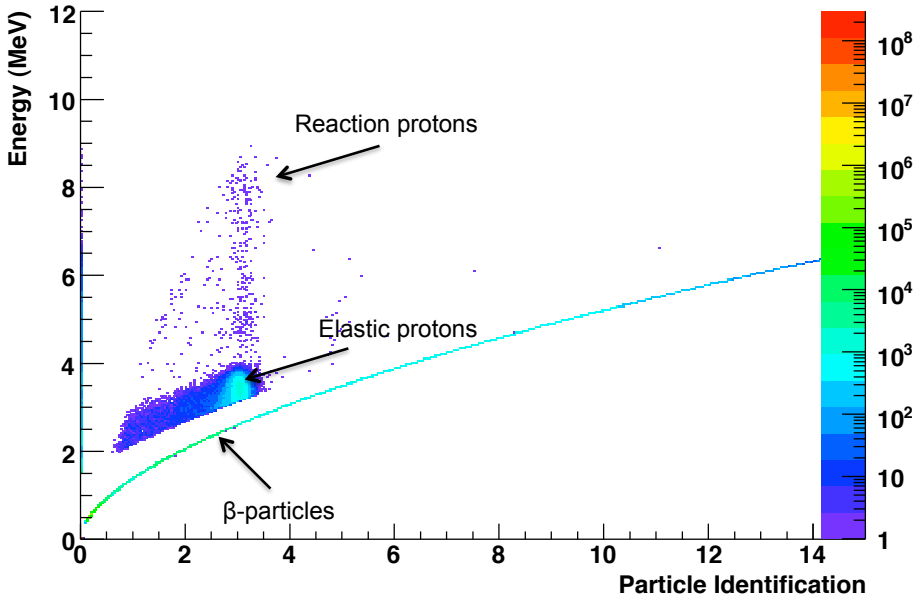

Figure 7.2: *Particle identification spectrum for the $^{18}Ne(\alpha,p)$ reaction. The proton band is centred at P.I. $\sim$ 3. The thin line that underpins the data set are uncorrelated β-particles.*

7.3 Reconstruction of Interaction Energies

With the protons isolated it was necessary to correct their detected energies for energy loss effects. The procedure was simpler for this experiment in comparison

to the ^{15}O(α,α) reaction, since a thin target was used. The experimental resolution (∼370 keV FWHM) was dominated by the energy loss of the ^{18}Ne beam through the target and thus the point of interaction could not be determined. It was therefore assumed that all interactions took place in the centre of the gas target.

From the difference in the strips hit in the ΔE and E detector, the angle of trajectory could be calculated and extrapolated back to the centre of the target and thus the path length through the aluminium exit window calculated. Energy losses of the protons through ^{4}He were ignored as they were negligible[1].

The next stage of the analysis was to convert the proton energy into a Q-value (Equation 7.2 [65]). This allowed the final excited state of the ^{21}Na nucleus to be determined.

$$E_x + Q = E_{\mathrm{p}}(1 + \frac{m_{\mathrm{p}}}{m_{^{21}\mathrm{Na}}}) - E_{^{18}\mathrm{Ne}}(1 - \frac{m_{^{18}\mathrm{Ne}}}{m_{^{21}\mathrm{Na}}}) - 2\frac{\sqrt{m_{\mathrm{p}} m_{^{18}\mathrm{Ne}}}}{m_{^{21}\mathrm{Na}}}\sqrt{E_{\mathrm{p}} E_{^{18}\mathrm{Ne}}}\cos\theta_{\mathrm{p}} \tag{7.2}$$

Once converted into excitation energies the results were plotted against yield, (Figures 7.3 and 7.4), for the two centre of mass energies investigated. A series of Gaussians were fitted to the data at $E_{\mathrm{CM}} = 2.5$ MeV. The three parameters of the Gausians were height, centroid and sigma. The centroids were all fixed with sigma and the height allowed to vary to minimise χ^2. A final constraint on the sigma for each Gaussian to be the same for each peak was also implemented. The final parameters of the Gaussians are shown in table 7.1.

7.4 Calculation of Total Cross-Section

7.4.1 Simulation

To calculate the total-cross section from the differential cross section, $\frac{d\sigma}{d\Omega}$, at a particular angle the angular distribution must be integrated. An assumption therefore had to be made about the angular distribution of particles since depending on the type of transition the distributions may favor a particular angle.

The simulation (Section 4.3.1.2) was used to study the effects of different distributions on the observed yield at the angles covered by the detector system.

[1] An 8 MeV proton will lose $E_{\mathrm{lab}} \sim 4$ keV in 2 cm of ^{4}He at 200 mbar

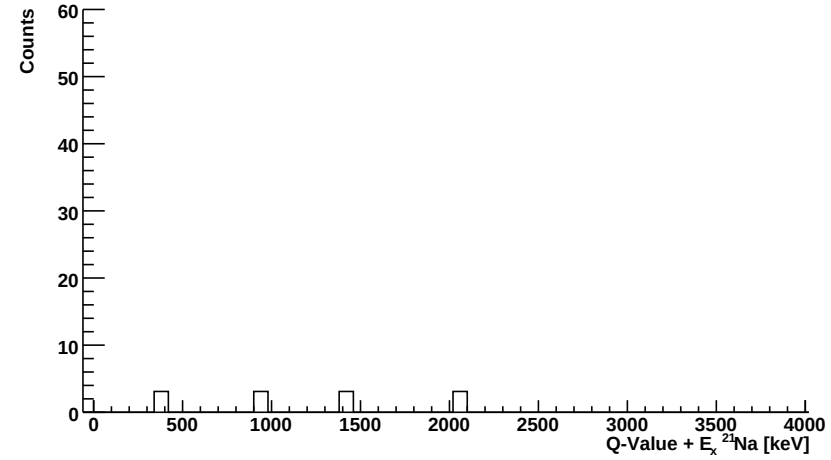

(a) Background Q-value spectrum for $E_{\mathrm{CM}} = 1.7$ MeV

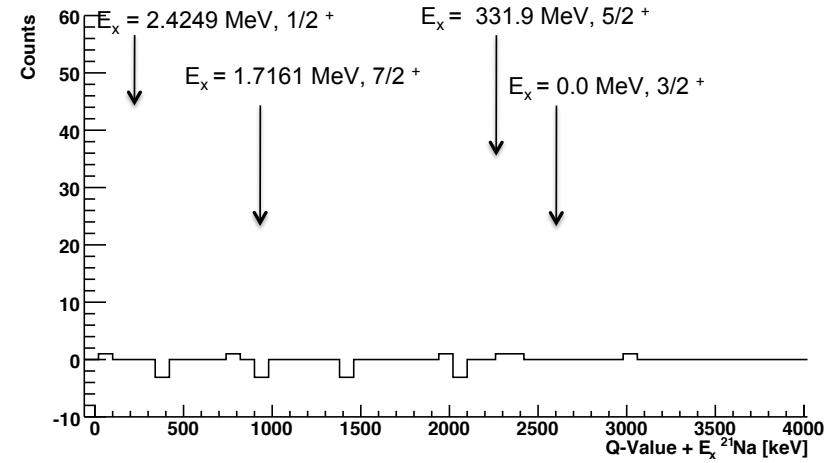

(b) Background subtracted Q-value spectrum for $E_{\mathrm{CM}} = 1.7$ MeV

Figure 7.3: *Background and background subtracted histogram for the* $^{18}Ne(\alpha,p)$ *reaction at* $E_{\mathrm{CM}} = 1.7$ *MeV*

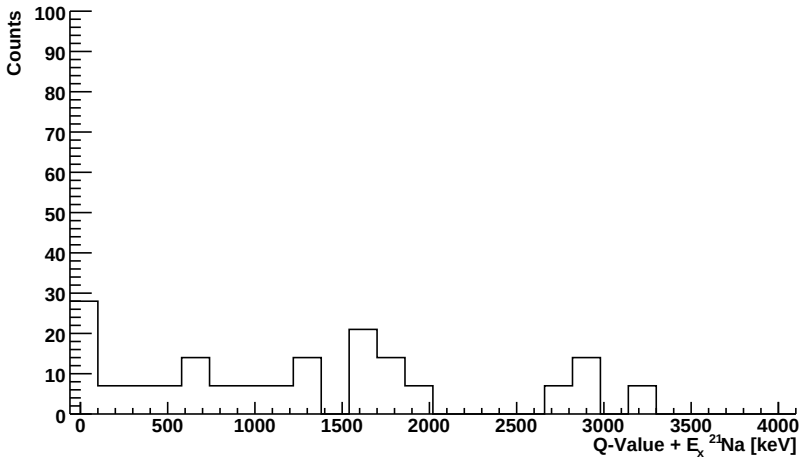

(a) Background Q-value spectrum for $E_{\mathrm{CM}} = 2.5$ MeV

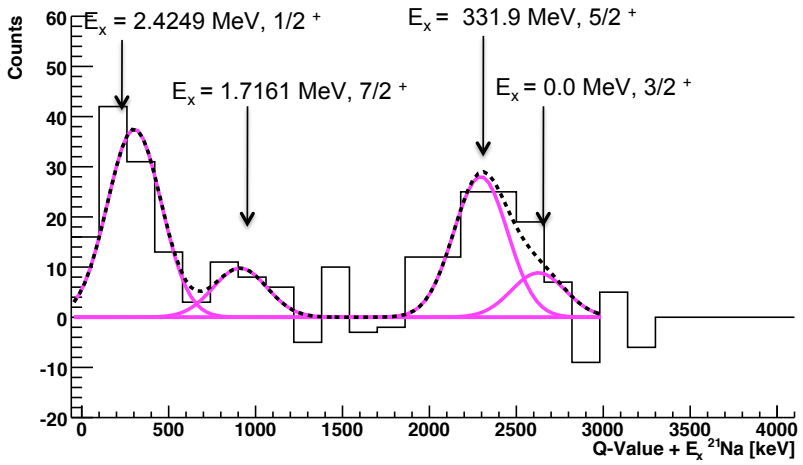

(b) Background subtracted Q-value spectrum for $E_{\mathrm{CM}} = 2.5$ MeV

Figure 7.4: *Background and background subtracted histogram for the* $^{18}Ne(\alpha,p)$ *reaction at* $E_{\mathrm{CM}} = 2.5$ *MeV*

Table 7.1: Details of the height, centroid and sigma of each of the Gaussian peaks used to fit the $E_{\mathrm{CM}} = 2.5$ MeV data.

Parameter	**Value**
Height 1	8.86
Centroid 1	2.63 MeV
Sigma 1	154.8
Height 2	28.1
Centroid 2	2.31 MeV
Sigma 2	154.8
Height 3	9.8
Centroid 3	0.911 MeV
Sigma 3	154.8
Height 4	37.5
Centroid 4	0.300 MeV
Sigma 4	154.8

This was done via a Monte Carlo technique, generating random kinematic angles with probabilities weighted according to Legendre polynomials. Legendre polynomials of $l = 0$-5 were examined, the results of which can be seen in Figure 7.5.

It can be seen that in the angular range subtended by the detectors there is very little difference between the expected yields observed due to various angular distributions (Figure 7.5). This is also reiterated in Figure 7.6. The yield from groups of 8 strips of the type S2 detector were summed. From the combined yield and assuming the angle at the centre of the grouping, a differential cross section was calculated and plotted against Legendre polynomials for l= 0 and l =1 transitions. From the limited angular range and low statistics of the experiment no reliable information could be inferred from the protons' angular distribution regarding their angular momentum. It was therefore assumed that the distribution was isotropic (l=0), i.e. an s-wave transition, as this is the most probable case in astrophysical scenarios.

This information was then incorporated into the calculation of the total cross-section.

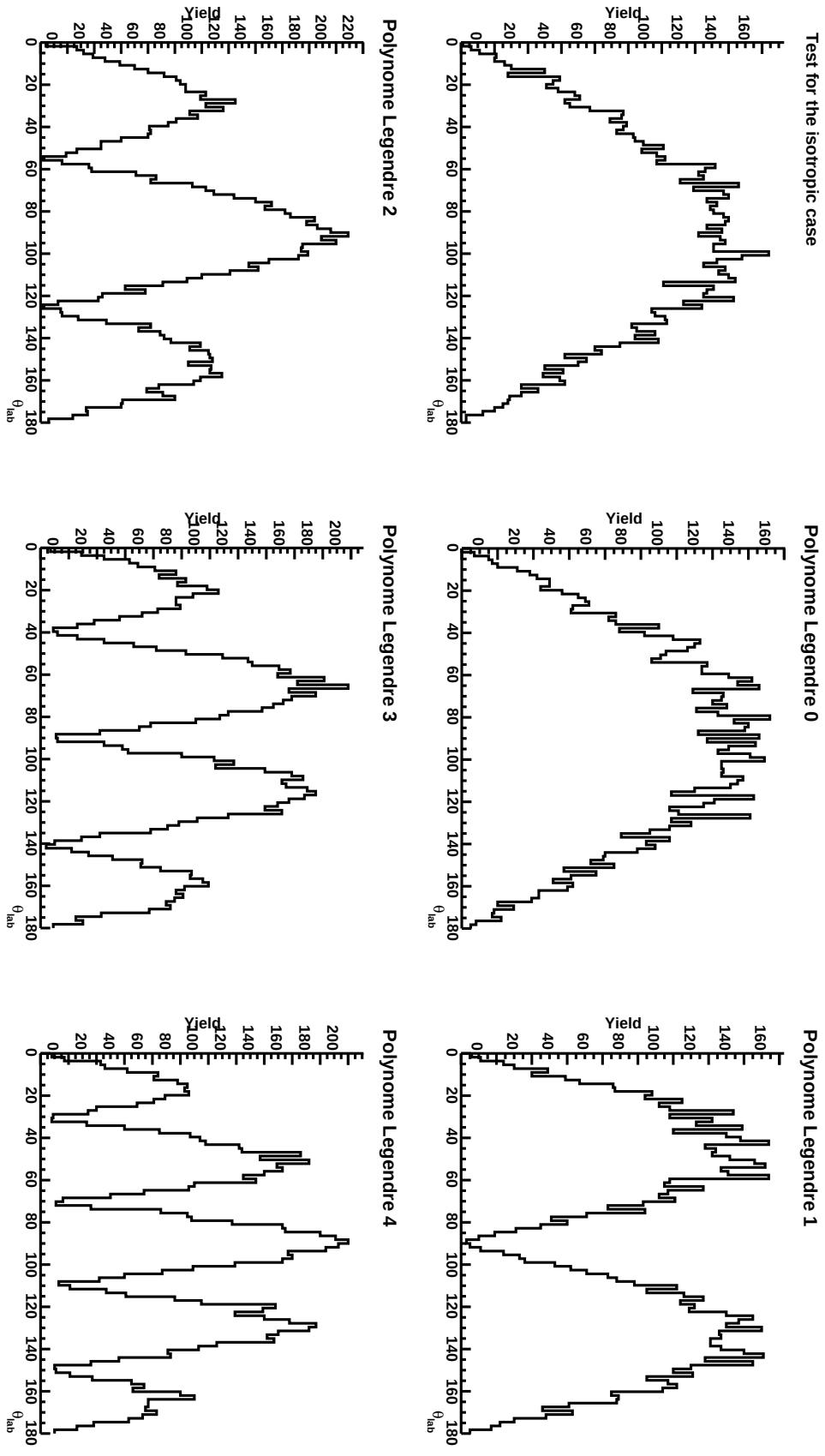

Figure 7.5: *Legendre Polynomials for l=0 to l =5*

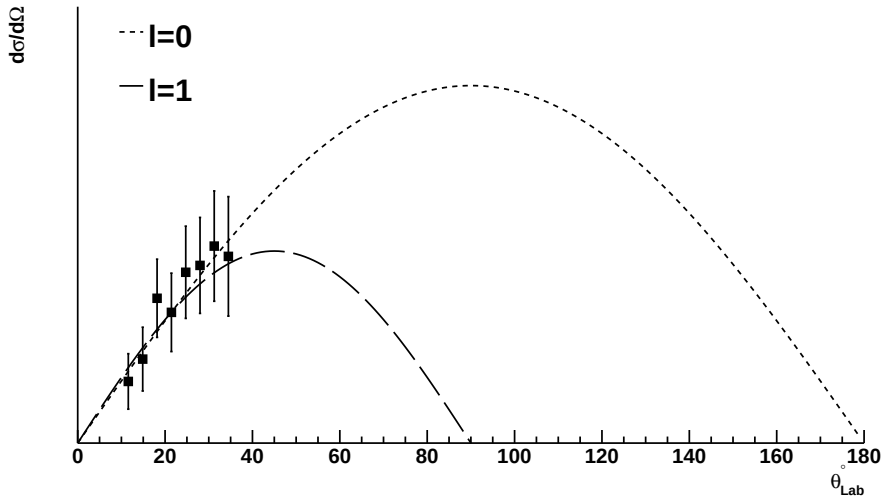

Figure 7.6: *Differential cross sections for the $^{18}Ne(\alpha, p)$ reaction. Figure illustrates that due to the limited angular range of the experiment and the low statistics there is no way to determine conclusively whether the angular distribution is that of an $l = 0$ or $l = 1$ transition.*

7.4.2 Cross-sections

With yields calculated for each populated state (E_{CM}=2.5 MeV) it was possible to calculate a total-cross section and the contribution from each of the identified states, this was done using equation 5.3. Although this calculates a differential cross-section a total cross-section can be calculated by normalising this value to 4π[1]. The time averaged beam current was calculated in the same manner as detailed in section 5.4.

As yields could not be discerned for the data at $\mathrm{E_{CM}}$=1.7 MeV an upper limit was calculated using the Feldman-Cousins technique [66] (with a 90% confidence limit) from which a cross section was calculated. The cross-sections are shown in Figure 7.7.

[1]This is only possible as an isotropic distribution is assumed

7.5 Interpretation of Results

7.5.1 Population of states

Figures 7.3 and 7.4 shows the background and background subtracted Q-value spectra for $E_{\mathrm{CM}} = 1.7$ and 2.5 MeV. From Figure 7.4(b) two main peaks can be identified. The broader peak at $Q \sim 2.5$ MeV is a combination of reaction protons from the ^{21}Na recoil being left in either the ground state ($Q = 2.627$ MeV) or first excited state (331.9 keV,$\frac{5}{2}^{+}$). The states could not be resolved individually as the difference in energy between the ground state and the first excited state is comparable to the experimental resolution and thus can not be resolved exclusively. The most prominent peak at $Q \sim 200$ keV corresponds to ^{21}Na being left in the third excited state (2.4249 MeV,$\frac{1}{2}^{+}$).

7.5.2 Reaction Rates

Figure 7.7 shows the cross-section against Q-value. At $E_{\mathrm{CM}} = 2.5$ MeV two cross-sections are presented, one corresponding to ^{21}Na recoil being left in the ground state (0.128 ± 0.031) mb, the other is the total cross-section which includes the inelastic channels being populated (1.22 ± 0.15) mb. At $E_{\mathrm{CM}} = 1.7$ MeV an upper limit for the cross-section has been evaluated using the Feldman-Cousins technique [66] with a 90% confidence level (0.021 mb). The solid line is a barrier penetration calculation normalised to the data point at $E_{\mathrm{CM}} = 2.5$ MeV for ground state protons. The dotted line is a Hauser-Feshbach calculation for the reaction including all states. The dashed line is a Hauser-Feshbach calculation examining only ground state to ground state reactions.

Figure 7.7 shows the results from this experiment alongside those of the data points from previous experiments. It should be noted here that cross-sections from previous experiments have not been stated explicitly in their respective publications and those illustrated in Figure 7.7 are taken directly from Figure 3.5. As can be clearly seen the cross-section at $E_{\mathrm{CM}} = 2.5$ MeV are an order of magnitude lower than the Sinha *et al* [42] results.

The conclusions that can be drawn from one experimental data point are limited. For instance, one cannot discern detail regarding any possible interference effects which may account for the difference in cross-sections between each of the measurements. It cannot be ruled out that the reaction is dominated by

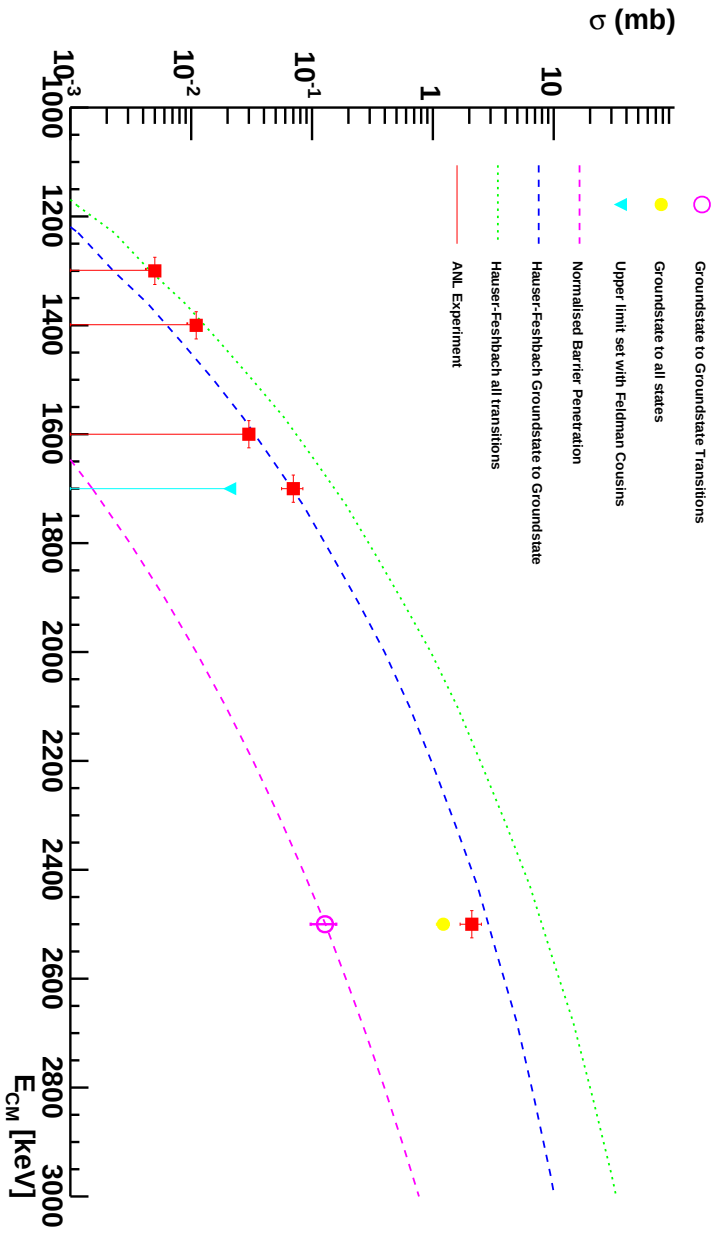

Figure 7.7: *Cross-sections presented at $E_{\mathrm{CM}} = 2.5$ MeV are of ground state to ground state transitions and for all states. Also shown is the barrier penetration factor normalised to the ground state to ground state data point at $E_{\mathrm{CM}} = 2.5$ MeV. Also shown is an upper limit for the cross-section calculated via the Feldman-Cousins technique at $E_{\mathrm{CM}} = 1.7$ MeV. The two Hauser-Feshbach lines shown are for goundstate-ground state transitions and for all states respectively. Courtesy of [67; 68]. The red data points are the experimental results from Sinha et al and are taken directly from 3.5.*

a broad resonance at this energy which is wider than the target, or indeed due to the high density of states if it is a broad continuum. In either case these could both account for the differences in σ between this experiment and Sinha *et al* [42].

Chapter 8

Conclusions and Future Work

The aim of this body of work was to investigate the two reactions, ^{18}F + p and ^{18}Ne(α,p), and present the results from these two reactions of astrophysical importance.

The rate of destruction of ^{18}F via the ^{18}F + p reactions, ^{18}F(p, α) and ^{18}F(p, γ), is of importance in both novae and X-ray burster explosive scenarios. The competing rates of the synthesis and destruction of ^{18}F, an astronomical observable, determine the amount of ^{18}F present in the ejected envelope of a nova explosion. To calculate the rates of the two destructive ^{18}F + p reactions a detailed spectroscopic knowledge of the compound nucleus ^{19}Ne above the ^{18}F + p threshold is required.

This region of ^{19}Ne was probed via the ^{15}O(α, α) elastic scattering reaction at the CRC, Louvain-la-Neuve, Belgium. Elastically scattered α-particles from a thick gaseous ^{4}He target were detected by segmented silicon detectors. The excitation function was subsequently fitted at $\theta_{\mathrm{CM}} = 168.1°$, $164.2°$ and $160.3°$ via the R-matrix formalism. From the fits, resonance parameters of energy and width could be extracted for the states about the ^{18}F + p threshold.

States in ^{19}Ne that had not been previously observed were covered by the energy range of this experiment. The states, all below the ^{18}F + p threshold were: $\frac{7}{2}^+$ $E_{\mathrm{x}} = 6.119$ (0.085) MeV with $\Gamma_\alpha = 0.33$ (0.015) keV, two $\frac{1}{2}^+$ $E_{\mathrm{x}} = 6.154(0.018)$ and $E_{\mathrm{x}} = 6.196(0.120)$ MeV with $\Gamma_\alpha = 18.8(1.9)$ keV and $\Gamma_\alpha = 2.04$ (1.4) keV keV respectively, $\frac{3}{2}^-$ $E_{\mathrm{x}} = 6.158$ (131)MeV with $\Gamma_\alpha = 0.80$ (0.7) keV and $\frac{5}{2}^+$ $E_{\mathrm{x}} = 6.317(6.5)$ MeV with $\Gamma_\alpha = 12.6(0.4)$ keV.

The main focus of the experiment was on a possible $\frac{3}{2}^+$ doublet at $E_{\mathrm{r}} = 8$ and 38 keV, which, to date has had its resonance parameters inferred from the

mirror nucleus ^{19}F. Following this new experimental approach and analysis the $\frac{3}{2}^+$ doublet was found to straddle the ^{18}F + p threshold with E_r = -22 and 3 (17) keV and Γ_α = 0.15 (0.2) and 3.3 (0.5)[1] keV respectively. S-factor calculations examining the four unique interference scenarios between these states and another $\frac{3}{2}^+$ state at E_r = 665 keV, Γ_α = 23.8 keV were examined. It was shown that there is a great difference between the four S-factor calculations in the temperature region of interest. It was, therefore, not possible to constrain the reaction rate of ^{18}F from these results alone.

However, the results do add motivation for the study of the direct reaction. Through information derived from this experiment and future direct measurements it will be possible to determine a reaction rate and the interference between the states.

For both cases (direct and indirect measurements) improvements in results would be achieved with improvements in experimental instrumentation. The improvement in radioactive ion beam intensities is of paramount importance to study these reactions.

Figure 8.1 shows the current experimental data with a calculated excitation function assuming a 10 keV experimental resolution. This resolution could be achieved if a thin windowless gas target were used. However, to cover the same energy range as this experiment many different beam energies would be needed as the target is thin. This could prove to be very time consuming.

With higher beam intensities the ^{18}F(p, α) reaction could be studied directly. Studying the cross-section at various E_{CM} values would allow for comparison to the S-factor calculations in this thesis thus allowing one to pinpoint which interference effects are prevalent in this reaction.

The ^{18}Ne(α,p)^{21}Na reaction is believed to play a crucial role in X-ray burster scenarios. The reaction is one of the possible HCNO breakout reactions that are responsible for generating the energy that drives this explosive scenario.

The reaction was studied at the CRC, Louvain-la-Neuve, Belgium. Reaction protons from interactions between a radioactive ^{18}Ne beam and a thin gaseous ^{4}He target were detected by segmented silicon detectors over an angular range between θ_{lab} = $\sim$10° and 30°. From the data a cross section at E_{CM} = 2.5 MeV

[1]It should be noted that all errors stated in the conclusion are those calculated manually and do not take into account any correlation between each state's properties

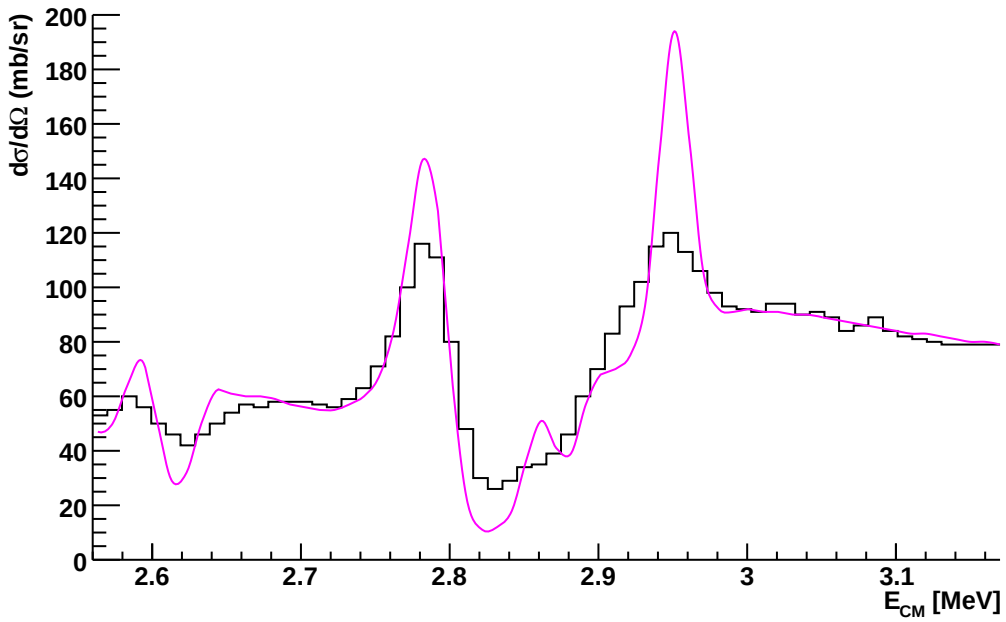

Figure 8.1: *Potential excitation function for* $^{15}O(\alpha,\alpha)$ *reaction with a 10 keV resolution. The excitation function has been calculated assuming the properties of the states concluded from the current experiment.*

of 1.22±0.15 mb was calculated and an upper limit (90% confidence limit) of 0.021 mb set at $E_{\mathrm{CM}} = 1.7$ MeV.

The cross sections were compared to the previous experiments of [41; 42]. The comparative cross section of ^{21}Na being left in its ground state calculated in this study were an order of magnitude below that of [42].

The evaluated cross section is also below that of the Hauser-Feshbach statistical model predictions. To date the reaction rate of this experiment has been based upon the Hauser-Feshbach results, which show cross section varying smoothly as a function of energy. This new direct measurement result shows that the reaction rate may have been significantly overestimated.

One cannot discern any information regarding the shape of the excitation function from this result as no information regarding possible interference effects appear. The interference effects at astrophysical temperatures will likely play an important part in accurately determining the reaction rate and are not taken into account within a Hauser-Feshbach calculation.

Ideally further direct studies at energy points E_{CM} <1.7 MeV are needed, which correspond to the astrophysical relevant temperatures. However, to perform such experiments a vast improvement in the beam intensity of ^{18}Ne, is needed. Currently the maximum available intensity is $\sim 10^6$ pps, which is the same intensity that was used for this measurement. The poor statistics from this experiment clearly show that this beam intensity is too low to study this reaction at low energies. An increase of 2-3 orders of magnitude would be required to study the reaction at E_{CM} <1.7 MeV and below.

In the interim, the time reverse reaction ^{21}Na(p, α)^{18}Ne, is a better candidate for study. The experiment of [41; 42] had an average beam intensity of ∼5000 pps. Recent developments at the TRIUMF laboratory, Canada, have produced a ^{21}Na beam with an intensity of $\sim 10^8$ pps. A proposal to study this has been approved and will take place in late 2009.

Appendix A

Semiconductor Detectors

Semiconductor devices are analogous in mechanism to gaseous ionisation detectors. Whereas in gaseous detectors radiation traversing the detector ionises the gas, in semiconductor devices the radiation creates electron-hole pairs in the semiconductor substrate. In both cases, the charge produced is collected by an electric field applied to the detector. The current produced is related to the energy of the ionising radiation.

Semiconductor detectors have certain advantages over gas ionization detectors:

1. The average energy ($\sim$eV) to create an electron-hole pair is much lower than that in a gaseous detector, typically $\times$ $\sim$10 smaller. This will lead to a better energy resolution as the amount of charge being produced for a given energy will be an order of magnitude greater. The variance is also reduced due to a greater magnitude of electron hole pairs.

2. The material is solid, and therefore, of a greater density. This will result in a greater stopping power.

3. The detectors are more compact and have a faster response time.

A.1 Silicon Detectors

Silicon is a group IV element with 4 valence electrons. At T=0 K they are all found in the valence band A.1 and all used in covalent bonds between the lattice atoms. As a result of there being no 'free' electrons when an electric field is applied there will be no current.

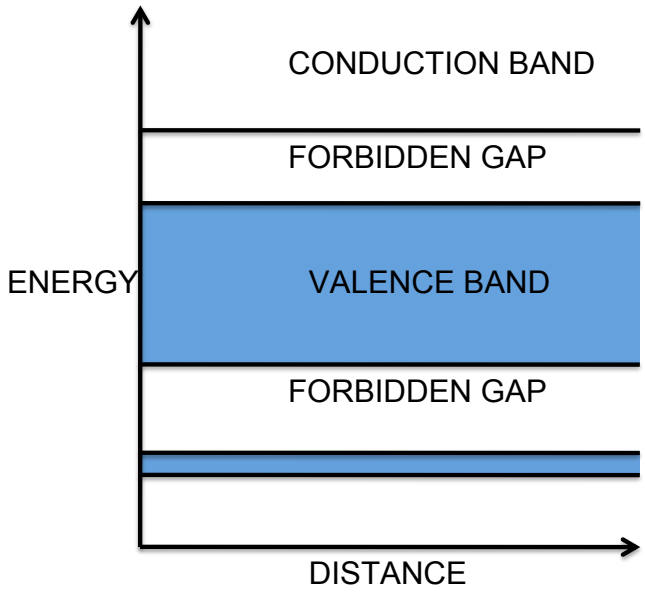

Figure A.1: *Energy band structure in a semiconductor. Adapted from [69]*

If radiation imparts energy to a bond then it can be broken, exciting an electron to the conduction band. The electron in the conducting band is 'free'. This will leave a vacant state, an 'electron hole' in the valence band. This hole can be thought of as a positive charge.

The hole can be filled by an electron from a nearby atom in the lattice leaving another hole in its place. This process repeats, again and again. The movement of the now free electron and the hole can be directed by an electric field and thus a current can flow.

The conduction band is only empty at $T = 0$ K. At higher temperatures thermal energy may excite an electron to move from the valence band to the conducting band creating electron holes. To better control the conductivity at operational temperatures impurities are introduced.

A.1.1 Doping

If a silicon atom in the lattice were to replaced by an atom with 5 valence electrons (e.g. phosphorous, arsenic), the net effect would be an unbound electron. An impurity which results in an excess of electrons is known as a *donor*. This electron is only loosely bound and will form a discrete energy level of the order of 0.01 eV below the conduction band in the forbidden gap. This can be easily excited to the conduction band.

If a trivalent impurity (e.g boron) is added to the silicon lattice this has the net effect of leaving an unpaired silicon electron. The boron 'borrows' this electron leaving a hole in its place. An impurity which results in a depletion of electrons is known as an *acceptor*. This borrowed electron is only loosely bound to the trivalent impurity as its nucleus only has a charge of $^{+}3$, therefore it forms a discrete energy level in the order of 0.01 eV above the valence band. Electrons from the valence band are easily excited to this level, thus, leaving holes in the valence band.

Charge carriers in donor-doped material are negative and are thus known as a n-type. An acceptor-doped material is known as p-type as the charge carrier is positive.

A.1.2 Depletion Zone

The junction formed between a p-type and n-type material has certain properties. Due to the difference in charge type and concentration, there is a drift of electrons and holes between the two. This exposes the respective donor/acceptor resulting in the p-type region becoming negatively charged and the n-type positively charged. This has the effect of creating an electric field across the junction.

This is known as the depletion zone, an area devoid of all charge carriers. Any electron or hole entering will be moved by the electric field in this area. Ionizing radiation traversing the depletion zone will free electron-hole pairs which will then be swept aside by the electric field. If electrical contacts are placed on either end of the junction a current signal proportional to the ionization intensity will be detected.

With the application of an external potential two different modes of non-equilibrium can be attained:

1. A positive bias applied to the p-type side and a negative potential to the n-type side. This is known as 'forward bias'. This has the effect of reducing the depletion zone and allowing an increase in charge transfer.

2. A negative bias is applied to the p-type side and a positive bias to the n-type. This is known as 'reverse bias'. This has the effect of increasing the size of the depletion zone and impeding current flow. A reverse biased junction is used in particle detectors. At a certain point, too high a voltage will cause the junction to breakdown and start conducting.

A.2 Experimental Detectors

A.2.1 SSSSD

LEDA (MSL type YY1[55]) is an example of a single sided silicon strip detector.

It is manufactured thus, see Figure A.2:

1. A silicon wafer (bulk typically ∼300 μm thick) is cleaned. It usually has slight impurities making it either slightly n or p type. Assume that it is n-type.

2. The substrate is oxidised on the surface. This allows for isolation between the strips (Stage 3)

3. The bulk is then heavily doped via ion-implantation, p^+ on the front and n^+ on the back. n^+ at the back as this will produce a much better low resistance (Ohmic) contact compared to the Si substrate.

4. Front and back are aluminised

It is important to note that the depletion region is predominantly in the lightly doped bulk. The aluminised layer and the p^+ implantation are known as the *dead layer* of the detector as an impinging particle will lose energy but not ionise the detector.

The bulk of the detector is n-type silicon, with a strip of p^+-type (boron doped) implanted on the front. Aluminium contacts are added on top of each

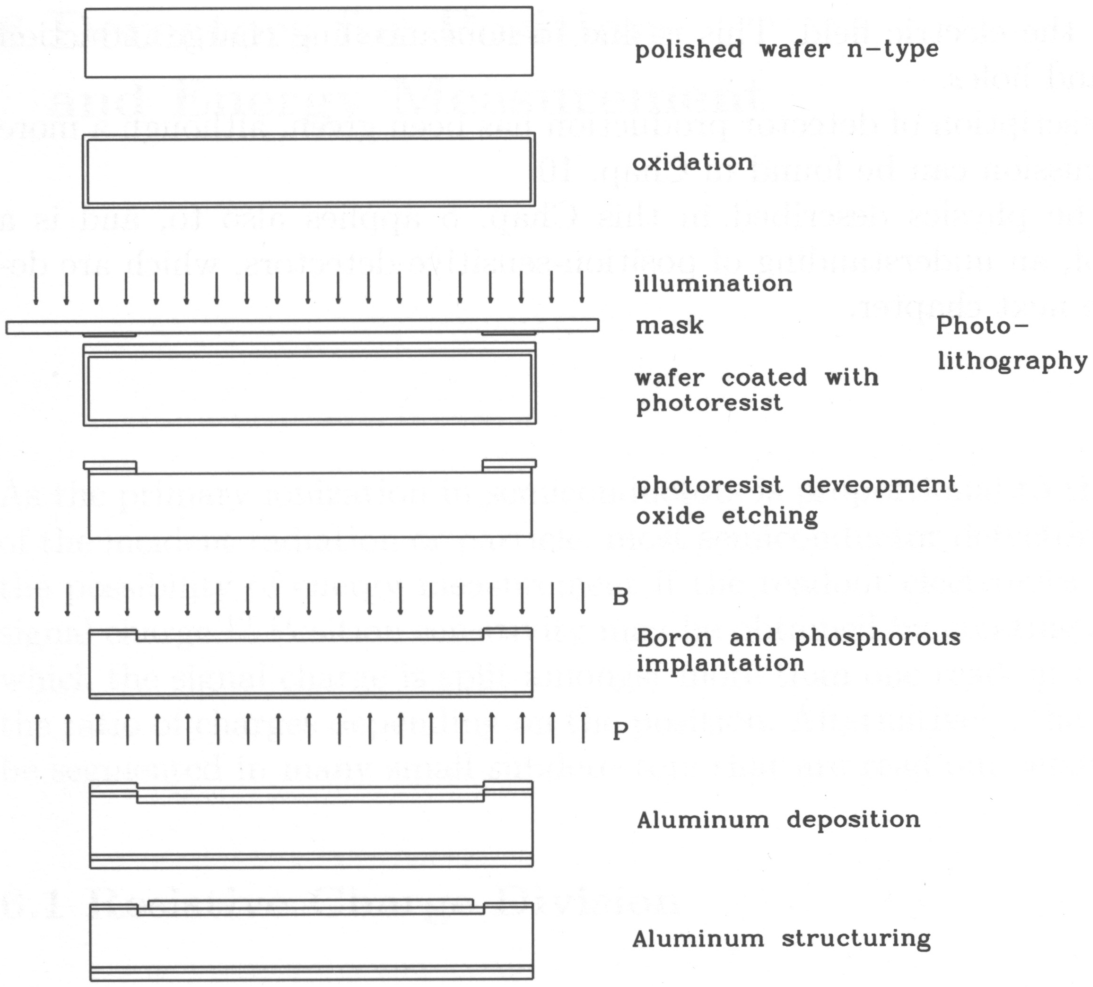

Figure A.2: *Manufacturing process of single sided silicon detector [70]*

strip and isolated by inter-strip of SiO_2. The rear of detector is a complete n^+-type, arsenic doped, with aluminium contacts.

A.2.2 DSSSD

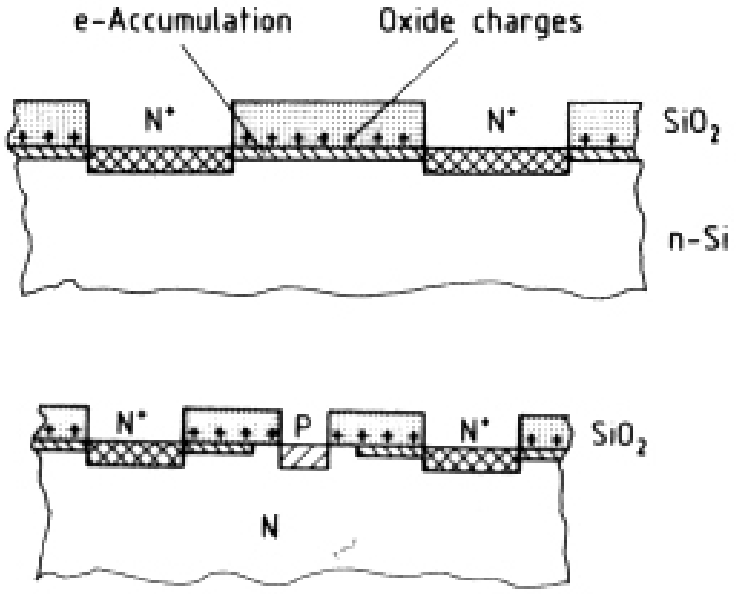

Figure A.3: *DSSSD implantation [71]*

This is again lightly doped silicon bulk, oxidised surface with front and back heavily doped p^+ and n^+.

The top diagram in Figure A.3 shows the problem of having the backside of the n-type substrate being implanted with a pentavalent material. The electron accumulation between n^+ strips prevents there being electrical isolation between the strips.

The effect of the accumulation is alleviated through the implantation of a trivalent material forming p-type 'barriers' between the n^+ strips, this is shown in the bottom diagram of Figure A.3.

Appendix B

Calculation of ΔE and r_{max} for R-matrix fits

B.1 ΔE

ΔE was calculated with the aid of SRIM [58]. The energy loss and straggling effects of an α-particle from an interaction at the centre of the target through to being detected at laboratory angles of $\theta_{lab} = 5.194°$ and $7.243°$ (annulus strips 0-3 of LEDA).

The calculation is as follows:
$\theta_{lab} = 5.194°$

1. Initial Energy at centre of target: 8.905 MeV
   After 3cm of ^{4}He at 300 mbar: 8.803 MeV
   σ = 7411.3 eV
   FWHM = 17.42 keV

2. Energy at Mylar exit window: 8.803 MeV
   After 12μm Mylar: 7.812 MeV
   σ = 23,037 eV
   FWHM = 54.14 keV

3. Energy at dead layer of detector: 7.812 MeV
   After 0.4μm Aluminium: 7.769 MeV

σ = 5,405 eV
FWHM = 12.70 keV

The same calclations are followed through at $\theta_{lab} = 7.243°$ to examine kinematic effects on the resolution.
$\theta_{lab} = 7.243°$

1. Initial Energy at centre of target: 8.836 MeV
   After 3cm of ^{4}He at 300 mbar: 8.733 MeV
   σ = 7,113 eV
   FWHM = 16.7 keV

2. Energy at Mylar exit window: 8.733 MeV
   After 12μm Mylar: 7.733 MeV
   σ = 23,746 eV
   FWHM = 55.80 keV

3. Energy at dead layer of detector: 7.733 MeV
   After 0.4μm Aluminium: 7.689 MeV
   σ = 5,218 eV
   FWHM = 12.26 keV

Summing the FWHM from straggling effects in each medium, the response of the detector ∼35 keV FWHM and kinematic effects (FWHM = 54.3 keV) in quadrature the resolution is calculated to be ΔE_{lab} 87.9 keV, ΔE_{CM} 18.5 keV

B.2 r_{max}

The nuclear radius is calculated using:

$$r_{max} = r_0(A_t^{\frac{1}{3}} + A_p^{\frac{1}{3}}) \tag{B.1}$$

where r_0 is the radius parameter and is between 1.0 - 1.5 fm

The calculated r_{max} for both the ^{15}O(α,α) and ^{15}N(α,α) reaction is 6.08 fm[1].

[1] An r_0 of 1.5 fm was used

Bibliography

[1] M.S.Smith D.W.Bardayan, R.L.Kozub. ^{19}F α widths and the ^{18}F+p reaction rates. *Physical Review C.*, **71**:018801–1, 2005. (document), 3.1, 5.5.1, 5.5.1, 5.11, 5.12, 5.2, 5.5.2, 6.1.3

[2] G.Gamow Alpher, Bethe. The Origin of Chemical Elements. *Physical Review*, **99**:204, 1948. 1.2

[3] http://www.thaispaceweather.com/IHY/Stars/images/main01.gif. 1.1

[4] M.Wiescher *et al.* Break-out Reactions from the CNO cycles. *J.Phys.G.Nucl.Part.Phys.*, **25**:133, 1999. 1.2.1.2

[5] C.F. von Weiszsäcker. *Phys.Z.*, **38**:137, 1937. 1.2.1.2

[6] C.F. von Weiszsäcker. *Phys.Z.*, **39**:633, 1938. 1.2.1.2

[7] C.L.Critchfield H.A.Bethe. *Physical Review.*, **54**:248, 1938. 1.2.1.2

[8] W. S. Rodney C. E. Rolfs. *Cauldrons in the Cosmos*. University of Chicago Press, Chicago, 1988. 1.2.1.2, 2.2, 2.3, 2.2.2

[9] www.src.le.ac.uk/projects/lobster/cyg75plot.jpg. 1.4

[10] M.Wiescher A.E.Champagne. Explosive Hydrogen Burning. *Annual Review Nuclear Particle Science*, **42**:39–76, 1992. 1.3.1, 1.4.1, 1.4.2, 1.5.1, 3.1.1

[11] A.W. Shafter *et al.* Classical Nova Explosions. *AIP Conference Proceedings*, **637**:462, 2002. 1.3.1

[12] S.Starrfield *et al.* Evolutionary sequences for Nova V1974 Cygni using new nuclear reaction rates and opacities. *Mon.Not.R.Astron.Soc*, **296**:502, 1998. 1.3.1

[13] J. W. Truran. *Physics of Classical Novae*. Springer, Berlin, 1990. 1.3.1

[14] M.Wiescher *et al.* Astrophysical nuclear reaction and the break-out from the hot CNO cycles. *Progress in Particle and Nuclear Physics*, **59**:51–65, 2007. 1.5, 1.5.1

[15] http://hemel.waarnemen.com/Informatie/Sterren/hoofdstuk6.html. 1.4, 1.6

[16] http://www.star.le.ac.uk/julo/research.html. 1.7, 1.4.1

[17] M.Wiescher *et al.* Reactions with radioactive beams and explosive nucleosynthesis. *Phil.Trans.R.Soc.Lond*, **356**:2105–2136, 1998. 1.4.1, 1.4.2

[18] H.Schatz and K.E.Rehm. X-ray Binaries. *Nuclear Physics A*, **777**:601–622, 2006. 1.4.2

[19] S. E. Woosley and T. A. Weaver. High energy Transients in astrophysics, 1984. AIP Confernce Proceedings. 1.4.2

[20] R.K.Wallace and S.E.Woosley. Explosive Hydrogen Burning. *Astrophys.J.Suppl*, **45**:389, 1981. 1.5.2

[21] M.Hernanz *et al.* Gamma-Ray Emission of Classical Novae and its Detectability by INTEGRAL, 1998. 3rd INTEGRAL Workshop: The Extreme Universe, Taormina (Italy). 1.6.1

[22] A.Shotter *et al.* Breakout from the hot CNO cycle via the ^{18}Ne(α,p)^{21}Na rection, 1999. E870 Proposal. 1.12

[23] G.Gamow. Zur Quantentheorie de Atomkernes. *Z.Phys*, **51**:204, 1928. 2.1.2

[24] P. Descouvemont. *Theoretical Models for Nuclear Astrophysics*. Nova Biomedical, 2004. 2.3

[25] W.Hauser and H.Feshbach. The Inelastic Scattering of Neutrons. *Physical Review*, **15**:366, 1952. 2.4

[26] K.E.Rehm *et al.* Study of the ^{18}F(p,α)^{15}O reaction at astrophysical energies using a ^{18}F beam. *Physical Review C.*, **52**, 1995. 3.1

[27] D.W.Bardayan *et al.* Destruction of ^{18}F via ^{18}F(p,α)^{15}O burning through the E_{CM}=665keV resonance. *Physical Review C.*, **63**, 2001. 3.1

[28] D.W.Bardayan *et al.* Strength of the ^{18}F(p,α)^{15}O Resonance at $E_{c.m}$=330keV. *Physical Review Letters*, **89**, 2002. 3.1

[29] N. de Sereville *et al.* Direct measurement of the ^{18}F(p,α)^{15}O reaction for the application to nova γ-ray emission, 2005. Nuclei in the Cosmos - IX, CERN, Switzerland, 2006. 3.1

[30] S.Utku *et al.* Breakout from the hot CNO cycle:The ^{18}F(p,α) vs ^{18}F(p,γ) branching ratio. *Physical Review C.*, **57**:2731 – 2739, 1997. 3.1, 5.5.2, 6.1.3

[31] D.W.Visser *et al.* Particle decay branching ratios for states of astrophysical importance in ^{19}Ne. *Physical Review C.*, **57**:2731, 1997. 3.1

[32] N. de Sereville *et al.* Indirect study of ^{19}Ne states near the ^{18}F+p threshold, 2008. Preprint Elsevier. 3.1

[33] D.W.Bardayan *et al.* Kinematically complete measurement of the ^{1}H(^{18}F,p)^{18}F excitation function for the astrophysically important 7.08 MeV state in ^{19}Ne. *Physical Review C.*, **62**, 2000. 3.1

[34] D.W.Bardayan *et al.* Search for astrophysically important ^{19}Ne levels with a thick-target ^{18}F(p,p)^{18}F measurement. *Physical Review C.*, **70**, 2004. 3.1, 5.5.2

[35] R.L.Kozub *et al.* New constraints on the ^{18}F(p,α)^{15}O rate in novae from the (d,p) reaction. *Physical Review C.*, **71**:032801, 2005. 3.1

[36] C.D.Nesaraja *et al.* Nuclear structure properties of astrophysical importance for ^{19}Ne above the proton threshold energy. *Physical Review C.*, **75**:055809, 2007. 3.1.1, 3.1, 2, 3.2, 3.1.2.1, 5.5.2

[37] http://www.nndc.bnl.gov/ensdf/. 3.1, 5.1

[38] F.de Oliveira *et al.* Comparison of low-energy resonances in ^{15}N(α,γ)^{19}F and ^{15}O(α,γ)^{19}Ne and related uncertainties. *Physical Review C.*, **55**:3149–3151, 1997. 1

[39] W.Bradfield-Smith. Breakout from the hot-CNO cycle via the ^{18}Ne(α,p)^{21}Na reaction. *Phys. Rev. C*, **59**:3402, 1999. 3.2, 3.5

[40] D.Groombridge. Breakout from the hot CNO cycle via the ^{18}Ne(α,p)^{21}Na reaction. II. Extended energy range E_{CM}∼1.7-2.9 MeV. *Phys. Rev. C*, **66**:055802, 2002. 3.2, 3.1, 3.5, 3.2.1

[41] S.Sinha, 2003. Argonne National Laboratory Annual Report,http://www.phy.anl.gov/div/ar04/I.%20Heavy-Ion%20Sec.%20A.pdf. 3.2, 4.4.2, 8

[42] S.Sinha, 2004. Argonne National Laboratory Annual Report, http://www.phy.anl.gov/div/ar05/iheavy 1.pdf. 3.2, 3.5, 7.5.2, 8

[43] Pierre Descouvement. http://pntpm3.ulb.ac.be/Nacre/Programs/coulomb.htm. 3.1, 3.2.1

[44] Andrija Matičč. *High-precision (p,t) reactions to determine reaction rates of explosive stellar processes.* PhD thesis, Rijksuniversiteit Groningen, 2007. 3.2.2, 3.6

[45] M. Fujiwara *et al.* Magnetic spectrometer Grand Raiden. *Nucl. Instrum. Methods A*, **422**:484, 1999. 3.2.2

[46] http://www.cyc.ucl.ac.be/. 4.1, 4.1, 4.2

[47] M.Gaelens *et al.* High Efficiency release targets for Radioactive Ion Beams: A Different Approach, 1998. 15th International Conference on the Applications of Accelerators in Research and Industry, Denton, Texas. 4.1.1.2

[48] C.Barue *et al.* Electron cyclotron resonance ion source developments at Louvain-la-Neuve. *Review of Scientific Instruments*, **69**:764, 1998. 4.1.1.3

[49] M.Loiselet *et al.* Production and Acceleration of Radioactive Beams at Louvain-La-Neuve, 1995. 14th International Conference on Cyclotrons and their Application, Cape Town. 4.1.1.4

[50] L.C. McDermott H.Smotrich, K.W.Jones and R.E. Benenson. Elastic Scatteing of Alpha Particles by ^{15}N. *Phys.Rev.*, **122**:232, 1961. 4.2.1, 5.5.1

[51] W.Galster *et al.* Target and detection techniques for the ^{13}N(p,γ)^{14}O reaction using radioactive ion beams: ^{13}C(p,γ)^{14}N reaction as a test case. *Phys. Rev. C*, **44**:2776–2787, 1991. 4.2.1

[52] http://www.swagelok.com/. 4.5

[53] D. Josephides. Private Communication. 1

[54] http://www.mksinst.com/docs/UR/pressureselector.aspx. 4.3.2

[55] T.Davinson *et al.* Louvain-Edinburgh Detector Array (LEDA): a silicon detector array for use with radioactive nuclear beams. *Nuc, Inst. Meth.*, **A454**:188, 2000. 4.3.3, 4.4.2, A.2.1

[56] http://www.micronsemiconductor.co.uk/. 4.3.3, 4.8, 4.4.2

[57] http://www.scitech.ac.uk. 4.3.4.1

[58] James Ziegler. http://www.srim.org/. 4.4.1, 4.4.2, 5.3, B.1

[59] C.Angulo *et al.* Identification of a new low-lying state in the proton drip line nucleus ^{19}Na. *Physical Review C*, **67**, 2003. 3

[60] Pierre Descouvement. DREAM - *R*-matrix calculation and fitting application. 5.5

[61] Fred James. http://wwwasdoc.web.cern.ch/wwwasdoc/minuit/minmain.html. 5.5

[62] N. de Sereville *et al.* Low-energy ^{18}F(p, α)^{15}O cross section measurements relevant to nova gamma-ray emission, 2008. Submitted to Phys.Rev.C 2008. 6.2

[63] W.N.Lennard *et al.* Nonlinear response of Si detectors for low-Z ions. *Nuclear Instruments and Methods.*, **A248**:454–460, 1986. 7.1

[64] F.S Goulding and B.G. Harvey. Identification of Nuclear Particles. *Ann. Rev. Nucl. Sci.*, **25**:167, 1975. 7.2

[65] N.de.Sereville. *Etude de la Reaction ^{18}F(p,α)^{15}O par Reaction de Transfert pour Application a l'Emission Gamma des Novae.* PhD thesis, L'Universite Paris, 2003. 7.3

[66] G. Feldman and R. Cousins. Unified approach to the classical statistical analysis of small signals. *Phys. Rev. D*, **57**:3873–3889, 1998. 7.4.2, 7.5.2

[67] T. Rauscher and F.K. Thielemann. Astrophysical reaction rates from statistical model calculations. *Atomic Data Nuclear Data Tables*, **75**, 2000. 7.7

[68] T. Rauscher. Private Communication. 7.7

[69] Helmuth Spieler. Solid state detectors and electronics, 2007. Lectures to TRIUMF Summer Institute, http://www-physics.lbl.gov/ spieler/TSI-2007/index.html. A.1

[70] G. Lutz. *Semiconductor Radiation Detectors*. Springer, Berlin, 1999. A.2

[71] J. Kemmer and G. Lutz. New structures for position sensitive semiconductor detectors. *Nuclear Instruments and Methods in Physics Research*, **A273**:588–598, 1988. A.3